# A Model and Device for High Throughput Measurements of Stem Flexural Stiffness in Grains

A Thesis

Presented in Partial Fulfillment of the Requirements for the

Degree of Master of Science

with a

Major in Mechanical Engineering

in the

College of Graduate Studies

University of Idaho

by

Austin Bebee

Major Professor: Daniel Robertson, Ph.D.

Committee Members: Matthew Swenson, Ph.D.; Edwin Odom, Ph.D.

Department Administrator: Steven Beyerlein, Ph.D.

May 2020

## Authorization to Submit Thesis

This thesis of Austin Bebee, submitted for the degree of Master of Science with a Major in Mechanical Engineering and titled "A Model and Device for High Throughput Measurements of Stem Flexural Stiffness in Grains," has been reviewed in final form. Permission, as indicated by the signatures and dates below, is now granted to submit final copies to the College of Graduate Studies for approval.

Major Professor: _____ Date: _____
Daniel Robertson, Ph.D.

Committee Members: _____ Date: _____
Matthew Swenson Ph.D.

_____ Date: _____
Edwin Odom, Ph.D.

Department Administrator: _____ Date: _____
Steven Beyerlein, Ph.D.

## Abstract

The global issue of crop lodging has significant, negative impacts on crop quality and supply. Crop lodging refers to the structural failure of crops due to external (e.g., rain, wind) and internal loading (e.g., grain weight). To reduce crop lodging, crops with high lodging resistance must be developed through selective breeding. However, numerous confounding factors make it difficult to evaluate lodging resistance accurately and efficiently. Several devices and methods have been developed to evaluate lodging resistance. Unfortunately, most of these devices are low throughput and only allow a limited number of plants to be tested at a time. More rapid evaluations are required to enable more efficient and effective selective breeding processes.

This thesis presents a novel device known as the SOCEM (Stiffness of Crops Extrapolation Machine) that can determine the lodging resistance of grain crops in a high throughput manner. The SOCEM is able to evaluate entire experimental plots in just a few minutes. The device utilizes a novel mathematical crop model to account for nonlinearities and interactions within mechanobiological systems. The model is derived and validated using physical and finite-element model experiments and its most effective range is highlighted.

## Acknowledgements

First, I would like to thank all members of my committee for their valuable time involved in this work. Dr. Mathew Swenson provided me with long-term lessons on design, which I will continue to implement in industry. I thank Dr. Edwin Odom for the depth of expertise he brings to the committee. I of course would like to thank Dr. Daniel Robertson for greatly developing me as an engineer, researcher, and person. He has directed me with advice, inspiration, and freedom toward impactful work I am proud of.

I also acknowledge Dr. Christopher Stubbs for the incredible advice, work (especially finite-element modeling), and thought-provoking discussion he provided. The depth of this work and its analysis would not have been possible without his efforts.

I would also like to thank Steven Haener, Taylor Spence, and Nick Locke for all their help on the SOCEM development. It was a pleasure to work with all of you.

Dr. Kurtis Schroeder and Dr. David White also kindly provided their agricultural expertise and time while allowing me to conduct tests in their wheat variety trial plots.

Funding for this work was supported by a Seed Grant from the University of Idaho Office of Research and Economic Development, from the National Science Foundation Award #1826715, and from the United States Department of Agriculture-National Institute of Food and Agriculture award #2016-67012-28381. Any opinions, findings, conclusions, or recommendations expressed in this thesis are those of the author and do not necessarily reflect the view of the U.S. Department of Agriculture or of the National Science Foundation.

This work would not have been possible without the support provided by the Mechanical Engineering Department. The provided teaching and research assistantships gave me a rewarding and exceptional learning experience.

## Dedication

I dedicate this work to my partner Kailyn, who has patiently supported me throughout my academic career. I also thank my parents, who have supported me every step of my life. Lastly, I would like to thank all my siblings and friends for all their advice and encouragement that allowed me to follow this path here.

# Table of Contents

# List of Tables

# List of Figures

# Chapter 1: Background

## 1.1 Introduction

To understand the significance of the work presented in this thesis, this chapter provides an introductory summary. The global issue of crop lodging and its nature is presented first, followed by previous work conducted to reduce lodging, and current methods to evaluate lodging resistance. Lastly, as a transition into Chapter 2, existing crop models are briefly discussed.

## 1.2 Crop Lodging

In the broadest view, this thesis revolves around the concept of improving crop yield. Crops play various and vital roles in our lives. Many crops, particularly cereal or grains, provide humanity with the most popular food staples, food sweeteners, livestock feed, and fuel (e.g., producing ethanol from maize). Maize (i.e., corn), wheat, and rice collectively provide over half of the world's caloric intake [1]. The demand for biofuel from grains (primarily maize and some wheat) continues to increase [2]. In 2018, 2,620 metric tons of grains were produced globally [3]. As the world population rapidly increases, farmland decreases [4], and climate change effects increase, the efficiency of crop production becomes even more of a paramount concern. Given their increasing significance in everyday life, the importance of and demand for strong, dependable crops is substantial.

A phenomenon known as lodging has a significant effect on crop production and efficiency. Lodging refers to the mechanical failure of crops prior to harvest, which decreases crop yield and grain quality. Farmers and plant breeders around the world report lodging resistance as one of their greatest concerns [5], as it has a tremendous economic impact. Lodging results in an estimated 5-20% annual yield loss of maize globally [6]. In the United States, lodging in maize alone is estimated to cause losses of $3.8 billion dollars each year [7]. Wheat lodging in the United Kingdom typically results in estimated losses of $64 million per year [8]. During more severe wheat lodging years (every three to four years in the UK), 15-20% of the planted area is affected [9], leading to losses of approximately $218 million [8]. Further, these loss estimates are believed to be under-predictions, as they do not include such costs as increased grain drying, reduced cereal quality (e.g. bread-making quality), and increased harvesting time (which lodging also causes) [10]. Lodging hinders the photosynthesis process and transportation of nutrients and water [11]. Hence, reduced malting and bread-making quality is paired with lodging [12]. On a global scale, lodging induces trillion-dollar losses per annum [13]. Reduced yield consequently increases the costs of food, consumer goods, fuel, and other agricultural products.

Lodging can be further classified into either root lodging or stalk lodging, which both have different failure mechanics, as shown in Figure 1.1. Root lodging describes the failure of the root anchorage system, while stalk lodging describes the stem buckling. In root lodging, the soil, anchorage roots, or a combination fail and result in the displacement of the stem [14]. Stalk lodging occurs when bending moments along the stem exceed the bending strength of the stem, leading to stem failure, often in the form of buckling [15]. The bending moment is usually produced from a combination of self-loading, wind, or rain. Figure 1.2 illustrates the free body diagram of a deflected stem, in which loads are depicted at the grain head and the stem's center of gravity. The weight loads from both the stem and grain head represent self-loading. Notice that as deflection increases, the moments at the plant's base will increase due to both weight loads.


**Figure 1.1** [16] **(a)** Root lodging causing displacement in wheat. **(b)** Stalk lodging in barley. Reprinted by permission from Springer Nature Customer Service Centre GmbH: Springer, *Encyclopedia of Sustainability Science and Technology* by Pete Berry, edited by Robert Meyers (2012).

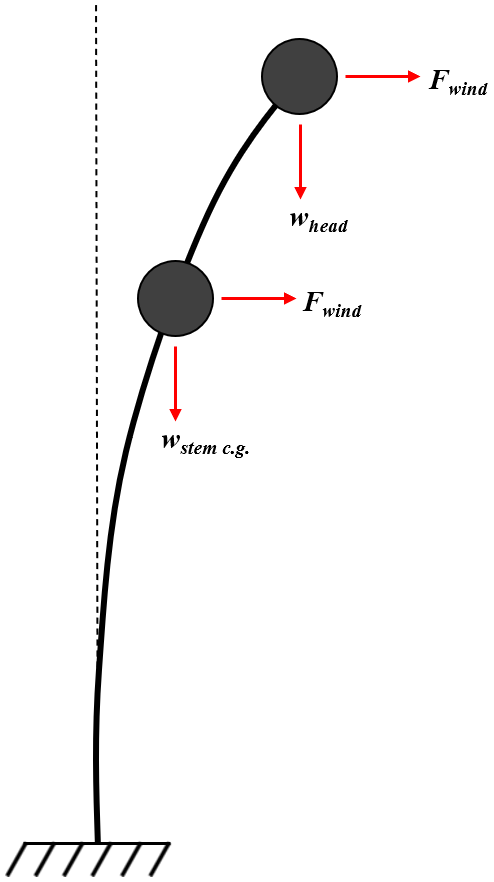


**Figure 1.2** The free body diagram of a deflected stem. External, wind and self-weight loads are depicted at the grain head and the stem's center of gravity (c.g.).

There are two types of buckling that can occur in plants. One type known as Brazier buckling, tends to be more predominant due to the stem shape. A simplified diagram of the stem structure is shown in Figure 1.3. Many plant stems can be modeled as thin-walled tubes [17]. Brazier buckling applies to thin-walled tubes that have ovalized due to bending, which can lead to a local collapse [15]. The ovalization increases the stress in the stem by reducing the second moment of area. Euler buckling is also possible, in which the entire stem buckles under a compressive load (i.e. self-loading), resulting in a curved stem. While separate mechanisms, Euler and Brazier buckling can interact and self-enhance [15]. Initial bending due to Euler buckling can commence Brazier buckling that can then cause ovalization, increasing stress and the chance of structural failure.

Due to different stem structures and characteristics among different types of crops, the location of stem failure varies. As shown in Figure 1.3, cereals generally consist of long, hollow internodes linked together by solid nodes [18]. In small grains, buckling is typically observed near the lower internodes [19-21] whereas, for maize, failure is often close to a node with the type of failure

(e.g., buckling, snapping, creasing, tissue failure) depending on the stage of development [22]. Regardless of the specifics, if stalk lodging occurs, the plant cannot recover [22].

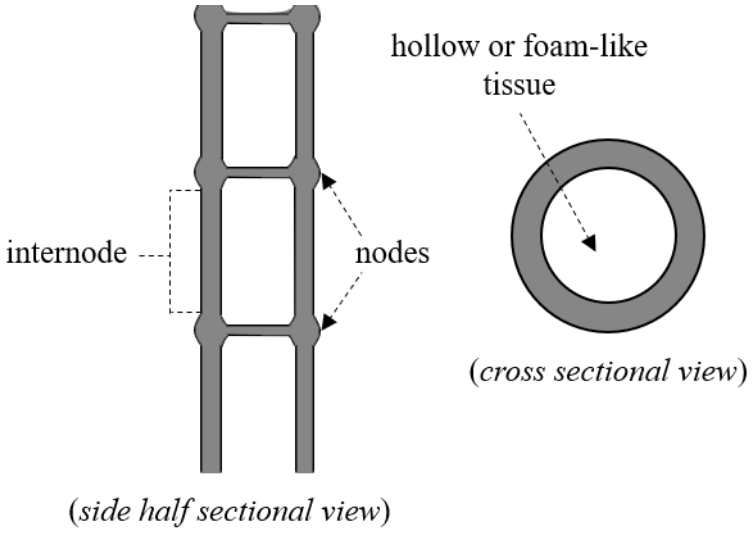


**Figure 1.3** Simplified diagram of the stem structure of plants.

While there is some debate as to whether root or stalk lodging is more predominant [19, 21, 23], both are recognized in modern agriculture. Despite being separate mechanisms, it is likely that root and stalk lodging interact with one another. Similar to Euler and Brazier buckling, consider when root lodging causes initial displacement that can then increase the bending moment along the stalk, increasing stress and the chance of stalk lodging [24]. It is necessary to study both types, but stalk lodging is the focus of this thesis.

### 1.3 Breeding for Lodging Resistance

One method to reduce the chance of stalk lodging, is to selectively breed for lodging resistant plants. Stalk strength must be made a priority in such breeding programs. Plants must possess a structure capable of enduring the internal and external forces (e.g. wind, rain, hail) [25] that act upon them while meeting metabolic needs to sustain their life and growth. Plant scientists have already made great strides to combat crop lodging. Perhaps most significantly, the introduction of semi-dwarfing varieties has increased the mechanical stability of several cereals [24]. Not only did shorter stems increase stability and reduce lodging, more nutrients were delivered to the heads, increasing their size [26]. Yield increased as a result. However, despite these advances, lodging is still a major recurring problem. New, alternative adaptations for breeding lodging resistant crops are required, especially as grain yield and weight increase [24]. Unfortunately, this is no simple task due to the

unique hierarchical, non-prismatic, nonlinear, and anisotropic structure of plants [27]. Properly and rapidly evaluating stalk strength is necessary to enable more efficient and effective breeding processes.

### 1.4 Stalk Lodging Resistance Assessment Methods

Several methods have been developed to assess the lodging resistance of crops. Typically, these methods have been developed by a biologist, agronomist or plant scientists., but lodging is fundamentally a mechanical / structural failure. Therefore, an engineering approach to the problem should provide greater insights and success. From such a perspective, the causes and mechanisms of lodging can be better understood, allowing more complete evaluations of crop properties. A brief review of several approaches to assess lodging resistance is provided here.

#### 1.4.1 Lodging Counts

Lodging counts continue to be one of the most popular methods to assess lodging resistance. In this method, visual lodging counts are conducted, which determine lodging resistance ratings [28]. This method is simple to conduct, but it is unreliable for several reasons. Lodging's numerous confounding factors, such as wind, rain, disease, pests, soil type, topography, and crop management methods, are not accounted for. There are some years in which almost no lodging will occur due to optimal growing conditions and low windspeeds, whereas some years, entire fields lodge regardless of crop strength [27] (e.g., during extreme weather events). To overcome these shortfalls, lodging counts are often averaged across several years, locations, and climates. Such tests are both time-intensive and expensive. Furthermore, root and stalk lodging are often not distinguished [28]

#### 1.4.2 Laboratory Tests

Several laboratory tests have been utilized to evaluate stalk lodging. These primarily feature crushing tests [29, 30], rind penetration resistance [31, 32], and bending tests [33, 34]. Crushing tests are the slowest, induce unnatural failure patterns [35], and studies indicate mixed correlations to lodging [22]. Rind penetration resistance measures the maximum force required to puncture a stalk's rind with a needle. This method is relatively quick but also does not reflect natural loading and has shown mixed correlations to lodging [22]. A study in maize showed that rind penetration resistance predicted less than 20% of the variation in stalk bending strength obtained from three-point bending tests [36]. Three-point bending tests, if performed properly, load stems more naturally and can acquire bending strength and flexural stiffness measurements. Flexural stiffness has been shown to be a good indicator of bending strength in stalks, and therefore stalk lodging resistance [24, 27]. Since lab tests are destructive, require transportation of samples, are time-consuming, and require expensive lab equipment, they are unpopular. A few field-based testing devices have therefore been developed.

1.4.3 Field Devices

The majority of field devices estimate stalk bending strength or flexural stiffness. So far, existing devices were designed solely for either large grains (e.g., maize or sorghum) [35, 37, 38] or small grains (e.g., wheat, rice, or barley) [28, 39]. Devices for large grains test single stems, but with small grains, a single stem typically does not provide enough resistance for reliable measurements. So, devices for small grains test multiple stems at a time.

There have been several similar, but unique, large grain devices. One device referred to here as Guo's device, measures resistance forces as it pulls maize stalks to specific angles [37]. An illustration of Guo's device and its testing operation is provided in Figure 1.4b. To operate Guo's device, a component attaches to the stalk at a defined height to record its angle as the user pulls the component and stalk via a connected belt. As the stalk is pulled to discrete angles, a strain sensor attached to the belt measures the pull force. The maximum equivalent force perpendicular to the stalk is determined and used to evaluate lodging resistance, which has been shown to be correlated to stalk lodging resistance in maize [37].

Two separate, but similar devices, known as the DARLING (Device for Assessing Resistance to Lodging in Grains) and the Stalker were recently developed to test large grains [35, 38]. As depicted in Figure 1.4c and 1.4d, both devices feature a ground footplate attached to a hinge that allows a vertical bar with a control box and a height-adjustable load cell to rotate. To operate both, the user positions the load cell on the stalk and places a foot on the footplate to stabilize the device. Using the Stalker (Figure 1.4c), the user then pushes the vertical bar forward until an LED indicator shows 45°. The maximum force during the test is quantified as the lodging resistance. The DARLING (Figure 1.4d) provides two methods of operation: the stalk can be bent until failure to determine its bending strength, and/or the flexural stiffness can be determined by bending within the linear-elastic range. The DARLING also provides a graphical user interface (GUI) for user control and instant feedback, unlike the Stalker. Both devices have been validated and indicated the ability to categorize crops based on lodging risk [35, 38].

Two similar devices have been developed for small grains. The first device, here called Berry's device, measures the force required to displace an isolated row of crops to discrete angles, as illustrated in Figure 1.4a [28]. The device is composed of a vertical bar with a load cell that is adjusted so it is at half the height of the plants. The resistance force of the plants is then measured at discrete angles, which is used to assess the lodging resistance. Studies indicate Berry's device is capable of categorizing wheat varieties by lodging resistance [40]. Although it was originally developed for wheat, this device has also been modified to examine maize [22]. Compared to existing

methods or devices, testing is considered efficient as it takes about six minutes to perform tests on each plot [28]. However, due to the weight of the battery pack and electronics, it has seen limited use among plant breeders [22].

A more recent device was developed and measures the “critical thrust force” (CTF) of a population of wheat to reach a 45° angle [39]. This device primarily consists of a vertical bar with a three-tooth forked bottom that fixes itself to the ground prior to testing and a dynamometer attached to a height-adjustable, rotating plate for measuring the resistance force. The CTF is used to quantify lodging resistance. Results from an experiment suggest a significant correlation between the CTF and the experimental wind speed that causes displacement of 45° [39].

Both small grain devices and methods do not seem to account for the number of stems that are in contact with the device during testing. Without accounting for the number of stems, comparisons between tests can be misinterpreted and fail to properly evaluate or rank the lodging resistance of hybrids. While difficult to determine, the degree to which the stems interact with one another was also not accounted for. The level of interaction can influence the system mechanics and therefore affect force measurements.

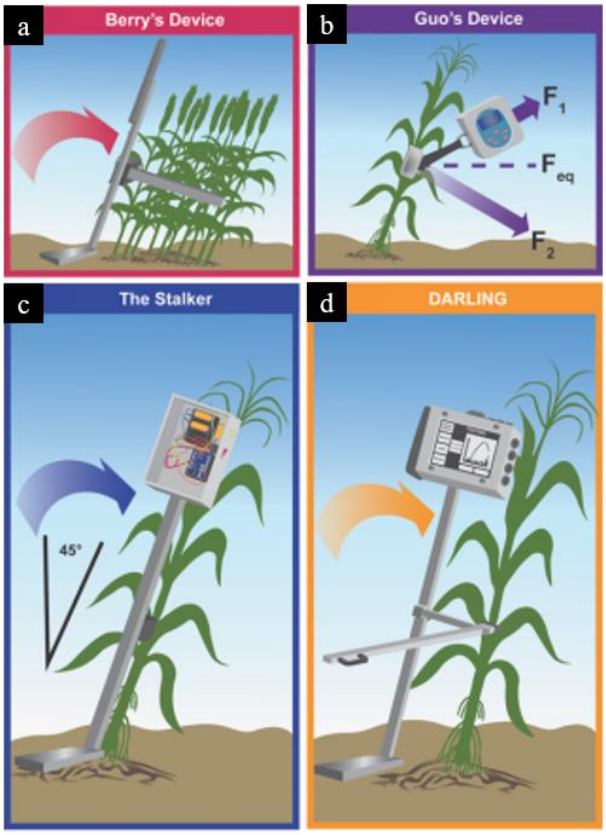


**Figure 1.4** [22] Devices for evaluating stalk bending strength. **(a)** Berry's device tests small grains by measuring multiple crop's resistance force as they bend. **(b)** Guo's device, for large grains, attaches a component to a stalk, which is connected to a belt and strain sensor. After pulling on the belt and bending the stalk to discrete angles, the maximum equivalent force perpendicular to the stalk is determined. This maximum force describes the lodging resistance. **(c)** The Stalker bends a large grain crop to 45° and uses the maximum force as an evaluation of lodging resistance. **(d)** The DARLING (Device for Assessing Resistance to Lodging in Grains), is similar to the Stalker, but can either bend the stalk to failure to determine its bending strength or nondestructively determine its flexural stiffness.

### 1.4.4 A More Efficient Device

There is a pressing need for a rapid, economic method to assess stem lodging [28]. While some devices previously mentioned may be considered quick, none have been able to test entire plots (i.e., hundreds of plants) at a time. This thesis presents the first device of its kind, titled SOCEM (Stiffness of Crops Extrapolation Machine) that is capable of such high throughput measurements. Unlike all previous devices mentioned, the SOCEM has an entirely unique design for rapid data collection while still replicating natural loading. With the SOCEM, accurate assessments of lodging resistance should become economically feasible for plant breeders and farmers. To provide such measurements, the SOCEM requires the use of a mathematical crop model.

### 1.5 Crop Models

To increase understanding of the underlying physics and mechanics of natural lodging, mathematical models have been developed [10, 23, 41-43]. From a simplified, engineering perspective, crops can be represented as vertical, cantilever beams. The equations governing cantilever beam mechanics have been well studied [44-49]. Consequently, equations for cantilever beams undergoing large deflection have been commonly used to model the mechanics of a single crop stem. Previous models have examined the frequency response of crops due to external loading and the likelihood of crop failure [42]. Others, like the model presented by Baker et al. [23], examined if a single wheat crop would lodge or not from the bending moment acting at a single stem's base due to wind. The strength of the stem and root-soil system was considered and determined from stem structures, soil structures, and weather conditions. This model was then expanded upon by Baker et al. [10] to apply to multiple types of crops and consider the effect of the neighboring canopies. The expanded model represents a plant as a two-mass system consisting of the roots and grain head connected by a weightless stem. Interactions between the canopies of neighboring plants are represented as springs attached to the head. Such a model provides complex equations and requires numerous input parameters, but it indicates conditions that may affect lodging risk, at least from a mechanics perspective. Biological factors (e.g. nutrient competition) are generally not accounted for in such closed-form models. Finite-element models have also been developed to investigate the biomechanics of plants [50, 51].

Most closed-form models utilize a single cantilever beam to analyze crops. Crop systems, however, are better represented as a group of interacting cantilever beams as deflections often lead to contact with neighboring crops. A general model involving multiple, separate cantilever beams deflecting into one another does not appear in the scientific literature. Furthermore, existing models of crop systems are generally too complex to utilize with field devices as they require numerous input parameters and/or elliptical integration or numerical methods. Thus, in Chapter 2, a novel mathematical model for understanding the force deflection response of multiple interacting cantilever beams undergoing large deflection is presented.

### 1.6 References

[1] Awika, Joseph M. 2011. "Major Cereal Grains Production and Use around the World." In *Advances in Cereal Science: Implications to Food Processing and Health Promotion*, edited by Joseph M. Awika, Vieno Piironen, and Scott Bean, 1089:1–13. ACS Symposium Series. Washington, DC: American Chemical Society. https://doi.org/10.1021/bk-2011-1089.ch001.

[2] Edgerton, Michael D. 2009. “Increasing Crop Productivity to Meet Global Needs for Feed, Food, and Fuel.” *Plant Physiology* 149 (1): 7–13. https://doi.org/10.1104/pp.108.130195.

[3] “World Agricultural Production | USDA Foreign Agricultural Service.” n.d. Accessed March 15, 2020. https://www.fas.usda.gov/data/world-agricultural-production.

[4] “List of Reports and Publications | 2017 Census of Agriculture | USDA/NASS.” n.d. Accessed March 15, 2020. https://www.nass.usda.gov/Publications/AgCensus/2017/index.php.

[5] M.P, Reynolds, Pietragalla J, and Braun H.J. 2008. *International Symposium on Wheat Yield Potential: Challenges to International Wheat Breeding*. CIMMYT.

[6] Flint-Garcia, S. A., C. Jampatong, L. L. Darrah, and M. D. McMullen. 2003. “Quantitative Trait Locus Analysis of Stalk Strength in Four Maize Populations.” *Crop Science* 43 (February): 13–22. https://doi.org/DOI 10.2135/cropsci2003.0013.

[7] Duvick, Donald N. 2005. “The Contribution of Breeding to Yield Advances in Maize (Zea Mays L.).” *Advances in Agronomy* 86: 83–145.

[8] Berry, P.M., and J. Spink. 2012. “Predicting Yield Losses Caused by Lodging in Wheat.” *Field Crops Research* 137 (October): 19–26. https://doi.org/10.1016/j.fcr.2012.07.019.

[9] Berry, P. M., R. Sylvester-Bradley, and S. Berry. 2007. “Ideotype Design for Lodging-Resistant Wheat.” *Euphytica* 154 (1–2): 165–79. https://doi.org/10.1007/s10681-006-9284-3.

[10] Baker, C.J., M. Sterling, and P. Berry. 2014. “A Generalised Model of Crop Lodging.” *Journal of Theoretical Biology* 363 (December): 1–12. https://doi.org/10.1016/j.jtbi.2014.07.032.

[11] Telkar, Shivkumar. 2017. “Crop Lodging on Cereals: Causes, Effect and Control Introduction.” *Biomolecule Reports*. https://www.researchgate.net/publication/321034837_Crop_Lodging_on_Cereals_Causes_Effect_and_Control_Introduction.

[12] Rajkumara, S. 2008. “Lodging in Cereals - A Review.” *Agricultural Reviews* 29: 55–60.

[13] Carlson, Brad. 2018. “Crop-Loss Research Focuses on Lodging.” Capital Press. 2018. https://www.capitalpress.com/ag_sectors/research/crop-loss-research-focuses-on-lodging/article_d02bb6c2-f9b0-11e8-8bc1-4fad73925f34.html.

[14] Berry, P. M., J. H. Spink, A. P. Gay, and J. Craigon. 2003. “A Comparison of Root and Stem Lodging Risks among Winter Wheat Cultivars.” *The Journal of Agricultural Science* 141 (2): 191–202. https://doi.org/10.1017/S002185960300354X.

[15] Niklas, Karl J., and Hanns-Christof Spatz. 2012. *Plant Physics*. University of Chicago Press.

[16] Berry, Pete M. 2012. “Lodging Resistance in Cereals.” Edited by Robert A. Meyers. Encyclopedia of Sustainability Science and Technology, 6201–6216. https://doi.org/10.1007/978-1-4419-0851-3_228.

[17] Spatz, Hanns-Christof, and Karl J. Niklas. 2013. “Modes of Failure in Tubular Plant Organs.” *American Journal of Botany* 100 (2): 332–36. https://doi.org/10.3732/ajb.1200454.

[18] Baker, C.J., P.M. Berry, J.H. Spink, R. Sylvester-Bradley, J.M. Griffin, R.K. Scott, and R.W. Clare. 1998. “A Method for the Assessment of the Risk of Wheat Lodging.” *Journal of Theoretical Biology* 194 (4): 587–603. https://doi.org/10.1006/jtbi.1998.0778.

[19] Mulder, E. G. 1954. “Effect of Mineral Nutrition on Lodging of Cereals.” *Plant and Soil* 5 (3): 246–306. https://doi.org/10.1007/BF01395900.

[20] Laude, H. H., and Arland W. Pauli. 1956. “Influence of Lodging on Yield and Other Characters in Winter Wheat [1].” *Agronomy Journal* 48 (10): 452–55. https://doi.org/10.2134/agronj1956.00021962004800100005x.

[21] Neenan, M., and J. L. Spencer-Smith. 1975. “An Analysis of the Problem of Lodging with Particular Reference to Wheat and Barley.” *The Journal of Agricultural Science* 85 (3): 495–507. https://doi.org/10.1017/S0021859600062377.

[22] Erndwein, Lindsay, Douglas D. Cook, Daniel J. Robertson, and Erin E. Sparks. 2020. “Field-Based Mechanical Phenotyping of Cereal Crops to Assess Lodging Resistance,” February. https://arxiv.org/abs/1909.08555v3.

[23] Pinthus, Moshe J. 1974. “Lodging in Wheat, Barley, and Oats: The Phenomenon, Its Causes, and Preventive Measures.” In *Advances in Agronomy*, 25:209–63. Elsevier. https://doi.org/10.1016/S0065-2113(08)60782-8.

[24] Berry, P. M., M. Sterling, J. H. Spink, C. J. Baker, R. Sylvester-Bradley, S. J. Mooney, A. R. Tams, and A. R. Ennos. n.d. “Understanding and Reducing Lodging in Cereals.” *Advances in Agronomy*, 217–71.

[25] Stubbs, Christopher J., Yusuf Oduntan, Tyrone Keep, Scott D. Noble, and Daniel J. Robertson. 2020. “The Effect of Self-Loading on the Mechano-Stability and Stalk Lodging Resistance of Plant Stems.” *BioRxiv*, March, 2020.03.21.001727. https://doi.org/10.1101/2020.03.21.001727.

[26] Ash, Mark S., and United States Department of Agriculture Economic Research Service. 1987. *Regional Crop Yield Response for U.S. Grains*. U.S. Department of Agriculture, Economic Research Service.

[27] Robertson, Daniel J., Shien Yang Lee, Margaret Julias, and Douglas D. Cook. 2016. “Maize Stalk Lodging: Flexural Stiffness Predicts Strength.” *Crop Science* 56 (4): 1711. https://doi.org/10.2135/cropsci2015.11.0665.

[28] Berry, P. M., J. Spink, M. Sterling, and A. A. Pickett. 2003. “Methods for Rapidly Measuring the Lodging Resistance of Wheat Cultivars.” *Journal of Agronomy and Crop Science* 189 (6): 390–401. https://doi.org/10.1046/j.0931-2250.2003.00062.x.

[29] Thompson, D. L. 1963. “Stalk Strength of Corn as Measured by Crushing Strength and Rind Thickness.” *Crop Science* 3 (4): 323–29. https://doi.org/10.2135/cropsci1963.0011183X000300040013x.

[30] Zuber, M. S., and C. O. Grogan. 1961. “A New Technique for Measuring Stalk Strength in Corn [1].” *Crop Science* 1 (5): 378–80. https://doi.org/10.2135/cropsci1961.0011183X000100050028x.

[31] Peiffer, J. A., S. A. Flint-Garcia, N. De Leon, M. D. McMullen, S. M. Kaeppler, and E. S. Buckler. 2013. “The Genetic Architecture of Maize Stalk Strength.” *Plos One* 8 (June). https://doi.org/ARTN e67066 10.1371/journal.pone.0067066.

[32] Li, Kun, Jianbing Yan, Jiansheng Li, and Xiaohong Yang. 2014. “Genetic Architecture of Rind Penetrometer Resistance in Two Maize Recombinant Inbred Line Populations.” *BMC Plant Biology* 14 (1): 152. https://doi.org/10.1186/1471-2229-14-152.

[33] Gou, Ling, Ming Zhao, Jian-Jun Huang, Bin Zhang, Tao Li, and Rui Sun. 2008. “Bending Mechanical Properties of Stalk and Lodging Resistance of Maize.” *Acta Agronomica Sinica* 34 (4): 653–61.

[34] Kokubo, Akira, Susumu Kuraishi, and Naoki Sakurai. 1989. “Culm Strength of Barley : Correlation Among Maximum Bending Stress, Cell Wall Dimensions, and Cellulose Content.” *Plant Physiology* 91 (3): 876–82.

[35] Cook, Douglas D., Witold de la Chapelle, Ting-Che Lin, Shien Yang Lee, Wenhuan Sun, and Daniel J. Robertson. 2019. “DARLING: A Device for Assessing Resistance to Lodging in Grain Crops.” *Plant Methods* 15 (1): 102.

[36] Robertson, Daniel J., Margaret Julias, Shien Yang Lee, and Douglas D. Cook. 2017. “Maize Stalk Lodging: Morphological Determinants of Stalk Strength.” *Crop Science* 57 (2): 926. https://doi.org/10.2135/cropsci2016.07.0569.

[37] Guo, Qingqian, Ruipeng Chen, Xiaoquan Sun, Min Jiang, Haifeng Sun, Shun Wang, Liuzheng Ma, Yatao Yang, and Jiandong Hu. 2018. “A Non-Destructive and Direction-Insensitive Method Using a Strain Sensor and Two Single Axis Angle Sensors for Evaluating Corn Stalk Lodging Resistance.” *Sensors* 18 (6): 1852.

[38] Heuschele, D. Jo, Jochum Wiersma, Leonard Reynolds, Amy Mangin, Yvonne Lawley, and Peter Marchetto. 2019. “The Stalker: An Open Source Force Meter for Rapid Stalk Strength Phenotyping.” *HardwareX*, e00067.

[39] Feng, Suwei, Dechuan Kong, Weihua Ding, Zhengang Ru, Gan Li, and Liyuan Niu. 2019. “A Novel Wheat Lodging Resistance Evaluation Method and Device Based on the Thrust Force of the Stalks.” *PLOS ONE* 14 (11): e0224732. https://doi.org/10.1371/journal.pone.0224732.

[40] Spink, J., P.M. Berry, R. Fenwick, and A.P. Gay. 2003. “To Establish Separate Standing Power Ratings for Stem and Root Lodging in the UK Recommended Lists for Wheat.” *HGCA Project Report*, No. 305.

[41] Crook, M. J., and A. R. Ennos. 1994. “Stem and Root Characteristics Associated with Lodging Resistance in Four Winter Wheat Cultivars.” *The Journal of Agricultural Science* 123 (2): 167–74.

[42] Farquhar, T., and H. Meyer-Phillips. 2001. “Relative Safety Factors against Global Buckling, Anchorage Rotation, and Tissue Rupture in Wheat.” *Journal of Theoretical Biology* 211 (1): 55–65. https://doi.org/10.1006/jtbi.2001.2330.

[43] Huang, Mingsen, Yaoming Li, Anya Chen, and Lizhang Xu. 2019. “Numerical Calculation Method of Deflection Deformation of Rice Stalk.” *Applied Sciences* 9 (15): 3125. https://doi.org/10.3390/app9153125.

[44] Barten, H. J. 1944. “On the Deflection of a Cantilever Beam.” *Quarterly of Applied Mathematics* 2 (2): 168–71. https://doi.org/10.1090/qam/10879.

[45] Barten, H. J. 1945. “Corrections to My Paper on the Deflection of a Cantilever Beam.” Quarterly of Applied Mathematics 3 (3): 275–76. https://doi.org/10.1090/qam/13361.

[46] Bisshopp, K. E., and D. C. Drucker. 1945. “Large Deflection of Cantilever Beams.” Quarterly of Applied Mathematics 3 (3): 272–75. https://doi.org/10.1090/qam/13360.

[47] Frisch-Fay, R. 1961. “A New Approach to the Analysis of the Deflection of Thin Cantilevers.” Journal of Applied Mechanics 28 (1): 87–90. https://doi.org/10.1115/1.3640472.

[48] Navaee, S., and R. E. Elling. 1992. “Equilibrium Configurations of Cantilever Beams Subjected to Inclined End Loads.” Journal of Applied Mechanics 59 (3): 572–79. https://doi.org/10.1115/1.2893762.

[49] [50] Wang, T.M. 1968. “Nonlinear Bending of Beams with Concentrated Loads.” Journal of the Franklin Institute 285 (5): 386–90. https://doi.org/10.1016/0016-0032(68)90486-9.

[50] Forell, Greg Von, Daniel Robertson, Shien Yang Lee, and Douglas D. Cook. 2015. “Preventing Lodging in Bioenergy Crops: A Biomechanical Analysis of Maize Stalks

Suggests a New Approach." *Journal of Experimental Botany* 66 (14): 4367–71. https://doi.org/10.1093/jxb/erv108.

[51] Stubbs, Christopher J. 2019. "Computational Modeling of Maize Stems." New York, NY: New York University.

# Chapter 2: Large Deflection Analysis of Multiple, Inline Cantilever Beams Using the Pseudo-Rigid Body Model

## 2.1 Abstract

Numerous natural and synthetic systems can be represented by clusters of individual, but interacting, cantilever beams. A pioneering model of the force-deflection response of multiple, inline, interacting cantilever beams using the pseudo-rigid body model is presented with its accompanying closed-form solution. From the closed-form solution, either the force-displacement response of the system of beams can be determined or the average flexural rigidity of the beams can be determined. The closed-form solution was validated through data triangulation between physical and computational experiments. An analysis of the closed-form solution indicated it is most accurate with deflections less than 50°, but sensitive to errors in input parameters for deflections less than 28°. Accounting for interactions between beams was shown to have a significant effect, especially at large deflections of densely spaced beams. The model may be used in high throughput applications for estimating flexural rigidity or initial design purposes. Several adjustments can be made to the model to more accurately model specific systems.

## 2.2 Introduction

Many natural and synthetic structures can be accurately modeled as a single cantilever beam. Consequently, the force-deflection response of cantilever beams has been well studied [1-6]. However, numerous natural and artificial systems are better represented as a group of mutually interacting cantilever beams. Equations for modeling systems of interacting cantilever beams have not been presented previously. For example, consider the case of a wheat field in which each individual wheat stem can be approximated as a single cantilever beam. When subjected to external forces each wheat stem will contact and interact with its neighbors. The same is true of most agricultural cropping systems. Other natural and synthetic systems with similar attributes include grasses, forests, hair, fur, nanotube arrays, brooms, and brushes. In each of these systems, a method capable of accounting for the interactions between adjacent cantilever beams would be useful. This paper takes a first step towards addressing this problem by providing a closed-form solution to model the force and deflection response of multiple, inline, interacting cantilever beams.

Consider Figure 2.1 which depicts a row of vertical cantilever beams, of equal length, placed directly inline along the x-axis with equal spacing. A rigid body, oriented parallel to the z-axis at a constant height $h$ moves in the x-direction applying a displacing force to each beam at $h$. As each beam deflects it will contact adjacent cantilever beam(s). Each beam will be displaced until the y-

coordinate of the end of each beam is at *h* at which point the beam will pass beneath the rigid body. From hereafter, the rigid body will be referred to as the force bar. The purpose of this paper is to outline a closed-form solution to solve the force-deflection response of systems similar to Figure 2.1 with any number of beams. The solution is compared and validated against physical experiments and a corresponding finite element modeling simulation.

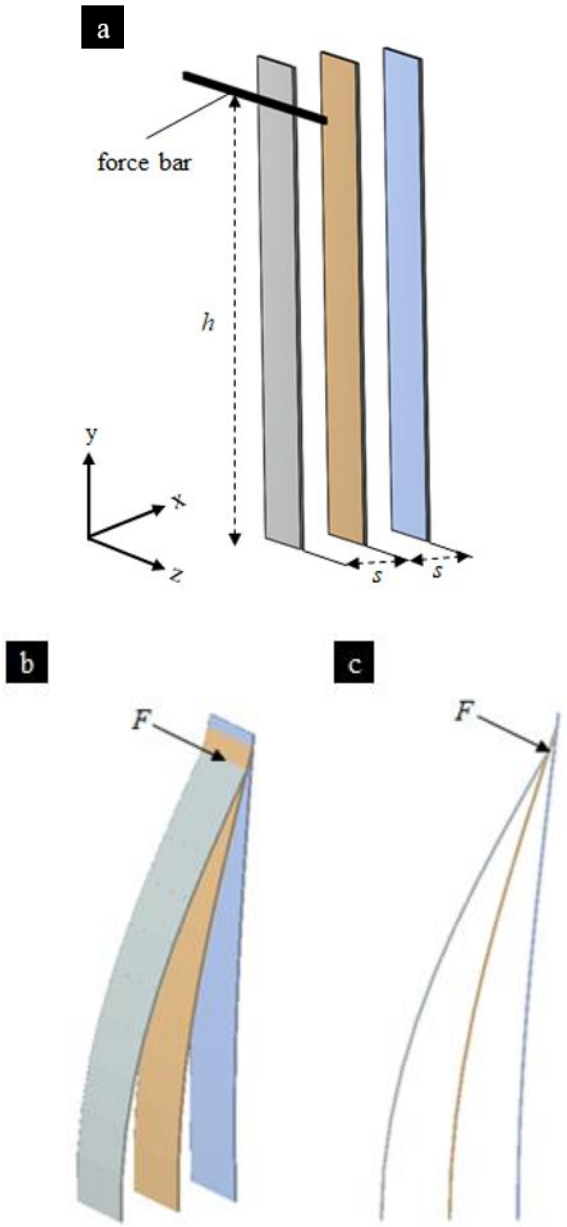


**Figure 2.1** System of inline cantilever beams. **(a)** Undeflected state of three, vertical cantilever beams of equal length fixed directly inline along the x-axis with equal spacing (*s*); the force bar, oriented parallel to the z-axis, is at a known, constant height (*h*). **(b)** Deflected state of the beams as the force bar moves in the x-direction, applying a force (*F*) at *h*. **(c)** Side view of the deflected state.

## 2.3 Theory

Several approaches to solving the large deflection contact problem depicted in Figure 2.1 are plausible. The authors chose to utilize the "pseudo-rigid body model" (PRBM) approach [7, 8]. The PRBM is an approximation method that provides an accurate and efficient manner to analyze large deflection problems. The PRBM method predicts the force-deflection response of flexible members with a combination of rigid bodies, precisely placed pin joint(s), and torsional springs. Each type of flexible member, (e.g., straight cantilever beam, initially curved cantilever beams, pinned-pinned flexible segments, etc.) has a corresponding PRBM with precise pin joint location(s) and torsional spring constant(s). In the current work, we utilize the PRBM of a cantilever beam with a point force applied along its length to determine the force-deflection response of multiple inline, interacting cantilever beams as depicted in Figure 2.1. The derivation of the solution follows. The PRBM for a single cantilever is presented first. A method to solve for the force-displacement response of multiple interacting cantilever beams is then presented.

### 2.3.1 Single Cantilever Beam Model

First consider a single, prismatic cantilever beam of length *l* with a force applied at its free end as depicted in Figure 2.2a. Friction forces and the weight of the cantilever beam are considered negligible for simplification. The beam is assumed to undergo large deflections and the stress-strain response of the material is linear elastic. Note that the following Equations 1-19 are derived in detail in *Compliant Mechanisms* [7]. That derivation is briefly reported here with slight adaptations for the reader's convenience.

The total force applied at the free end *F* has both a horizontal component *P* and a vertical component *nP*. For the vertical force component, a positive *n* describes a compression force acting on the undeflected beam. Thus,

$$F = P\sqrt{n^2 + 1} \tag{1}$$

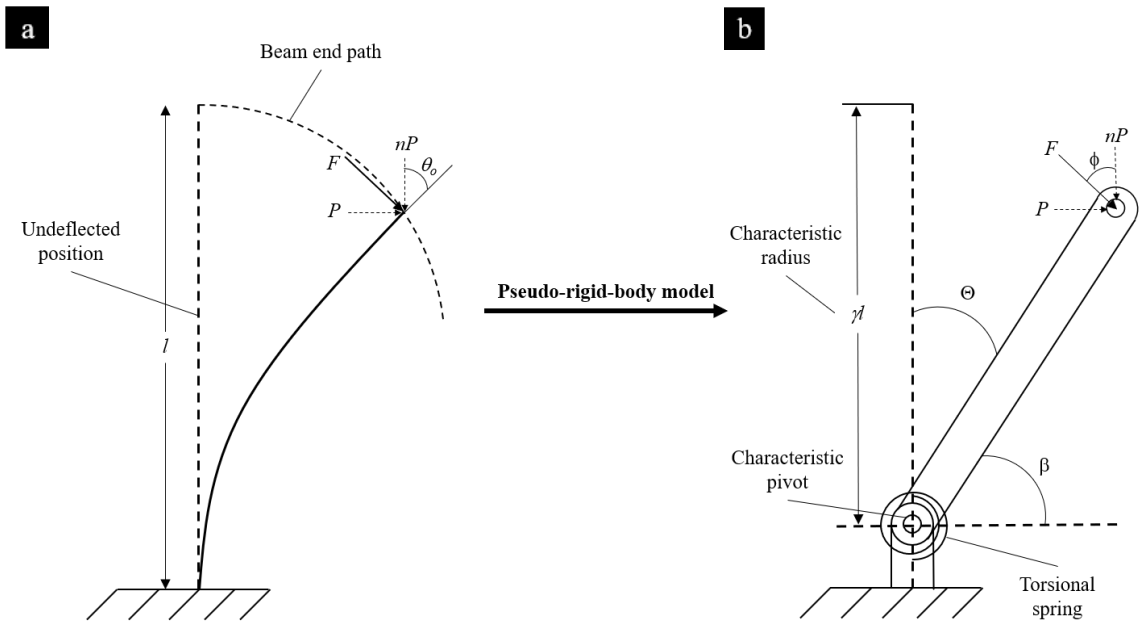


**Figure 2.2 (a)** Cantilever beam undergoing large deflection due to a force applied at the free end with **(b)** its PRBM translation.

As seen in [7], the deflection of the beam pictured in Figure 2.2a can be represented by the PRBM shown in Figure 2.2b. In Figure 2.2b, the flexible cantilever beam is represented by connecting two rigid links with a pin joint and a torsional spring at the characteristic pivot. The characteristic pivot is positioned so that the longer link has a length equivalent to the characteristic radius of the circular path of the free end. The characteristic radius is written as $\gamma l$ where $\gamma$ is known as the characteristic radius factor. As shown by Howell [7], $\gamma$ varies as a function of $\phi$, the angle of the force applied, which is defined with respect to the undeflected axis (vertical axis in this case). From the PRBM,

$$\phi = \tan^{-1}\left(\frac{1}{n}\right) \tag{2}$$

Howell [7] shows that there is a nearly linear relationship between the beam end angle, $\theta_o$, and the PRBM angle, $\Theta$, expressed as

$$\theta_o = c_o \Theta \tag{3}$$

in which $c_o$, the parametric angle coefficient, is a function of $n$.

Fitting a curve to the numerical data Howell [7] provides for $c_o$ results in

$$c_o = (-2 \times 10^{-6})n^4 + (7 \times 10^{-5})n^3 - 0.0009n^2 + 0.006n + 1.241 \quad (4)$$

This allows $\phi$ to properly be corrected from

$$\phi = \frac{\pi}{2} - \theta_o \quad (5)$$

Rearranging Eq. (2) presents

$$n = \frac{1}{\tan(\phi)} \quad (6)$$

The following piecewise function can be used to define $\gamma$ as a function of $n$:

$$\gamma = \begin{cases} 0.841655 - 0.0067807n + 0.000438n^2 & (0.5 < n < 10.0) \\ 0.852144 - 0.0182867n & (-1.8316 < n < 0.5) \\ 0.912364 + 0.0145928n & (-5.0 < n < -1.8316) \end{cases} \quad (7)$$

To account for the force response, the PRBM represents the beam's resistance with the stiffness coefficient, $K_\Theta$, a nondimensionalized torsional spring constant. This stiffness coefficient is related to the transverse force, which causes the link to deflect and produce a torque at the characteristic pivot. The nondimensionalized transverse load index can be written as

$$(\alpha^2)_t = \frac{F_t l^2}{EI} \quad (8)$$

The relationship between $(\alpha^2)_t$ and $\Theta$ is nearly linear, allowing the force-deflection relationship to be described as

$$(\alpha^2)_t = K_\Theta \Theta \quad (9)$$

Like $\gamma$, $K_\Theta$ can be described as a function of $n$:

$$K_\Theta = \begin{cases} 3.024112 + 0.121290n + 0.003169n^2 & (-5 < n \leq -2.5) \\ 1.967647 - 2.616021n - 3.738166n^2 \\ -2.649437n^3 - 0.891906n^4 - 0.113063n^5 & (-2.5 < n \leq -1) \\ 2.654855 - 0.509896 \times 10^{-1}n + 0.126749 \times 10^{-1}n^2 \\ -0.142039 \times 10^{-2}n^3 + 0.584525 \times 10^{-4}n^4 & (-1 < n \leq 10) \end{cases} \quad (10)$$

It is important to note that both $K_\Theta$ and $\gamma$ are estimations with accuracy limits that are in terms of the maximum $\Theta$, as described in [7]. The following approximation of $K_\Theta$ can also be implemented to simplify the solution process:

$$K_\Theta \approx \pi\gamma \tag{11}$$

Recall that the transverse force $F_t$ produces a torque at the characteristic pivot, expressed as

$$T = F_t \gamma l \tag{12}$$

This torque can also be written as

$$T = K\Theta \tag{13}$$

where $K$ is the torsional spring constant (not to be confused with the stiffness coefficient, $K_\Theta$). Setting Eq. (12) and Eq. (13) equal and rearranging for $F_t$ yields

$$F_t = \frac{K\Theta}{\gamma l} \tag{14}$$

Combining Eq. (8) and Eq. (9),

$$\frac{F_t l^2}{EI} = K_\Theta \Theta \tag{15}$$

Inserting Eq. (14) into the above then gives

$$\frac{K\Theta l}{\gamma EI} = K_\Theta \Theta \tag{16}$$

Equation 16 can then be rearranged for $K$ or the flexural rigidity, $EI$, expressed below respectively:

$$K = \gamma K_\Theta \frac{EI}{l} \tag{17}$$

$$EI = \frac{Kl}{\gamma K_\Theta} \tag{18}$$

Another approximation for $K$ can be expressed by substituting Eq. (11) into Eq. (17), yielding

$$K \approx \pi\gamma\frac{EI}{l} \tag{19}$$

2.3.2 Multiple Inline Interacting Cantilever Beam Model

The equations above apply to a single cantilever beam. We now address the simultaneous deflection of multiple interacting cantilever beams that are inline, allowing the beams to come into contact during deflection. The closed-form solution to this problem is derived below.

Consider the case previously shown in Figure 2.1, in which three identical, vertical cantilever beams of length $l$ are placed with equal spacing $s$ along the x-direction. Let the force bar, oriented parallel to the z-axis, move across the beams, applying a force at a known, constant height $h$ that deflects all three beams. While this system is dynamic in nature, there will be a point at which the frontmost beam is at its maximum deflection (i.e., immediately prior to passing under the force bar and returning to its vertical position). The applied force at this point will be referred to as $F_{peak}$. The PRBM of this specific scenario is depicted in Figure 2.3 while the PRBM free body diagrams of each individual beam are illustrated in Figure 2.4. For clearer visualization, the geometry is often described with respect to the angle, $\beta$, rather than $\Theta$, in Figure 2.4 and equations.

$$\beta_i = \frac{\pi}{2} - \Theta_i \tag{20}$$

While only three beams are being examined, the following derivation will be generalized to work with any number of beams.

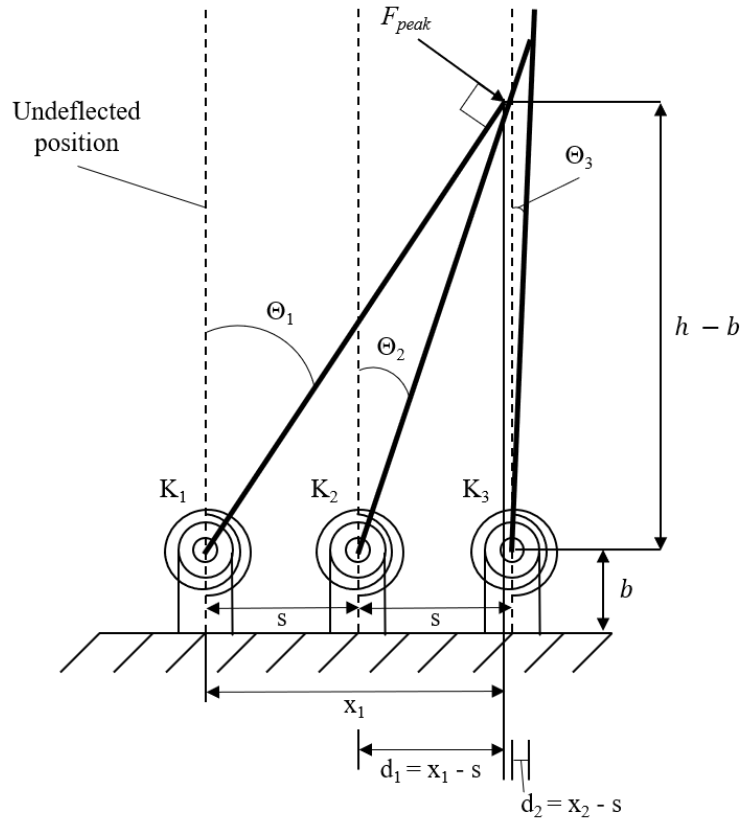


**Figure 2.3** Side view showing the PRBM at the first beam's most deflected state. Beams of equal length, *l*, are placed with equal spacing, *s*, along the x-axis.

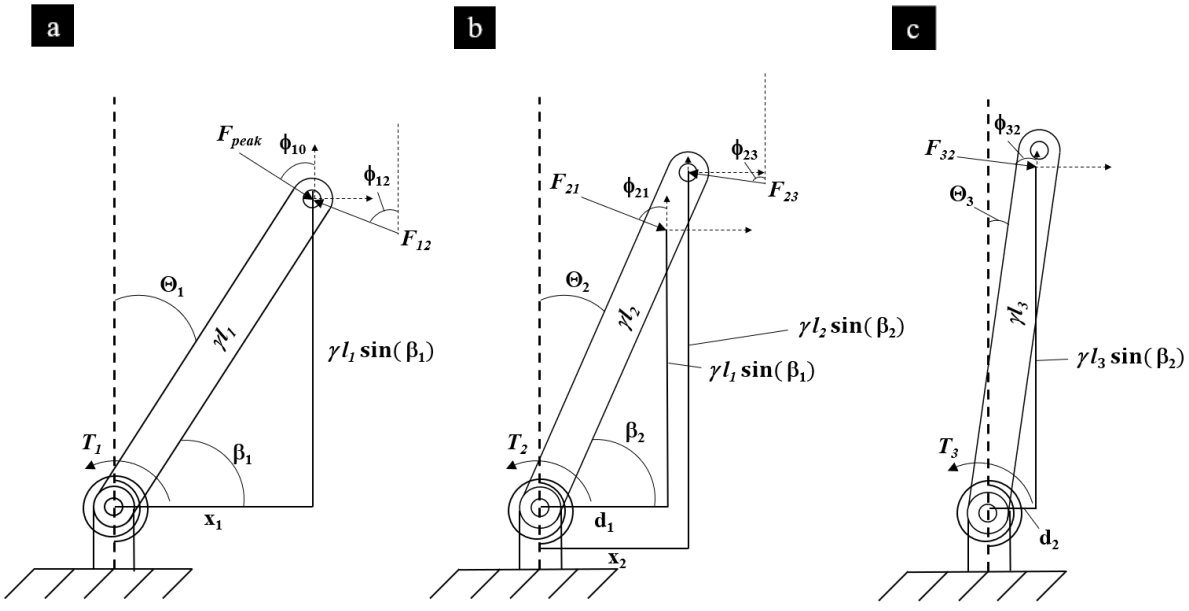


**Figure 2.4** The PRBM free body diagrams for **(a)** the first beam, **(b),** middle beam, and **(c)** last beam.

To obtain an expression for $F_{peak}$ or $EI$, the angles of deflection ($\Theta$) and locations of the forces are required. Starting with the first beam, $\Theta_1$ in radians becomes

$$\Theta_1 = \frac{\pi}{2} - \sin^{-1}\left(\frac{h - b_1}{\gamma_1 l}\right) \tag{101}$$

where $b$, the base of the PRBM, is expressed as

$$b_i = (1 - \gamma_i)l \tag{22}$$

To implement Eq. (21), a value for $\gamma_1$ must be selected. Initially, the assumption in which the applied force is always acting horizontally will be made, yielding $n_1 = 0$ and $\gamma_1 = 0.8517$. With this simplifying assumption, an initial estimate for $\Theta_1$ can be made. While maintaining this $\Theta_1$, the assumption in which the applied force is always acting perpendicularly to the first beam will now be made. Using Eq. (3) and Eq. (5) then provides $\phi_1$. Given $\phi_1$, a value for $n_1$ can be obtained from Eq. (6), which can then be inputted to update $\gamma_1$. Changing $\gamma_1$ will then require $\Theta_1$ to also be updated. This will restart the process of determining $\phi_1$. This process should be repeated until $\gamma_1$ converges, which can easily be implemented using a while loop in a computer program. The final $n_1$ should also be utilized to update $K_{\Theta 1}$, which is needed to determine the first beam's $K$ (if $EI$ is known) from Eq. (17). For this analysis, it is assumed that all beams in the system possess the same $K$ for simplification.

To determine the geometry of the remaining beams and forces, the x-coordinate of the first beam's end point, $x_1$, at its maximum deflection is required. With $i = 1$, this is simply

$$x_i = \gamma_i l \cos(\beta_i) \tag{23}$$

As shown in Figure 2.3, note that the horizontal distance a beam extends past the next beam's origin is expressed as

$$d_i = x_i - s \qquad (while\ x_i > s) \tag{24}$$

If the $x_i > s$ condition is not met, the $i^{th}$ beam will not contact the next ($i$+1) beam prior to the first beam passing below the force bar (i.e., disengaging) and returning to its vertical position. With Eq. (24), the angle of deflection *for the non-initial beams* ($i > 1$) can be expressed as

$$\Theta_i = \frac{\pi}{2} - \tan^{-1}\left(\frac{\gamma_{i-1} l \sin(\beta_{i-1})}{d_{i-1}}\right) \tag{25}$$

Recall that from Newton's third law [9], every force has an equal and opposite reaction, so as the $i^{th}$ beam exerts a force on the $i$+1 beam, the $i$+1 beam will exert a force of equal magnitude back. This supports the use of the following notation,

$$F_{i,i+1} = -F_{i+1,i} \tag{26}$$

Note that $F_{i,\,i+1}$ corresponds to the force acting on the $i^{th}$ beam induced by the $i$+1 beam. The force vectors of equal magnitude acting between beams $i$ and $i$+1 will be assumed to act at the mean perpendicular angle of the $i$ and $i$+1 beams. Thus,

$$\phi_{i,i+1} = \frac{\phi_i + \phi_{i+1}}{2} \tag{27}$$

Where $\phi$ can be found using Eq. (5). Note that $\phi_{i,i+1} = \phi_{i+1,i}$. For each beam, $\phi_{i,i+1}$ should be used to determine $n_i$ in order to update each beam's $\gamma_i$.

The solution process for $F_{peak}$ begins by analyzing the final beam as it is the only beam with just one force and a torque acting on it. From there, it is possible to backsolve to $F_{peak}$. Consider the moments at the final beam's torsional spring. A moment in the counterclockwise direction is defined as positive. As illustrated in the Figure 2.4,

$$\sum M_3 = T_3 + F_{32y} d_2 - F_{32x}\left(\gamma_2 l \sin(\beta_2)\right) = 0 \tag{28}$$

Let the force components be defined as

$$F_x = F \sin(\phi) \tag{29}$$

$$F_y = -F \cos(\phi) \tag{30}$$

Substituting the force components into Eq. (28) gives

$$T_3 - F_{32}\left(\cos\left(\phi_{32}\right) d_2 + \sin(\phi_{32})\, \gamma_2 l \sin(\beta_2)\right) = 0 \tag{31}$$

Inserting $T_3$ using Eq. (13) and solving for $F_{32}$ yields

$$F_{32} = \frac{K_3 \Theta_3}{\cos\left(\phi_{32}\right) d_2 + \sin(\phi_{32})\, \gamma_2 l \sin(\beta_2)} \tag{32}$$

In general terms, the *final beam's resistive force* can be expressed as

$$F_{i,i-1} = \frac{K_i \Theta_i}{\cos\left(\phi_{i,i-1}\right) d_{i-1} + \sin(\phi_{i,i-1})\, \gamma_{i-1} l \sin(\beta_{i-1})} \tag{33}$$

The moments acting at the middle beam's torsional spring can be expressed as

$$\sum M_2 = T_2 + F_{21y} d_2 - F_{21x}\left(\gamma_1 l \sin(\beta_1)\right) + F_{23y} x_2 - F_{23x}\left(\gamma_2 l \sin(\beta_2)\right) = 0 \tag{34}$$

Recall that $F_{23} = -F_{32}$ so

$$F_{23x} = -F_{32x} = -F_{32}\sin(\phi_{32}) \tag{35}$$

$$F_{23y} = -F_{32y} = F_{32}\cos(\phi_{32}) \tag{36}$$

After substituting $T_2$ and the force components, Eq. (34) can be rearranged for $F_{21}$ as shown below:

$$F_{21} = \frac{K_2 \Theta_2 + F_{32}\left(\cos\left(\phi_{32}\right) x_2 + \sin\left(\phi_{32}\right)\left(\gamma_2 l \sin(\beta_2)\right)\right)}{\cos\left(\phi_{21}\right) d_1 + \sin(\phi_{21})\, \gamma_1 l \sin(\beta_1)} \tag{37}$$

In general terms, the *resistive force of any middle beam* can be expressed as

$$F_{i,i-1} = \frac{K_i \Theta_i + F_{i+1,i}\left(\cos\left(\phi_{i+1,i}\right) x_i + \sin\left(\phi_{i+1,i}\right)\left(\gamma_i l \sin(\beta_i)\right)\right)}{\cos\left(\phi_{i,i-1}\right) d_{i-1} + \sin(\phi_{i,i-1})\, \gamma_{i-1} l \sin(\beta_{i-1})} \tag{38}$$

Using the same methods as done for the middle beam, $F_{peak}$ can be solved for from the sum of the moments acting at the first beam's torsional spring, yielding

$$F_{peak} = \frac{K_1 \Theta_1 + F_{21}\left(\cos\left(\phi_{21}\right) x_1 + \sin\left(\phi_{21}\right)\left(\gamma_1 l \sin(\beta_1)\right)\right)}{\cos\left(\phi_{10}\right) x_1 + \sin(\phi_{10})\, \gamma_1 l \sin(\beta_1)} \tag{39}$$

To then arrive at an expression for *EI*, an expression for *K* must be derived first. Since $K_\Theta$ and $\gamma$ both don't vary much over a vast range of $\phi$, the assumption that each beam possesses the same *K* will still be held. Under this simplifying assumption, each beam's resistive force expression can be expressed as $\frac{F_{i,i-1}}{K}$.

Notice that the first beam's resistive force expression becomes,

$$\frac{F_{peak}}{K} = \frac{\Theta_1 + \frac{F_{21}}{K}\left(\cos\left(\phi_{21}\right) x_1 + \sin\left(\phi_{21}\right)\left(\gamma_1 l \sin(\beta_1)\right)\right)}{\cos\left(\phi_{10}\right)x_1 + \sin(\phi_{10})\,\gamma_1 l \sin(\beta_1)} \tag{40}$$

where $\frac{F_{21}}{K}$ remains on the right side since its value can be substituted in.

Rearranging for *K* then provides

$$K = \frac{F_{peak}\left(\cos\left(\phi_{10}\right)x_1 + \sin(\phi_{10})\,\gamma_1 l \sin(\beta_1)\right)}{\Theta_1 + \frac{F_{21}}{K}\left(\cos\left(\phi_{21}\right) x_1 + \sin\left(\phi_{21}\right)\left(\gamma_1 l \sin(\beta_1)\right)\right)} \tag{41}$$

which can be inserted into Eq. (18), giving *EI*.

While the above equations were derived from the perspective of the first beam's maximum deflected state at the force bar height *h*, this approach was taken for simplicity and to provide context in the upcoming sections. By virtually adjusting *h* in small increments, the equations can be implemented as a function of *x*. More specifically, virtually placing the force bar at the beam height *l* initially and incrementally decreasing the force bar height until the actual *h* or desired deflection is reached, results in a near continuous plot of the applied *F*.

Plotting the reaction force *F* as the force bar moves across the identical beams, will result in a plot similar to Figure 2.5. Notice that the force will reach an initial peak or maximum force ($F_{peak}$) when the first beam has reached its maximum deflection, as shown in Figure 2.6a. Immediately after the first beam deflects under the force bar, *F* will sharply drop off and then continue to rise until the second beam reaches its maximum deflection, shown in Figure 2.6b. With identical beams and equal spacings, at this point, *F* will have returned to the same $F_{peak}$ seen at the first beam's maximum deflection. These equivalent $F_{peak}$ values will continue to be observed as long as the number of beams in contact at the frontmost beam's maximum deflection does not decrease. Near the end of a set of beams, the number of contacting beams will be reduced as shown in Figure 2.6c and Figure 2.6d. As a result, the corresponding *F* peaks shown in Figure 2.5's plot, are lower than the initial $F_{peak}$. It is expected that $F_{peak}$ will occur *m* times, following

$$m = (t + 1) - u \tag{42}$$

where *t* is the total number of beams and *u* is the maximum number of beams in contact at the frontmost beam's maximum deflection. From a system's geometry, *u* can be determined.

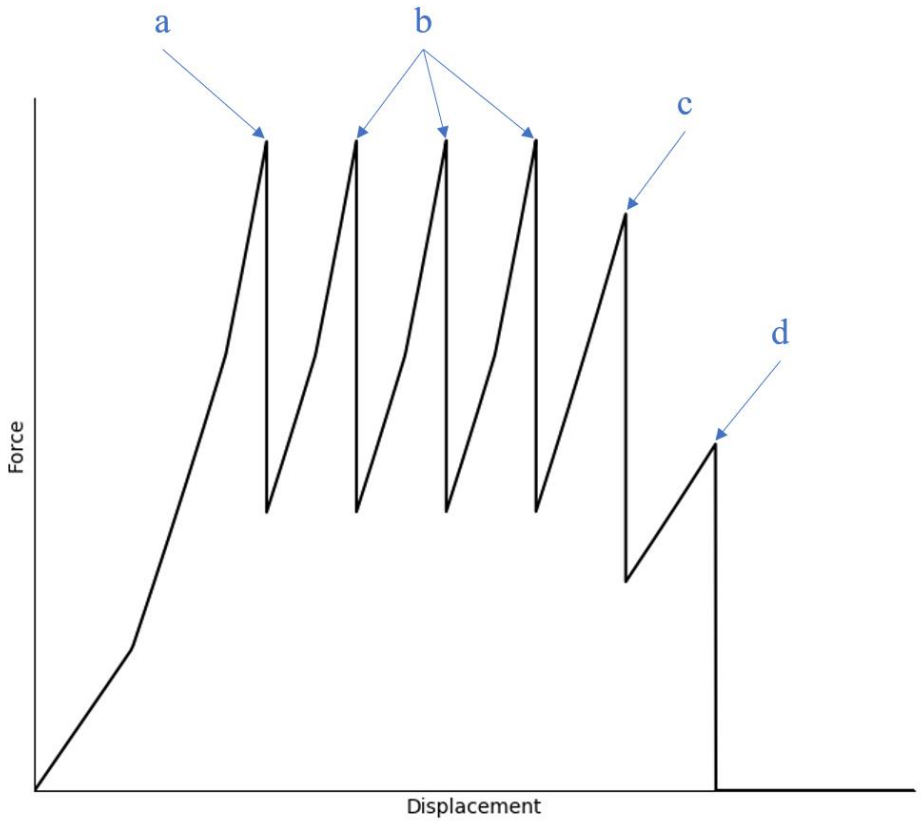


**Figure 2.5** An ideal plot of the total force response *F* as the force bar moves across six beams. The state of the beams at points **a**, **b**, **c**, and **d** can be seen in Figure 2.6. $F_{peak}$ at point **a** is equivalent to those at **b**.

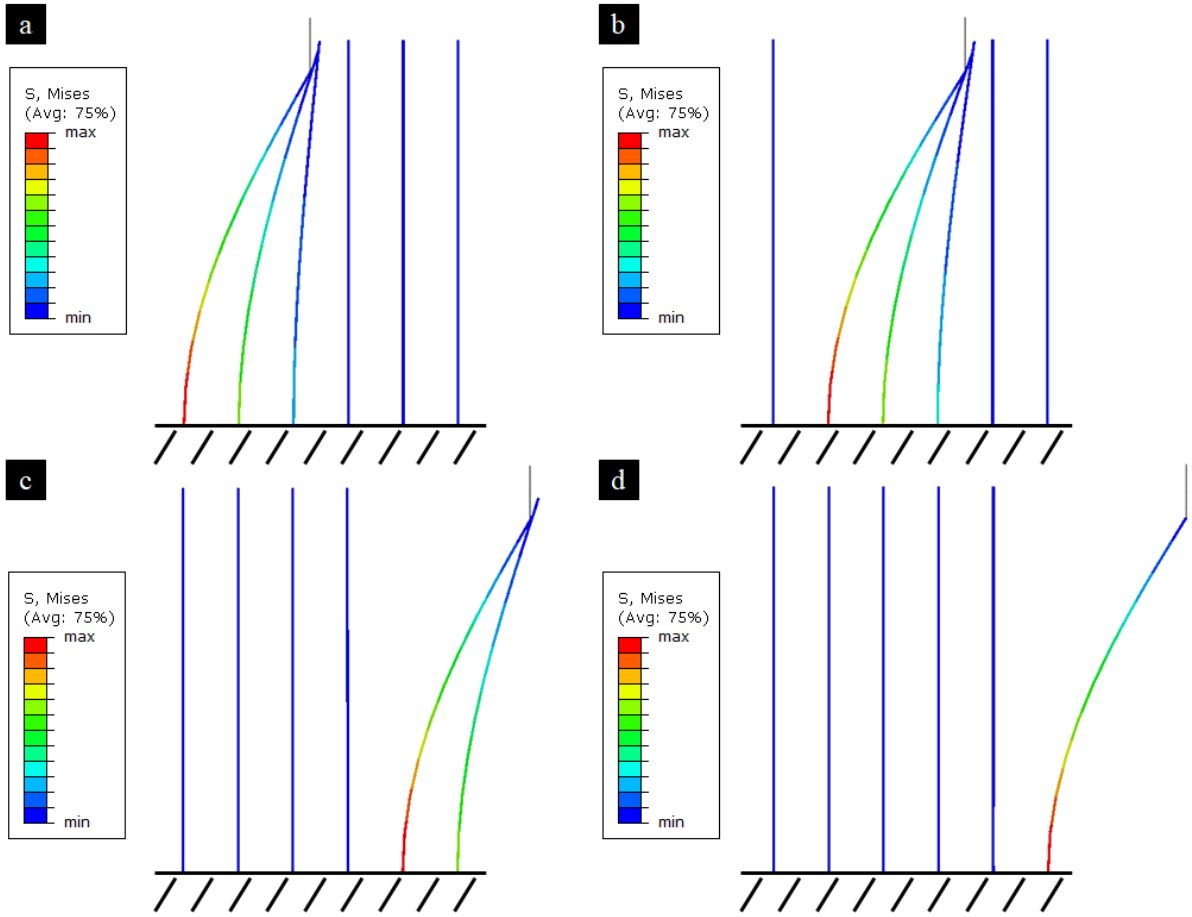


**Figure 2.6** States of the six-beam system as the force bar moves through. **(a)** State of the system at the first beam's maximum deflection. **(b)** State at the deflection of the second beam's maximum deflection; for this case of six beams, the contact state is equivalent for the third and fourth beam. **(c)** State at the second to last beam's maximum deflection. Notice the number of beams in contact has been reduced to two. **(d)** Maximum deflection of just the final beam.

From the closed-form solution, the force response can be solved for if given *EI*, the length of the beams (*l*), spacing distance (*s*), and the height of the force bar (*h*). Alternatively, the closed-form solution can be used to solve for *EI*, given the force response, *l*, *s*, and *h*.

### 2.4 Data Triangulation to Assess Accuracy of the Closed-Form Solution

The closed-form solution method from the Multiple Inline Interacting Cantilever Beam Model presented above was validated through physical and computational finite element experiments. Across the experiments, all input parameters were varied to assess the robustness of the closed-form solution. Details of the physical experiments are presented first followed by a description of the finite element model experiments.

2.4.1 Physical Experimental Setup

The PRBM solution method presented above was validated through physical experiments. As illustrated in Figure 2.7, six rectangular sheet metal strips were securely placed directly inline, and equally spaced by width *s*. A rectangular aluminum bar (i.e., a rigid body force bar) oriented perpendicular to the sheet metal strips at height *h* was attached to a load and displacement sensor. The force bar was then slowly driven across the beams, causing each beam to deflect and eventually pass under the bar. The force-displacement response of the bar was analyzed and the closed-form solution was used to estimate the *EI* of the beams. Five different sets of beams underwent testing. The estimated *EI* values were then compared to actual *EI* values for each set of beams. Actual *EI* values were determined from three-point bending tests and calipers measurements.

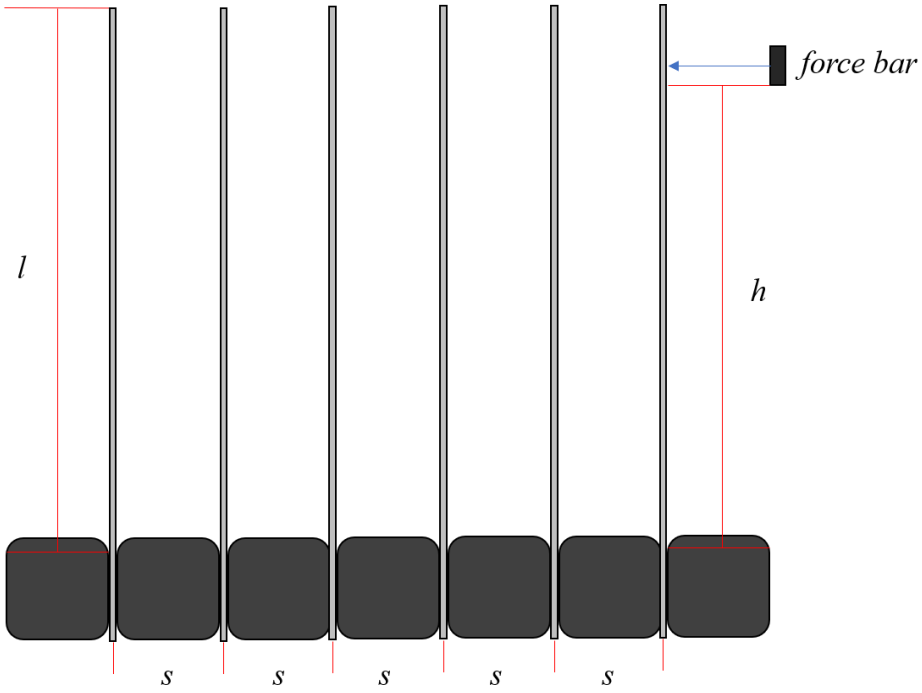


**Figure 2.7** Diagram of experimental setup. *l* - effective length of beams, *h* - minimum effective height of the force bar, *s* - width of spacing bars.

The geometric and material properties of the beams were acquired as described below. Beam lengths were measured by the same individual with an imperial ruler, while the width and thickness were measured with a set of digital calipers. Four randomly selected rectangular strips cut from the same sheet metal stock, underwent individual three-point bending tests using an Instron universal testing machine (Model 5965, Instron Crop., Norwood, MA). The Instron software (Bluehill 3.0) was used for instrumentation control and data acquisition of displacement, force, and the calculation for *E*.

All tests limited displacement to prevent yielding or other physical deformation. In particular, the supports were spaced 10 cm apart and the loading anvil was lowered at a rate of 0.13 cm $s^{-1}$. The test stopped at a beam displacement of 0.3 cm. The mean *E* of the four beams was then calculated and assigned to all corresponding beams cut from the same stock. A total of five sets of beams were created. Each set consisted of six beams and each set was constructed to possess a unique *EI* value. Table 2.1 displays the breakdown of *EI* and accompanying statistics for each set of beams.

**Table 2.1** Mean properties (± SD.) of each set of sheet metal test beams.

| ***Set*** | ***Material*** | ***EI (N mm$^2$)*** | ***E (N/mm$^2$)*** | ***I (mm$^4$)*** |
|---|---|---|---|---|
| A | Aluminum | 41900 ± 1480 | 82000 ± 2560 | 0.511 ± 0.009 |
| B | Aluminum | 63000 ± 1990 | 82000 ± 2560 | 0.769 ± 0.003 |
| C | Aluminum | 111000 ± 2820 | 79000 ± 1900 | 1.41 ± 0.011 |
| D | Steel | 154000 ± 5930 | 200000 ± 6756 | 0.772 ± 0.014 |
| E | Aluminum | 335000 ± 6000 | 74500 ± 919 | 4.49 ± 0.059 |

Each set of beams described in Table 2.1, were subjected to three tests with different beam to beam spacings (*s*). The first test had a beam to beam spacing of 19.1 mm, the second a spacing of 24.9 mm, and the third a spacing of 49.9 mm. The height of the force bar was adjusted so that the beams would not yield but they would come into contact with at least one other beam during the test. Across the 15 experiments (5 sets of beams × 3 spacings) the height of the force bar ranged from 5.08 - 16.51 mm below the top of the beams. Table 2.2 summarizes the testing conditions for all 15 experimental tests.

**Table 2.2** Conditions for each physical experiment test. Note that the effective *l* and *h* (with respect to the spacing bars) are listed. The expected peaks refer to the number of maximum force peaks that occur for a test with six beams.

| Set | *EI* (N mm$^2$) | *s* (mm) | *l* (mm) | *h* (mm) | Expected peaks |
|---|---|---|---|---|---|
| $A_1$ | 41900 | 24.9 | 180 | 167 | 4 |
| $B_1$ | 63000 | 24.9 | 180 | 165 | 4 |
| $C_1$ | 111000 | 24.9 | 231 | 219 | 4 |
| $D_1$ | 154000 | 24.9 | 205 | 191 | 4 |
| $E_1$ | 335000 | 24.9 | 231 | 219 | 4 |
| $A_2$ | 41900 | 49.9 | 180 | 167 | 5 |
| $B_2$ | 63000 | 49.9 | 180 | 165 | 5 |
| $C_2$ | 111000 | 49.9 | 231 | 219 | 5 |
| $D_2$ | 154000 | 49.9 | 205 | 191 | 5 |
| $E_2$ | 335000 | 49.9 | 231 | 224 | 5 |
| $A_3$ | 41900 | 19.1 | 186 | 175 | 3 |
| $B_3$ | 63000 | 19.1 | 186 | 175 | 3 |
| $C_3$ | 111000 | 19.1 | 237 | 225 | 3 |
| $D_3$ | 154000 | 19.1 | 211 | 198 | 3 |
| $E_3$ | 335000 | 19.1 | 237 | 225 | 3 |

### 2.4.2 *EI* Estimation

For each test condition, *EI* was estimated from the closed-form solution using a Python script that follows the process outlined in 2.3.2 Multiple Inline Interacting Cantilever Beam Model. The input parameters to the script were the peak force ($F_{peak}$) from the experimental tests, beam to beam spacing (*s*), beam length (*l*), and height of the force bar (*h*). The load cell utilized in the experimental setup only measured the horizontal component of the force exerted on the force bar. The total force exerted on the force bar was estimated utilizing the measured horizontal force component and the beam end angle, $\theta_o$. Each experimental test also experienced several peak forces due to sequential engagement and disengagement of the beams with the force bar, as described in Figure 2.5. The peak force ($F_{peak}$) used to estimate *EI* was calculated by averaging the first *m* number of expected peak forces (see Table 2.2) from each test according to Eq. (42).

### 2.4.3 Finite Element Model Development and Validation

The closed-form solution was further investigated using a parametric finite element model (FEM) of multiple interacting cantilever beams. The FEM was validated against physical experimental data with one, two, three, and six beams, as shown in Figure 2.8. The 2-dimensional

model was developed in Abaqus/CAE 2019 [10-12]. The metal beams were modeled as 2-noded linear beam elements, and the loading plate was modeled as a discrete rigid. All contact was modeled as frictionless. Material and contact damping was used to aid in force-displacement stability and was confirmed to have a negligible effect as compared to the internal potential energy of the beams. The model was analyzed as a dynamic simulation in Abaqus/Explicit 2019, capturing full contact and non-linear effects [10-12].

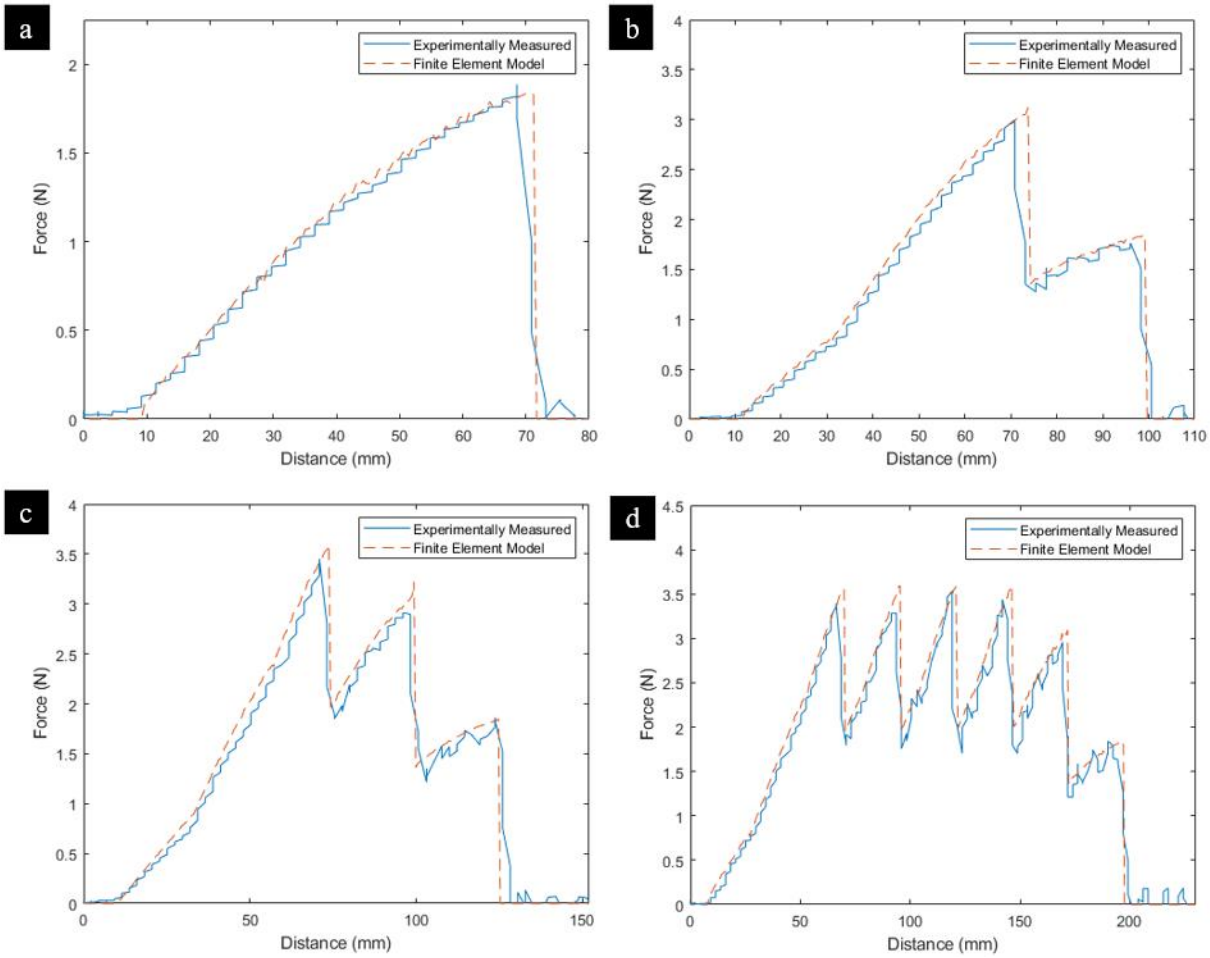


**Figure 2.8** Validation of the finite element model (FEM). The experimentally measured and FEM horizontal force-displacement curves of the one **(a)**, two **(b)**, three **(c)**, and six **(d)** beam experiments.

## 2.4.4 FEM Experiments

Once the FEM was validated, it was used to assess the accuracy of the closed-form solution. As a first step in this process and to create preliminary insight into the closed-form solution's predictivity, an in-depth analysis of its force-displacement response was examined for a single case. In particular, the case of six beams of $EI$ = 63000 N mm$^2$, $s$ = 24.9 mm, and $l$ = 180 mm being

deflected by a force bar driven at $h$ = 165 mm was analyzed via physical experimentation, via a FEM simulation, and with the closed-form solution. The force-displacement response from each method was then compared.

After the preliminary, single case, analysis described in the preceding paragraph, a more comprehensive data triangulation [13, 14] experiment was conducted. In particular, one researcher simulated FEMs of eight identical, inline beams ($l$ = 180 mm) at 10 different $s$ values undergoing deflection due to 10 unique $h$ values. Thus, a total of 100 FEMs were produced (*10* $s$ values × 10 $h$ values = 100). For all beams and simulations, $EI$ was held constant at 63000 N mm$^2$. A summary of the input parameters for the models is provided in Table 2.3. Note that the amount of deflection depends on the ratio of $h$ to $l$.

**Table 2.3** Parameters across the 100 FEM simulations (10 $s$ × 10 maximum deflections). Each simulation consisted of eight identical, inline beams of $l$ = 180 mm and $EI$ = 63000 N mm$^2$.

| ***s* (mm)** | ***h* (mm)** | ***h/l*** | **Max $\Theta$ (º)** |
|---|---|---|---|
| 2.00 | 89.81 | 0.50 | 67.2 |
| 6.22 | 97.36 | 0.54 | 64.0 |
| 10.44 | 104.91 | 0.58 | 60.4 |
| 14.67 | 112.46 | 0.63 | 56.8 |
| 18.89 | 120.01 | 0.67 | 53.2 |
| 23.11 | 127.56 | 0.71 | 49.4 |
| 27.33 | 135.11 | 0.75 | 45.4 |
| 31.56 | 142.66 | 0.79 | 41.1 |
| 35.78 | 150.21 | 0.84 | 36.5 |
| 40.00 | 157.76 | 0.88 | 31.3 |

The 100 force response plots (10 $s$ values × 10 $h$ values) and the corresponding system dimensions ($s$, $l$, and $h$) were then given to another researcher. This researcher then utilized the closed-form solution to backsolve for all 100 $EI$ values using two methods. Both methods inputted the dimensions but used different sources for the input force. The closed-form solution requires $F_{peak}$ or the force just before the beam is no longer in contact with the force bar. $F_{peak}$ can be determined by either analyzing the total force or x-component force, but using the x-component force requires an additional step involving further assumptions. The observed $F_{x\,peak}$ uses the corrected $\phi$ to estimate $F_{peak}$. Since $\phi$ is an estimation, the $F_{peak}$ calculated from $F_{x\,peak}$ may not fully align with the direct $F_{peak}$. Therefore, both $F_{peak}$ values and the corresponding system dimensions ($s$, $l$, and $h$) were inputted into the closed-form solution to examine the difference in results. Unlike the physical

experiment, $F_{peak}$ and $F_{x\,peak}$ were obtained from the first observed force peak as the following peaks should be identical with identical FEM beams. The backsolved *EI* values from both methods were then compared to the actual *EI* values used in the FEMs.

## 2.5 Results

The results are presented in three sections. A comparison between the physical experiments and the closed-form solution is provided first. A single case examination comparing the closed-form solution force-displacement response to a corresponding physical experiment and FEM simulation is then provided. Lastly, the closed-form solution is assessed using 100 FEMs with various input parameters.

### 2.5.1 Physical Experiments vs. Closed-Form Solution

From the physical experiment outlined in 2.4.1 Physical Experiment Setup, the predicted *EI* values computed from the closed-form solution were plotted against the corresponding, measured *EI*, as shown in Figure 2.9. Fitting a linear regression (blue line) to the plot provides $R^2 = 0.99$ and a slope of 0.945, indicating the closed-form solution generally underpredicted *EI*. The "ideal" line describing the theoretical case in which all predicted *EI* were equivalent to all measured *EI*, has been shown in red. Assuming the mean, measured *EI* to be the true value, the closed-form solution yielded a mean absolute percent error of 10.92% with a standard deviation of 6.98%.

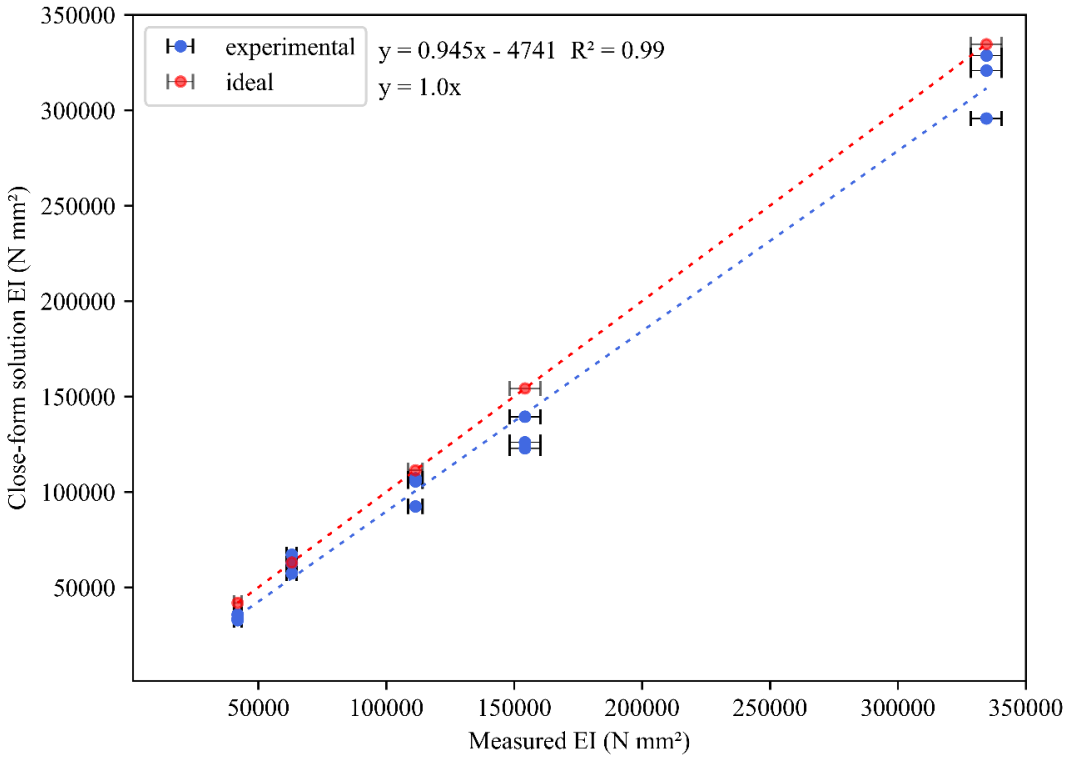


**Figure 2.9** *EI* linear regression of closed-form solution. The predicted *EI* (N mm$^2$) obtained from the closed-form solution plotted against the measured *EI* (N mm$^2$). Linear regression blue line shows $R^2$ = 0.99 and slope of 0.945. Error bars represent the standard deviation of the measured *EI*. The red line shows the theoretical, ideal case of $y = x$ to indicate accuracy.

### 2.5.2 Force Response Comparison

The six-beam horizontal force response ($F_x$) was plotted against the $x$ displacement from the physical experiment (blue), FEM simulation (green), and two closed-form solution predictions (orange - closed-form solution and red - closed-form solution with correction factor) in Figure 2.10. The force response between the physical experiment, FEM, and closed-form solution prediction are in fairly good agreement, but the closed-form solution overpredicts the force peaks and displacement at maximum deflection. Recall that the closed-form solution utilizes straight, rigid segments from the PRBM, which were not designed to capture the physics of a beam deflecting under a force bar. The kinematics in which the end of the beam slips under the force bar may be oversimplified, resulting in the closed-form solution's overpredictions. Stemming from this, a correction factor of 1.0085 was multiplied to $h$, giving $h$ = 166.4 mm and the force response plotted in red in Figure 2.10. This correction factor yields better agreement with the displacement and force peaks. The statistical

comparison between all four plots is presented in Tables 2.4 – 2.6. The maximum $F_x$ was determined from the mean of the first, four peaks while the max displacement and linear slope were determined from the first peak.

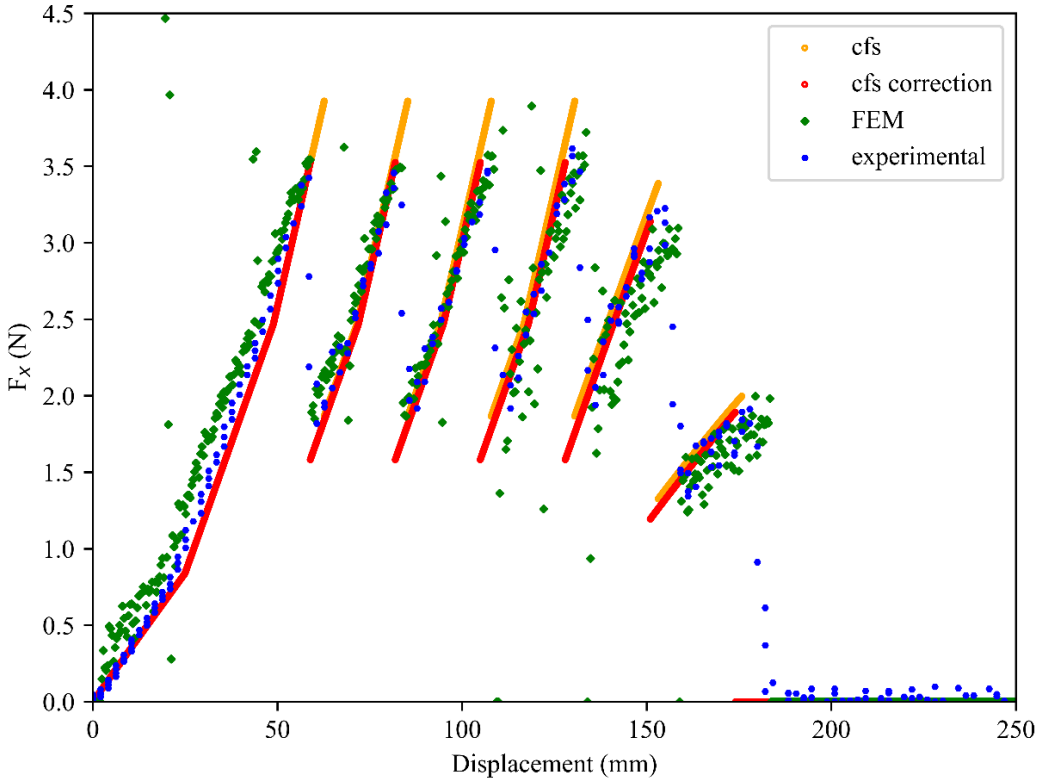


**Figure 2.10** Force-displacement comparison. $F_x$ plotted against $x$ displacement for six beams under identical conditions ($EI$ = 63000 N mm$^2$, $l$ = 180 mm, $h$ = 166 mm, $s$ = 24.9 mm) from a physical experiment (blue), FEM simulation (green), and closed-form solution prediction or cfs (orange). An additional closed-form solution prediction (red) was also plotted using the same $EI$, $l$, and $s$, but with a correction factor of 1.0085 multiplied to $h$, giving $h$ = 167.47151 mm.

**Table 2.4** Max $F_x$ comparison. Six beam system's max $F_x$ statistical comparison between the experimental results, FEM simulation, closed-form solution (cfs), and correction factor closed-form solution (cfs cor.). The max $F_x$ was determined from the mean of the first, four peaks.

| **Plot** | **Max $F_x$ (N)** | **Per. Diff. vs Exp. (%)** | **Per. Diff. vs FEM (%)** |
|---|---|---|---|
| exp. | 3.49 | 0.00% | 1.30% |
| FEM | 3.58 | 1.30% | 0.00% |
| cfs | 3.93 | 5.85% | 4.56% |
| cfs cor. | 3.53 | 0.47% | 0.83% |

**Table 2.5** Displacement comparison. Six-beam system's displacement at the first $F_{x\,peak}$ statistical comparison between the experimental results, FEM simulation, closed-form solution (cfs), and correction factor closed-form solution (cfs cor.). The beam's contact point with the force bar is estimated to be at 0 mm.

| Plot | Displacement at $F_{x\,peak}$ | Per. Diff. vs Exp. (%) | Per. Diff. vs FEM (%) |
|---|---|---|---|
| exp. | 58.53 | 0.00% | 0.06% |
| FEM | 58.46 | 0.06% | 0.00% |
| cfs | 62.64 | 3.39% | 3.46% |
| cfs cor. | 58.86 | 0.28% | 0.34% |

**Table 2.6** Linear slope comparison. Six-beam system's linear slope statistical comparison between the experimental results, FEM simulation, closed-form solution (cfs), and correction factor closed-form solution (cfs cor.). The linear slope was calculated from the contact point to the first $F_{x\,peak}$.

| Plot | Linear Slope (N/mm) | Per. Diff. vs Exp. (%) | Per. Diff. vs FEM (%) |
|---|---|---|---|
| exp. | 0.0596 | 0.00% | 1.36% |
| FEM | 0.0613 | 1.36% | 0.00% |
| cfs | 0.0627 | 2.46% | 1.10% |
| cfs cor. | 0.0599 | 0.19% | 1.17% |

### 2.5.3 FEM Data Triangulation

When compared to the *EI* values from the 100 multiple beam FEM simulations, the closed-form solution *EI* predictions from $F_{peak}$ yielded a mean percent error of 4.23% with a standard deviation of 5.16%. The percent error from each combination of spacing and maximum deflection is shown in Figure 2.11. Recall that the maximum deflection is directly related to the ratio of *h* to *l*. An additional contour plot with the "non-absolute" percent error color-coded is provided in Figure 2.12. This better highlights when the closed-form solution underpredicts or overpredicts.

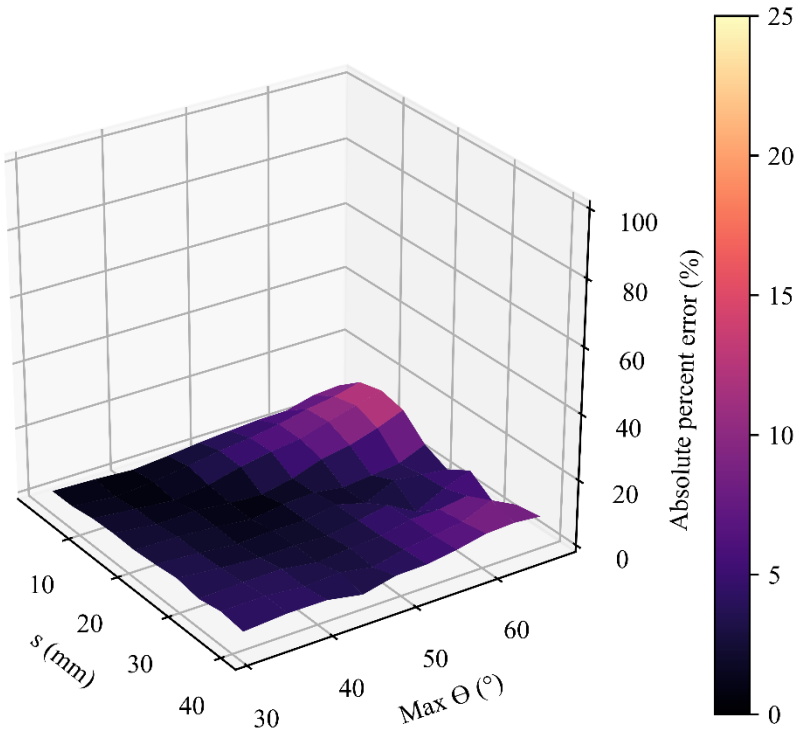


**Figure 2.11** 3D plot of the closed-form solution absolute percent error (%) versus spacing (mm) and maximum deflection (°) as a result of inputting $F_{peak}$ over 100 FEM simulations.

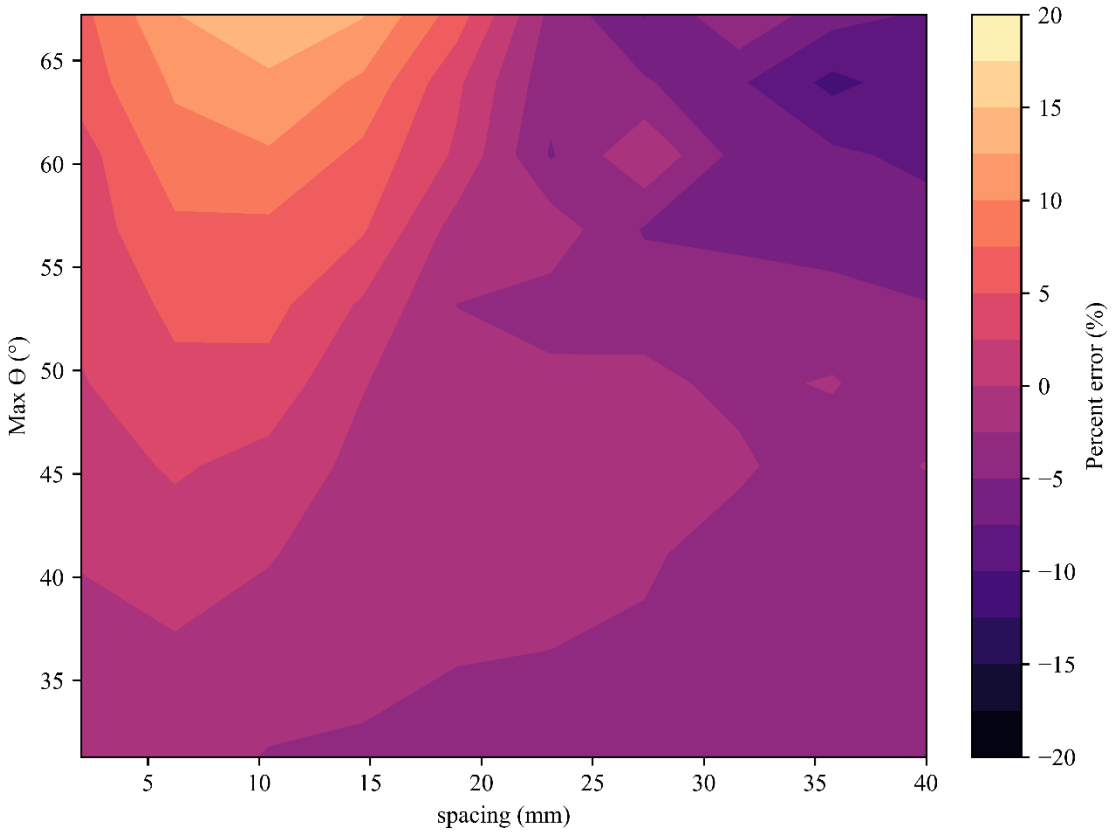


**Figure 2.12** Contour plot of the closed-form solution "non-absolute" percent error (%) versus spacing (mm) and max deflection (°) as a result of inputting $F_{peak}$ over the same 100 FEM simulations used in Figure 2.11.

Figure 2.12 suggests that the closed-form solution tends to yield increased error at greater deflections (i.e., lower force bar heights). More specifically, at larger deflections, the closed-form solution tends to overpredict *EI* when paired with smaller spacings, whereas underpredictions are observed when paired with larger spacings. At deflections less than 50°, the mean percent error is 2.41% (SD. = 1.67%). Note that the FEM force-displacement plots had increased noise for the larger deflections, particularly at $s$ = 2.0 mm and $s$ = 6.22 mm. This may have contributed to some error as $F_{peak}$ was obtained from those plots.

The closed-form solution *EI* predictions from $F_{x\,peak}$ provided similar results as shown in Figures 2.11 and 2.12, but with increased error. The mean percent error was 34.46% with a standard deviation of 59.99% using this method. The contour plot showing the "non-absolute" percent error across all spacing and deflection combinations is provided in Figure 2.13. At deflections greater than 50°, the closed-form solution accuracy begins to decrease for most spacings when inputting $F_{x\,peak}$, as shown in Figure 2.13. An explanation for this observation is provided in the Discussion.

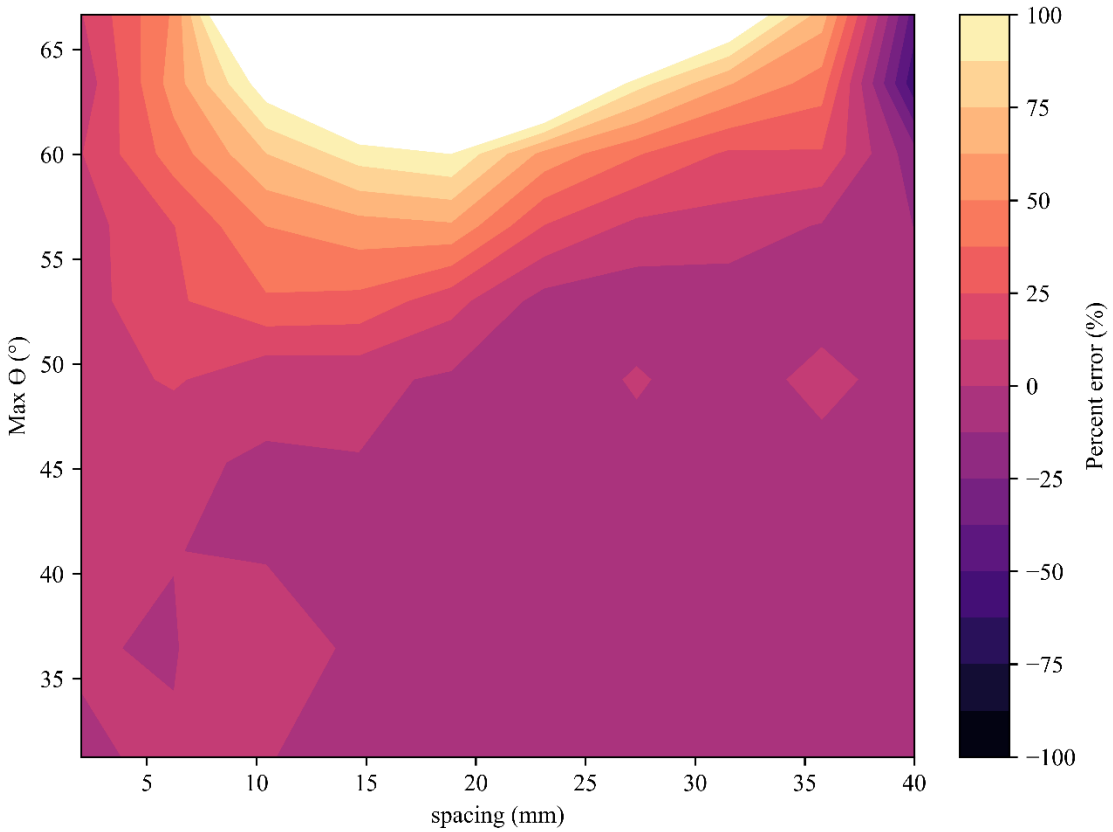


**Figure 2.13** Contour plot of the closed-form solution "non-absolute" percent error (%) versus spacing (mm) and maximum deflection (°) as a result of inputting $F_{x\,peak}$ over the same 100 FEM simulations.

Note that in Figure 2.13, the closed-form solution uses the PRBM single beam's end angle to correct for $\phi$. Without correcting $\phi$ from the PRBM beam end angle ($\theta_o$), underpredictions in $F_{peak}$ and *EI* are typically observed, giving a mean percent error in *EI* of 18.24% with a standard deviation of 14.66%. However, at deflections less than 50°, this method provides a mean percent error in *EI* of 12.11% (SD. = 4.48%), whereas, correcting for $\phi$ provides a mean percent error of 2.99% (SD. = 3.50%).

## 2.6 Discussion

The following discussion presents experimental uncertainty, $F_{x\,peak}$ error analysis, a closed-form solution sensitivity analysis, an examination of the effect of interactions, limitations, applications, and future work.

### 2.6.1 Experimental Uncertainty

Any physical experiment contains sources of error and uncertainty. The physical experiments conducted as part of this thesis are no exception. Potential sources of experimental uncertainty in this

study include friction and measurement errors. For example, all beams were assumed to be perfectly smooth, prismatic, and identical. In addition, the force bar height $h$ was assumed to be perfectly constant during the experiment. These factors were closely controlled and monitored but small sources of error likely still existed in the experiment. One advantage of FEMs is that experimental uncertainties involving geometric measurement tolerances can be eliminated. Furthermore, FEMs enable all input parameters to be carefully controlled and varied to produce extensive data sets that would not be economically feasible via physical experimentation. However, FEMs are subject to some noise even with a high sampling rate or small step size. Fortunately, it is typically easy to identify and disregard noisy data points that occur due to dynamic effects. For these reasons, both physical experiments and FEMs were used to validate the closed-form solution.

### 2.6.2 $F_{x\,peak}$ Error Analysis

When inputting $F_{x\,peak}$, the closed-form solution's accuracy at deflections greater than 50° was significantly decreased, as previously shown in Figure 2.13. Fundamental assumptions that the closed-form solution is built upon become less valid in these circumstances. Recall that point loads are used throughout the closed-form solution; yet, as the deflections increase, the contact surface between beams increases. Additionally, the closed-form solution uses the PRBM single beam's end angle $\theta_o$ to correct for $\phi$, but this is likely to underpredict $\phi$ with multiple beams interacting and influencing $\theta_o$. As a result, an erroneous lower value of $\phi$ causes a large overprediction in $F_{peak}$ when converted from $F_{x\,peak}$ ($F = F_x/\sin(\phi)$). Without correcting $\phi$, underpredictions in $F_{peak}$ conversions occur, providing less error at larger deflections but increased error at smaller deflections. Neither $\phi$ method is comprehensive for multiple beams.

While there is approximately the same amount of noise in the FEM $F_x$ plots as the $F$ plots, this closed-form solution $F_{x\,peak}$ method amplifies error during the determination of $F_{peak}$. Error amplification also increases as deflection increases when inputting $F_{x\,peak}$ as $\phi$ is directly related to $\Theta$. To illustrate this, consider $F_{peak}$ values being converted from $F_{x\,peak}$ over several deflections while holding the inputted $F_{x\,peak}$ constant. Figure 2.14 displays the resulting relative $F_{peak}$ (in relation to its own maximum value) as a function of $\Theta$. Notice that at greater deflections, the slope significantly increases. Therefore, erroneous measurements of $F_{x\,peak}$ at larger deflections have a greater impact on the converted $F_{peak}$ and $EI$ predictions. In the FEM experiment, error and variation in the converted $F_{peak}$ and $EI$ prediction did increase with deflection following a similar curve to that shown in Figure 2.14. This is shown in Figures 2.15 and 2.16.

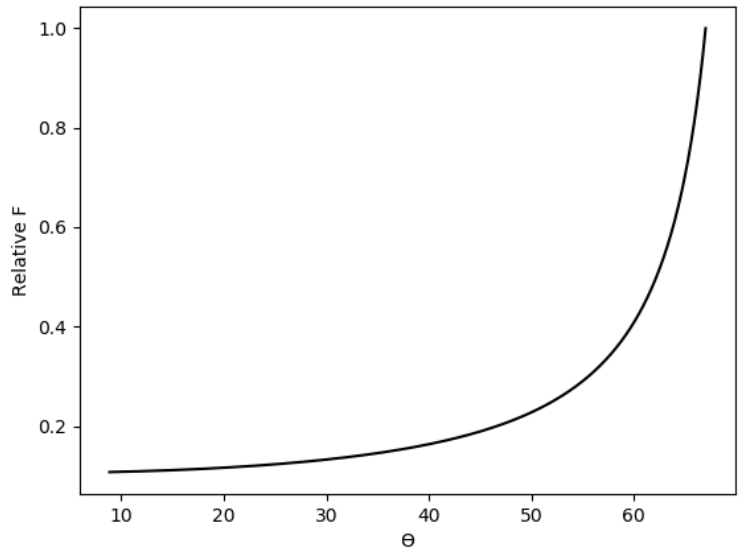


**Figure 2.14** Relative converted $F_{peak}$ ($F_{peak}/max(F_{peak})$) as a function of maximum deflection ($\Theta$). The inputted $F_{x\,peak}$ was held constant.

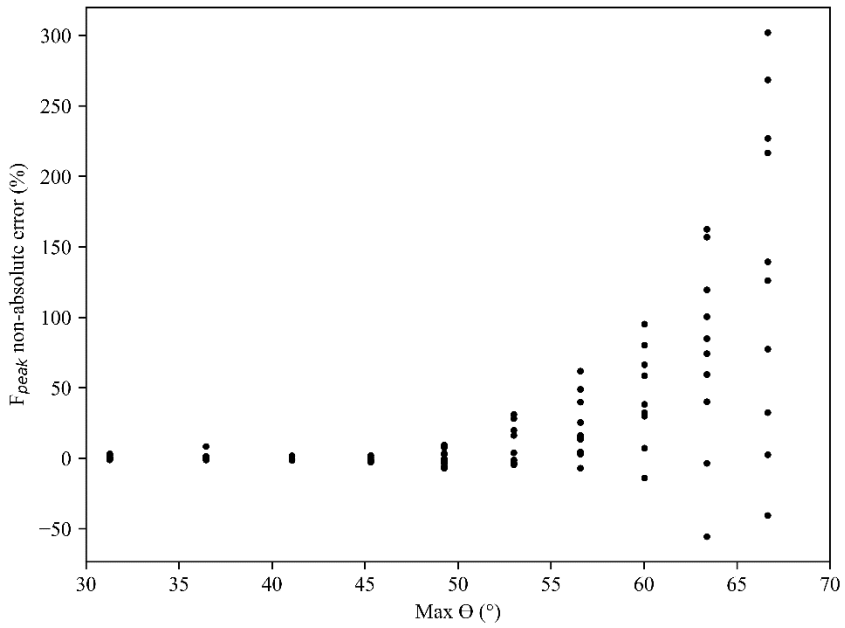


**Figure 2.15** Non-absolute percent error in the closed-form solution's converted $F_{peak}$ from $F_{x\,peak}$ (compared to the observed $F_{peak}$ from the FEM force-displacement plots) as a function of maximum deflection.

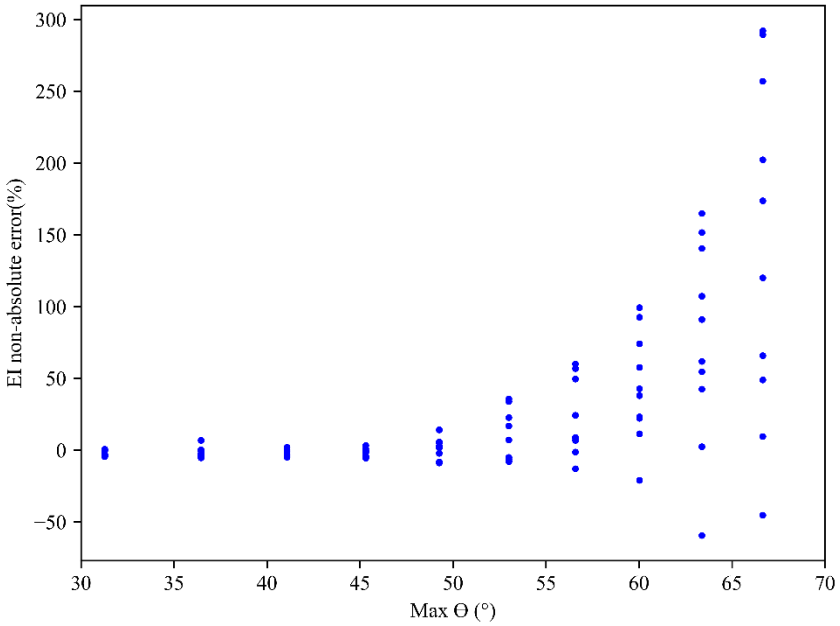


**Figure 2.16** Non-absolute percent error in the closed-form solution *EI* prediction with $F_{peak}$ from Figure 2.15 inputted as a function of maximum deflection.

### 2.6.3 Closed-Form Solution Sensitivity Analysis

A sensitivity analysis of the closed-form solution was conducted to highlight its most effective use. Using a Python script, the closed-form solution was utilized to predict *EI* for all combinations of *h* from 0.5*l* to 0.99*l* and *s* from 0.005*l* to 0.99*l* while holding the inputted *l* and $F_{\text{peak}}$ constant. As expected, *EI* increases as both *h* and *s* increase. The relative *EI* with respect to its own maximum across all combinations ($EI/EI_{max}$) is shown in Figure 2.17.

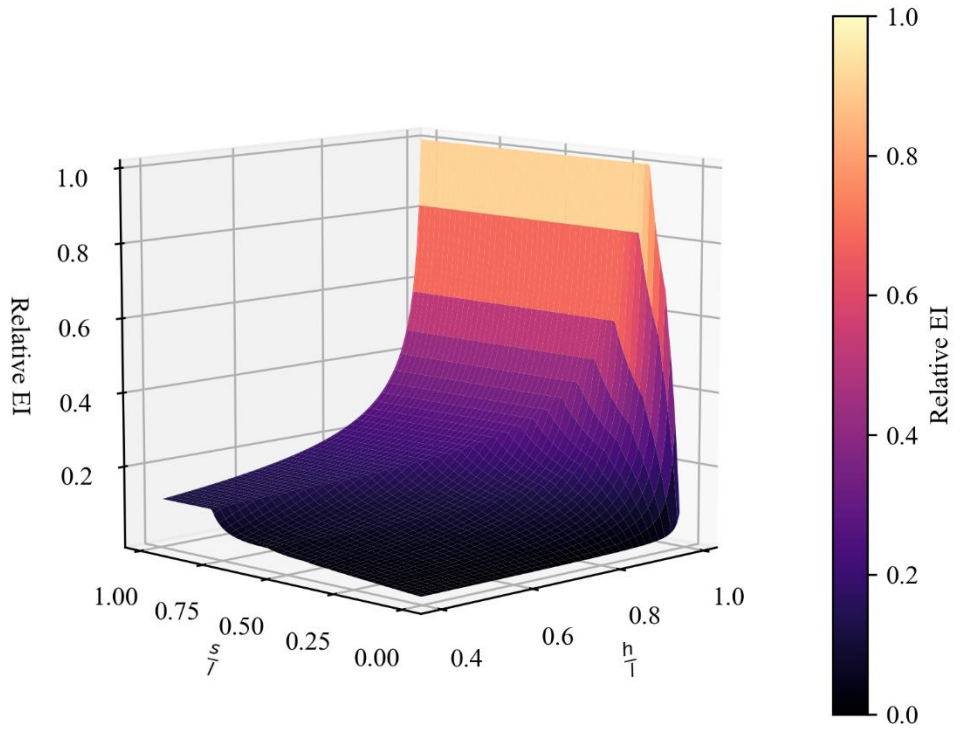


**Figure 2.17** Relative *EI* ($EI/EI_{max}$) across combinations of *s* and *h* (normalized with respect to *l*) with $F_{peak}$ held constant. The surface plateaus at dimensions where no interactions between beams occur.

The numerical derivative of this relative *EI* was then assessed, first with respect to *h/l* and then *s/l*, as shown in the contour plots respectively in Figures 2.18 and 2.19.

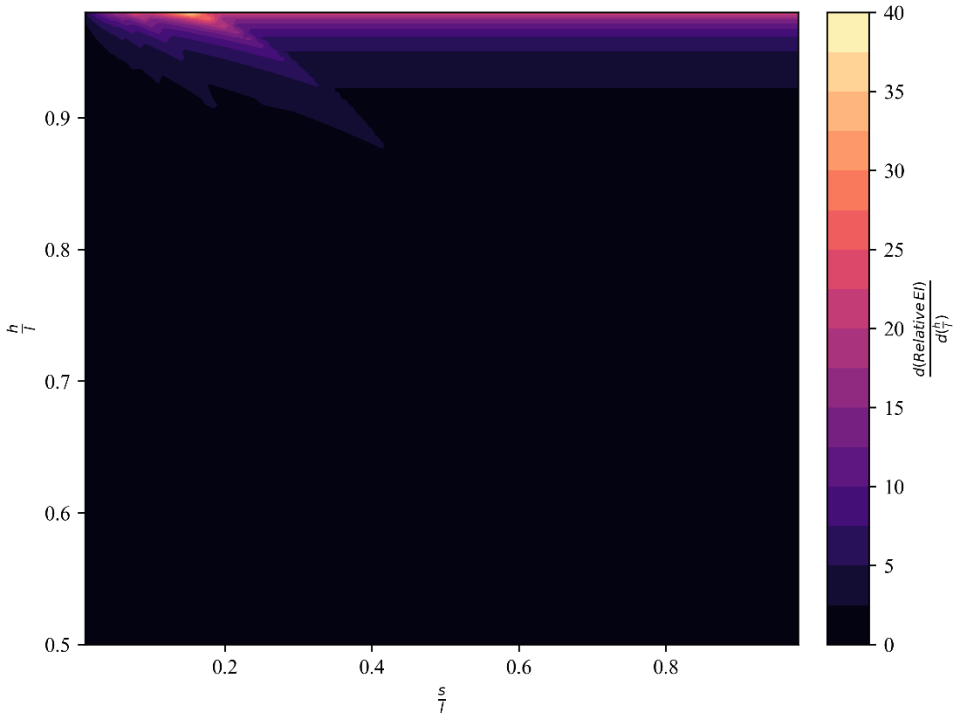


**Figure 2.18** Contour plot showing the numerical derivative of the relative *EI* with respect to *h/l* for combinations of *h/l* and *s/l*.

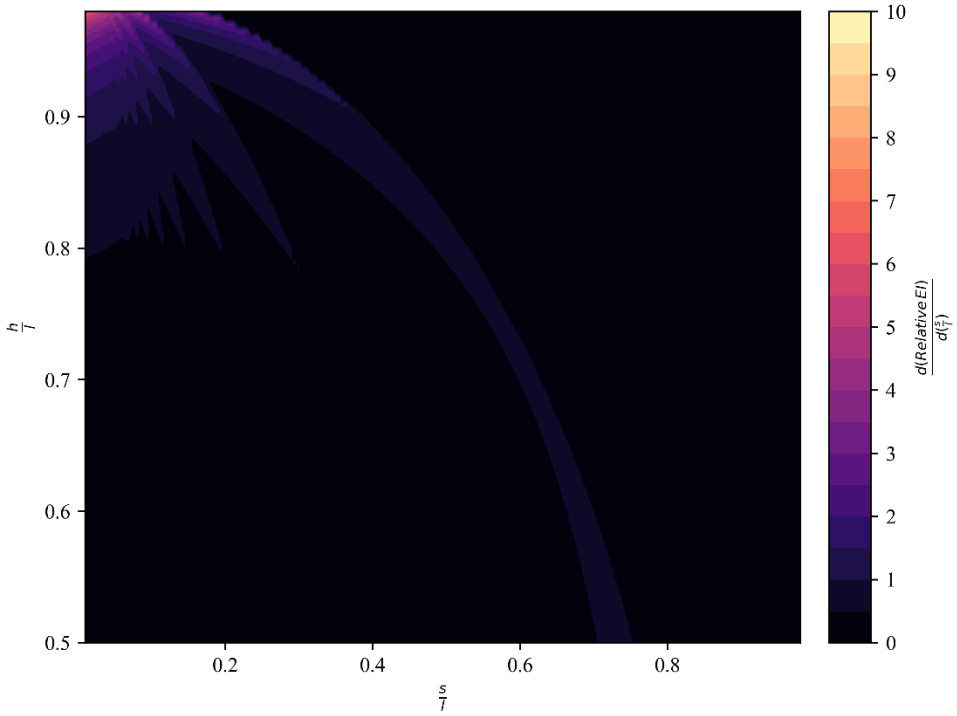


**Figure 2.19** Contour plot showing the numerical derivative of the relative *EI* with respect to *s/l* for combinations of *s/l* and *h/l*. Note the difference in colormap scales compared to Figure 2.18.

Notice in Figure 2.18 that the derivative of the relative *EI* is small for all spacings unless *h/l* is greater than about 0.9. Thus, from a theoretical perspective, at higher *h/l* ratios, errors in *h* and *l* measurements can result in greater error in *EI* predictions, than if lower *h/l* ratios were used. On the other hand, FEM experimental results showed greater error with greater deflections (low *h/l* ratios). Recall that the closed-form solution was generally accurate in the FEM experiment with deflections less than 50°, which corresponds to a *h/l* ratio of approximately 0.7. The most effective range of *h/l* with minimal sensitivity to errors is then 0.7 - 0.9.

Figure 2.19 again shows sensitivity at high *h/l* ratios, particularly at smaller *s/l* ratios. Note that the lighter purple curve running through the middle of the plot is likely due to interactions between beams no longer occurring. By comparing Figures 2.18 and 2.19, taking note of the difference in scales, it seems that the closed-form solution is less sensitive overall to changes in *s/l* than to changes in *h/l*.

The effect of $F_{peak}$ is linear as indicated by Eq. (41) and Eq. (18), unless $F_{x\,peak}$ is inputted as previously discussed.

### 2.6.4 Effect of Interactions

To explore the effect of interactions in multiple beam systems and the closed-form solution, an additional PRBM model was developed in which interactions were eliminated by assuming no contact for any spacing or deflection. In essence, its closed-form solution assesses the location of each beam's load at the frontmost beam's maximum deflection (i.e., immediately prior to passing under the force bar). Summing each beam's force response then allows for predictions of $F_{peak}$ or *EI*. This model is referred to as the Non-Interacting Model. The Multiple Inline Interacting Cantilever Beam Model will be referred to here as the Interacting Model.

The Interacting and Non-Interacting Model were then utilized to predict *EI* values for all combinations of *h* from 0.5*l* to 0.99*l* and *s* from 0.005*l* to 0.99*l*. $F_{\text{peak}}$ was held constant for all cases. The percent differences between the two model's *EI* predictions were then computed. Figure 2.20 displays the results with a contour plot, in which negative percent differences correspond to the Interacting Model calculating a lower *EI* than the Non-Interacting Model.

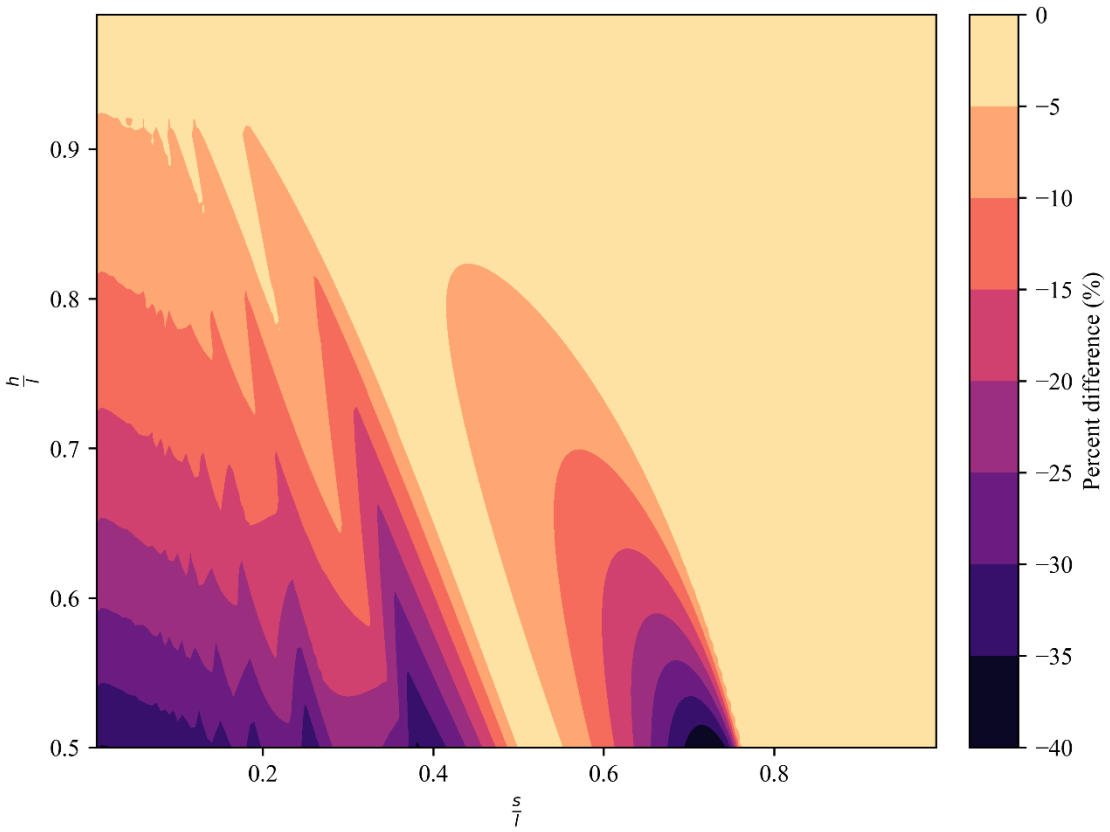


**Figure 2.20** *EI* percent difference between the Interacting Model and Non-Interacting Model for various combinations of *s* and *h* (normalized with respect to *l*). Negative percent differences indicate the Interacting Model predicted a lower *EI* value than the Non-Interacting Model.

For all combinations of *h*/*l* and s/*l*, the Interacting Model produces lower *EI* predictions than the Non-Interacting Model. Generally, the difference is small (less than 5%), but increases as *h*/*l* and *s* decrease. At the non-extremes of system dimensions, the effect of interactions is minimal. In those cases, the simpler Non-Interacting Model is applicable. At lower *h*/*l* and *s* values, more interaction occurs, which has a greater effect on $F_{peak}$ and predictions of *EI*. Therefore, the Interacting Model is likely to be more accurate in these situations. Reconsider Figure 2.12 in which the Interacting Model tended to overpredict FEM *EI* values for small *h* and *s* values. Without accounting for the interactions, Figure 2.20 suggests the overpredictions and error would be greater. Although, at large *h* and small *s* values, neglecting the interactions may have potentially decreased error.

More interestingly, both the Interacting Model and Non-Interacting Model can simultaneously be assessed for systems with unknown or varying levels of interactions. This refers to systems in which beams are not always inline with each other. The true *EI* or $F_{peak}$ is likely to be somewhere between the Interacting and Non-Interacting predictions.

### 2.6.5 Limitations

The Multiple Interacting Cantilever Beam Model was developed from the perspective of a controlled, ideal scenario, which places limitations on its effectiveness. Recall that the model assessed the scenario with constant spacing and assumed all beams had identical lengths and flexural stiffnesses. The beams were also assumed to be fully fixed to the ground and directly inline. In many cases, especially natural systems, these assumptions will not hold. The complexity in nature will violate other significant assumptions within the closed-form solution as well. Consider agricultural crop systems. The closed-form solution does not account for loading due to the crop head/fruit (if pre-harvest), leaves interacting, and loose soil. Such factors affect the system's mechanics which the closed-form solution currently cannot account for. Furthermore, the model utilizes a static perspective to analyze a dynamic process. At higher speeds, the reliability of the model may decrease with greater inertial forces involved [15].

The model hereby presented only examined cases in which the beams possessed rectangular-faced geometry that guaranteed interaction between beams. With different beam geometry, the deflection and interaction behavior are likely to be altered. With hollow cylinders (e.g. many types of crops), some torsional deflection, out of plane bending, and sliding may be involved. This has been observed in preliminary exploration of hollow cylinders, which tend to spread apart upon large deflections.

The model and experiments only considered cases in which the force bar was parallel to the face of the beams. Other force bar orientations were not explored and are likely to result in different mechanics and force responses.

### 2.6.6 Applications

While a more accurate and complete model can be developed, the relative simplicity is a key strength of the model that allows for easy adoption in various applications. Just four input parameters ($s$, $l$, $h$, $F_{peak}$ or $EI$) allow for relatively accurate predictions. Thus, the model can be implemented into high throughput applications for estimating $EI$ or initial design purposes.

In terms of measuring $EI$, the model is most likely to be applied to natural systems. Many models of natural systems exist but are often too complex to be implemented in applications or field devices. Some require numerous input parameters [16], don't account for interactions [17], and/or require elliptical integration or numerical methods [17]. The simple model presented here may overlook complex factors involved in nature, but it can be used as an efficient first estimation, especially in many natural systems with limited variation in geometry (spacing and length). Note that in most systems, like agricultural crops, multiple rows are involved rather than a single row as the

presented model illustrates. Under the simplifying assumption that the dimensions remain consistent between rows, the model can still be applied for when multiple rows contact the force bar. To do so, the measured force must be divided by the number of rows acting upon the force bar. An average *s* and *l* should also be determined for inputs. The ability to evaluate multiple rows at once is highly advantageous. It allows for a large sample size and produces a more detectable force response.

The model can also aid in the initial design process of similar synthetic structures, such as brushes, brooms, or even nanotube arrays. Specifically, the model can provide accurate predictions and highlight the effect of design choices. In many cases, designers may be interested in the system's maximum force response, which the model can predict for any combination of *s, l, h, EI*, or even the number of beams in a row. For example, given *EI*, *l*, and the number of beams (10 in this case), Figure 2.21 can be generated.

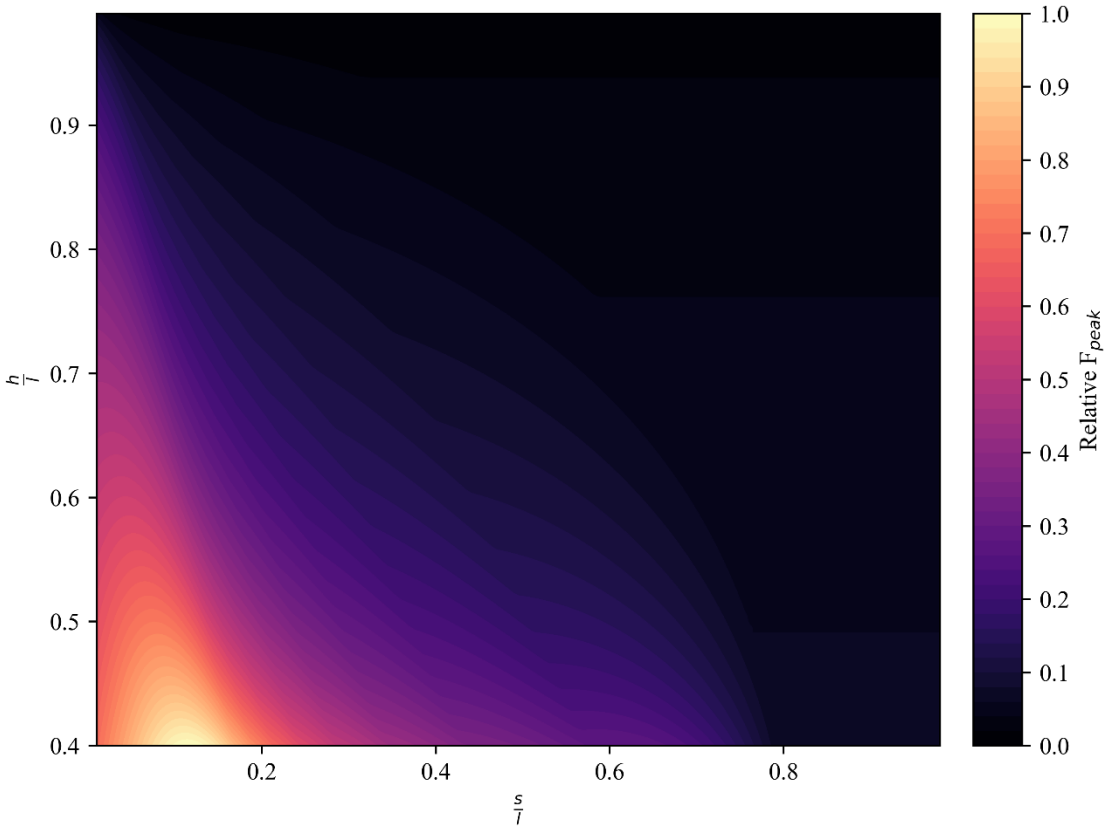


**Figure 2.21** Relative maximum force ($F_{peak}$) of 10 beams for all combinations of *s* and *h*. *EI* and *l* held constant.

2.6.7 Future Work

While the Multiple Interacting Cantilever Beam Model has been shown to be a good predictor of *EI* or the force response, the model could be improved from a few approaches. A beam end angle correction factor for multiple beams interacting based on $\Theta$ and *s/l* could be experimentally developed. This would likely reduce error, particularly at deflections greater than 50°. The contact surfaces could also be explored over combinations of *h/l* and *s/l* to better place point loads. While the simplicity of the model is one of the strongest benefits, incorporating multiple pin joints and torsional springs into the PRBM is likely to improve accuracy. This has been shown to increase accuracy for single cantilever beams [18]. The contact surfaces may consequently be modeled more realistically with such additions. It is also possible to incorporate each beam's specific *K*, rather than assuming all are equivalent. However, this would increase the complexity and is not expected to increase accuracy significantly since $K_\Theta$ and $\gamma$ both don't vary much over a vast range of $\phi$. As alluded to in 2.6.5 Limitations, different beam geometry should also be examined as adaptations to the model may be required.

**2.7 Conclusion**

A novel model of the deflection of multiple, inline, interacting cantilever beams using the pseudo-rigid body model has been described with its accompanying closed-form solution. Just four input parameters *(l, h, s,* $F_{peak}$ or *EI*) are required to determine the force-displacement response or the average *EI*. The closed-form solution was shown to provide accurate predictions when compared to physical and computational experiments, validating the model. The model is most accurate with deflections less than 50°, but sensitive to errors in input parameters for deflections less 28°. Error is likely reduced when inputting $F_{peak}$ directly from the total force rather than the horizontal component.

With its simplicity, the model can easily be applied to better understand many natural and synthetic systems (agricultural crops, hair, brushes, etc.) by accounting for nonlinearities and interactions. Interactions were shown to have significant effect, especially at large deflections and small spacings. Adjustments to the model may be required to better model specific systems. Future work should be conducted to improve the accuracy and effective range of the model.

## 2.8 Nomenclature

**Table 2.7** Nomenclature

| Term | Definition |
|---|---|
| $(\alpha^2)_t$ | nondimensionalized transverse load index |
| $\beta$ | $\beta = 90° - \Theta$ |
| cfs | closed-form solution |
| $c_o$ | parametric angle coefficient |
| $d_i$ | horizontal distance the $i^{th}$ beam extends past the next $(i + 1)$ beam |
| $E$ | Young's modulus (modulus of elasticity) |
| $EI$ | flexural stiffness |
| $F$ | applied force acting on cantilever beam |
| FEM | Finite Element Model |
| force bar | rigid body, see Figure 2.1 |
| $F_{peak}$ | total force response before sliding past the force bar |
| $F_{x\,peak}$ | force response in horizontal direction of $F_{peak}$ |
| $\gamma$ | characteristic radius factor |
| $h$ | effective height of force bar |
| $I$ | cross-sectional moment of inertia |
| $K$ | torsional spring constant |
| $K_\theta$ | nondimensionalized torsional spring constant |
| $l$ | effective length of beams |
| $m$ | number of maximum force peaks |
| $nP$ | vertical component of $F$ |
| $P$ | horizontal component of $F$ |
| $\phi$ | angle of $F$ with respect to undeflected axis |
| PRBM | pseudo-rigid body model |
| $s$ | beam to beam spacing |
| $SD$ | standard deviation |
| $T$ | torque |
| $t$ | total number of beams in system |
| $\Theta$ | PRBM angle of deflection |
| $\theta_o$ | beam end angle |
| $u$ | maximum number of beams in contact at frontmost beam's maximum deflection |

**2.9 References**


[1] Barten, H. J. 1944. “On the Deflection of a Cantilever Beam.” *Quarterly of Applied Mathematics* 2 (2): 168–71. https://doi.org/10.1090/qam/10879.

[2] Barten, H. J. 1945. “Corrections to My Paper on the Deflection of a Cantilever Beam.” Quarterly of Applied Mathematics 3 (3): 275–76. https://doi.org/10.1090/qam/13361.

[3] Bisshopp, K. E., and D. C. Drucker. 1945. “Large Deflection of Cantilever Beams.” Quarterly of Applied Mathematics 3 (3): 272–75. https://doi.org/10.1090/qam/13360.

[4] Frisch-Fay, R. 1961. “A New Approach to the Analysis of the Deflection of Thin Cantilevers.” Journal of Applied Mechanics 28 (1): 87–90. https://doi.org/10.1115/1.3640472.

[5] Navaee, S., and R. E. Elling. 1992. “Equilibrium Configurations of Cantilever Beams Subjected to Inclined End Loads.” Journal of Applied Mechanics 59 (3): 572–79. https://doi.org/10.1115/1.2893762.

[6] Wang, T.M. 1968. “Nonlinear Bending of Beams with Concentrated Loads.” Journal of the Franklin Institute 285 (5): 386–90. https://doi.org/10.1016/0016-0032(68)90486-9.

[7] Howell, Larry L. 2001. *Compliant Mechanisms*. New York: John Wiley & Sons.

[8] Howell, L. L., A. Midha, and T. W. Norton. 1996. “Evaluation of Equivalent Spring Stiffness for Use in a Pseudo-Rigid-Body Model of Large-Deflection Compliant Mechanisms.” Journal of Mechanical Design 118 (1): 126–31. https://doi.org/10.1115/1.2826843.

[9] Thornton, Stephen T., and Jerry B. Marion. 2004. *Classical Dynamics of Particles and Systems.* 5th ed. Belmont, CA: Brooks/Cole.

[10] Matthews, Frank L., G. A. O. Davies, D. Hitchings, and C. Soutis. 2000. *Finite Element Modelling of Composite Materials and Structures*. Elsevier.

[11] Hibbitt, Karlsson, B. I. Karlsson, and E. P. Sorenson. 2016. “ABAQUS/Standard Theory Manual.” *Sorenson Inc*.

[12] Simulia, D. S. 2016. “ABAQUS Analysis Manual.” *Providence, RI*.

[13] Lawlor, Debbie A., Kate Tilling, and George Davey Smith. 2016. “Triangulation in Aetiological Epidemiology.” *International Journal of Epidemiology* 45 (6): 1866–86. https://doi.org/10.1093/ije/dyw314.

[14] Nelson, Nathanael, Christopher J. Stubbs, Ryan Larson, and Douglas D. Cook. 2019. “Measurement Accuracy and Uncertainty in Plant Biomechanics.” *Journal of Experimental Botany* 70 (14): 3649–58.

[15] Li, Na, Hai-Jun Su, and Xian-Peng Zhang. 2017. “Accuracy Assessment of Pseudo-Rigid-Body Model for Dynamic Analysis of Compliant Mechanisms.” *Journal of Mechanisms and Robotics* 9 (5): 054503. https://doi.org/10.1115/1.4037186.

[16] Baker, C.J., M. Sterling, and P. Berry. 2014. “A Generalised Model of Crop Lodging.” *Journal of Theoretical Biology* 363 (December): 1–12. https://doi.org/10.1016/j.jtbi.2014.07.032.

[17] Huang, Mingsen, Yaoming Li, Anya Chen, and Lizhang Xu. 2019. “Numerical Calculation Method of Deflection Deformation of Rice Stalk.” *Applied Sciences* 9 (15): 3125. https://doi.org/10.3390/app9153125.

[18] Su, Hai-Jun. 2009. “A Pseudorigid-Body 3R Model for Determining Large Deflection of Cantilever Beams Subject to Tip Loads.” *Journal of Mechanisms and Robotics* 1 (2): 021008. https://doi.org/10.1115/1.3046148

# Chapter 3: SOCEM: A High Throughput Field Device for Assessing Stalk Lodging Resistance in Grains

## 3.1 Abstract

The breaking of crop stems before harvest, known as stalk lodging, has a significant, negative impact on farmers and plant breeders. To reduce lodging, proper phenotyping of stalk strength is required. Existing methods are unreliable or have limited throughput. A new device titled SOCEM (Stiffness of Crops Extrapolation Machine) for phenotyping stalk strength is presented here with details of its design and testing method. It replicates natural loading and has higher-throughput estimations of stalk strength than any previously developed devices. Entire experimental plots, despite featuring numerous, interacting stems, can be tested at once within a few minutes. Validation tests indicate it can accurately evaluate flexural stiffness, which is highly correlated to stalk bending strength. Preliminary data suggests it can distinguish between varieties that are prone to lodging and varieties with high lodging resistance. In its current state, it is designed for small grains, but it will be adapted for large grains in the future.

## 3.2 Introduction

The mechanical failure of cereal crops, known as lodging, can have a significant negative impact on crop yield and grain quality [1]. For example, in the UK, lodging associated yield losses in wheat are estimated at $64 million per annum on average [2]. However, severe wheat lodging typically occurs every 3-4 years in the UK which affects 15-20% of the planted area [3] and can cause financial losses closer to $218 million [2]. Similar trends are common in other vital grain crops. For example, lodging in maize is estimated to cause $3.8 billion dollars in US yield losses per annum [4].

Lodging can be divided into two types, stalk lodging and root lodging. Stalk lodging occurs when the stem breaks (typically near the lower internodes for small grains [5-7], whereas root lodging refers to the failure of the root anchorage system. Both types of lodging are prevalent in modern agriculture. While they are separate mechanisms, root and stem lodging may enhance each other. For example, it is possible for root lodging to induce an initial displacement of the stalk from the vertical that then increases the applied bending moment on the stalk due to self-weight. This, in turn, increases the chance of stalk lodging [8]. Once stalk lodging occurs in a plant, it cannot recover [9].

One of the most commonly employed techniques to quantify lodging resistance of various crop varieties is to simply count the number of lodged plants at harvest [10]. Unfortunately, lodging counts are highly confounded by numerous uncontrolled environmental factors. Such factors include wind, rain, disease, soil type, topography, previous crop, and husbandry [8]. The amount of lodging is

also temporally dependent [8]. Some years no lodging will occur, while other years, entire fields lodge regardless of crop strength [11]. Furthermore, lodging counts frequently do not specify the type of lodging [10] which limits understanding of possible differences in failure patterns among varieties. Finally, lodging counts are binary (lodged or not lodged) whereas lodging resistance (i.e. stalk and root anchorage strength) exists on a continuous spectrum of values. The binary nature of lodging counts limits statistical approaches used to discover the genetic underpinnings of lodging resistance.

Lodging resistant crops must be strong enough to withstand internal and external forces (e.g. wind, rain, hail, self-weight) [12]. Breeding for increased stalk strength is therefore a viable path to decrease lodging related losses. Several tools have been developed to assess the root and stalk strength of grain crops in the field. In addition, several laboratory-based methods of measuring strength are available to researchers (e.g., three-point bending, rind penetration resistance, tensile and crushing tests [13]. Unfortunately, lab tests are typically time-intensive, destructive, and require transporting samples offsite which results in increased cost. Many labs have found lab-based testing procedures to be prohibitively expensive to employ in genetic and plant breeding studies aimed at improving lodging resistance due to the large sample sizes required in such studies. In general, field-based tools for measuring stalk strength and lodging resistance are more economically and logistically feasible to employ in plant breeding and genetic studies of field crops.

Several devices have been constructed that are designed to perform bending tests on grain crops in the field. For instance, several researchers have developed devices for testing large grain crops (e.g., corn, sorghum) [14-16]. These devices all utilize a similar method of applying external loads to the plant of interest that induce bending in the plant's stalk or stem. The force-displacement data recorded by the device is then used in various ways to predict lodging risk. When working with small grain crops (i.e., wheat, barley, canola, etc.) the stem of a single plant typically does not provide enough resistance for reliable force measurements in a field setting. Therefore, multiple plant stems are typically subjected to a bending force during a test. For example, two hand-held devices [10, 17], have been developed to measure the force required to push a row of crops to a discrete angle. Unfortunately, it is unclear how to properly account for the number of stems being engaged in such tests as the number of stems may vary from one test to the next. Furthermore, the stems can interact with one another during the test which may also affect test results. A complete review of field-based tools for assessing stalk and root lodging resistance in grain crops can be found in [9].

This chapter describes a new, portable, field-based device, known as SOCEM (Stiffness of Crops Extrapolation Machine) that enables higher-throughput estimations of stalk strength than any previously developed device. The SOCEM is easily operable, simulates natural stem loading patterns, and can collect lodging resistance data from an experimental plot of wheat within a few minutes.

Despite testing numerous stems at once, its novel design and method accounts for nonlinearities and interactions within the complex, mechanobiological crop system. Furthermore, the SOCEM can be used post-harvest to prevent damage to yield-bearing crops. The SOCEM was originally developed for testing small grains, however, it can be scaled up and applied to test large grain crops as well.

## 3.3 Device Description

The SOCEM device is composed of four subsystems: frame, graphical user interface (GUI), electronics for data acquisition, and sensors for measuring force and device displacement. Details of each subsystem are provided here. The primary function of the SOCEM is to displace stems and record force and position data as it is pushed through a harvested plot of stems (i.e., stubble). The force-position data is paired with measurements of the average crop height and the average spacing between stems (obtained from planting density measurements). From the analysis, estimations of the average flexural stiffness of the plot are calculated as an evaluation of stalk lodging resistance.

### 3.3.1 Frame

The aluminum frame, as depicted in Figure 3.1, consists of a chassis, handlebar connected to the vertical arm, and three 24-inch bike wheels. The position of the handlebar can easily be adjusted by loosening an 80/20 “L” handle linear bearing brake. The large-diameter wheels and tires provide smooth rollover on uneven surfaces. Attachments, such as sensors and cases, are mounted to the frame with bolts on the 80/20 ready tube or 80/20 T-slot extrusions. Additional attachments are easily mountable. Figure 3.3 displays the SOCEM with primary and secondary attachments. The force bar, which attaches to the force sensor, is a 76 cm long, carbon fiber rectangular rod that is lightweight to reduce noise in force measurements due to weight loading vibrations. Since crops vary in height, the height of the force bar can be adjusted via two, 80/20 linear bearing sliders. A custom ruler and pointer indicate the force bar height from the ground. The indicated force bar height is a user input for the GUI.

For ease of transportation and storage, the frame is able to be collapsed and folded, as shown in Figure 3.2. To do so, the handlebar is rotated forward fully, and a wing nut and bolt are removed, allowing the rear to swivel inward. The two front wheels can also easily be removed by sliding them out of the 80/20 ready tube after removing their wing nut and bolt. Even without removing the front wheels, in the folded form, the SOCEM can fit in a truck or hatch-back vehicle. The weight of the full device is less than 200 N, allowing most individuals to lift it if needed.

**Figure 3.1** CAD model of the SOCEM frame.

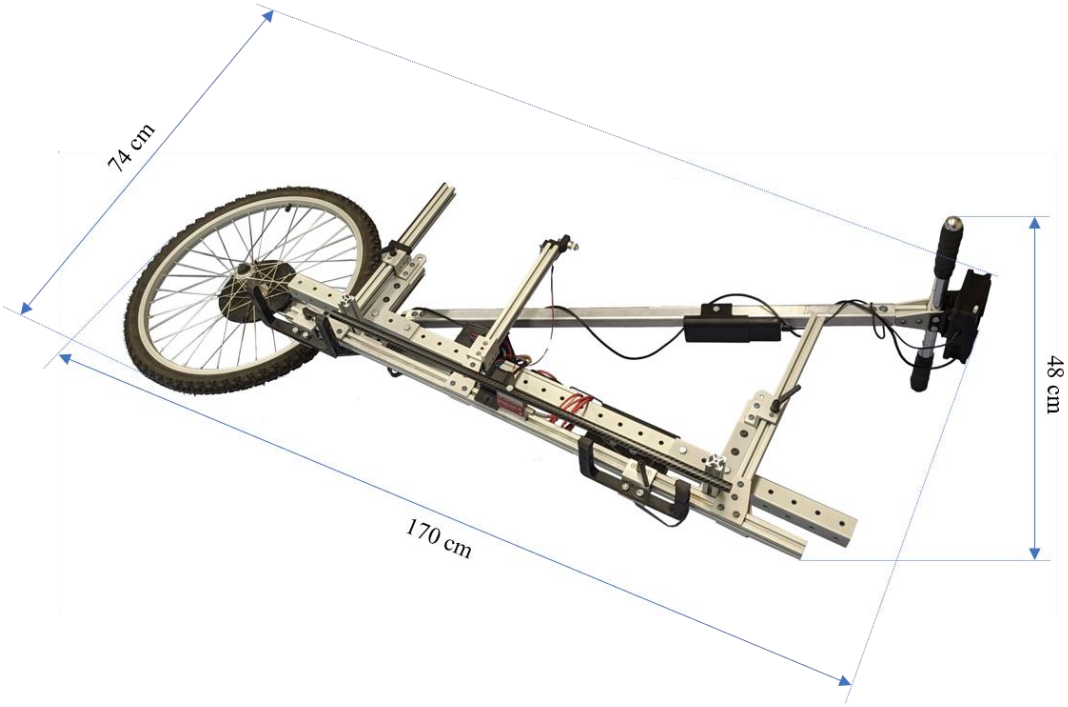


**Figure 3.2** The SOCEM in its collapsed and folded configuration for transportation. Maximum volumetric dimensions illustrated.

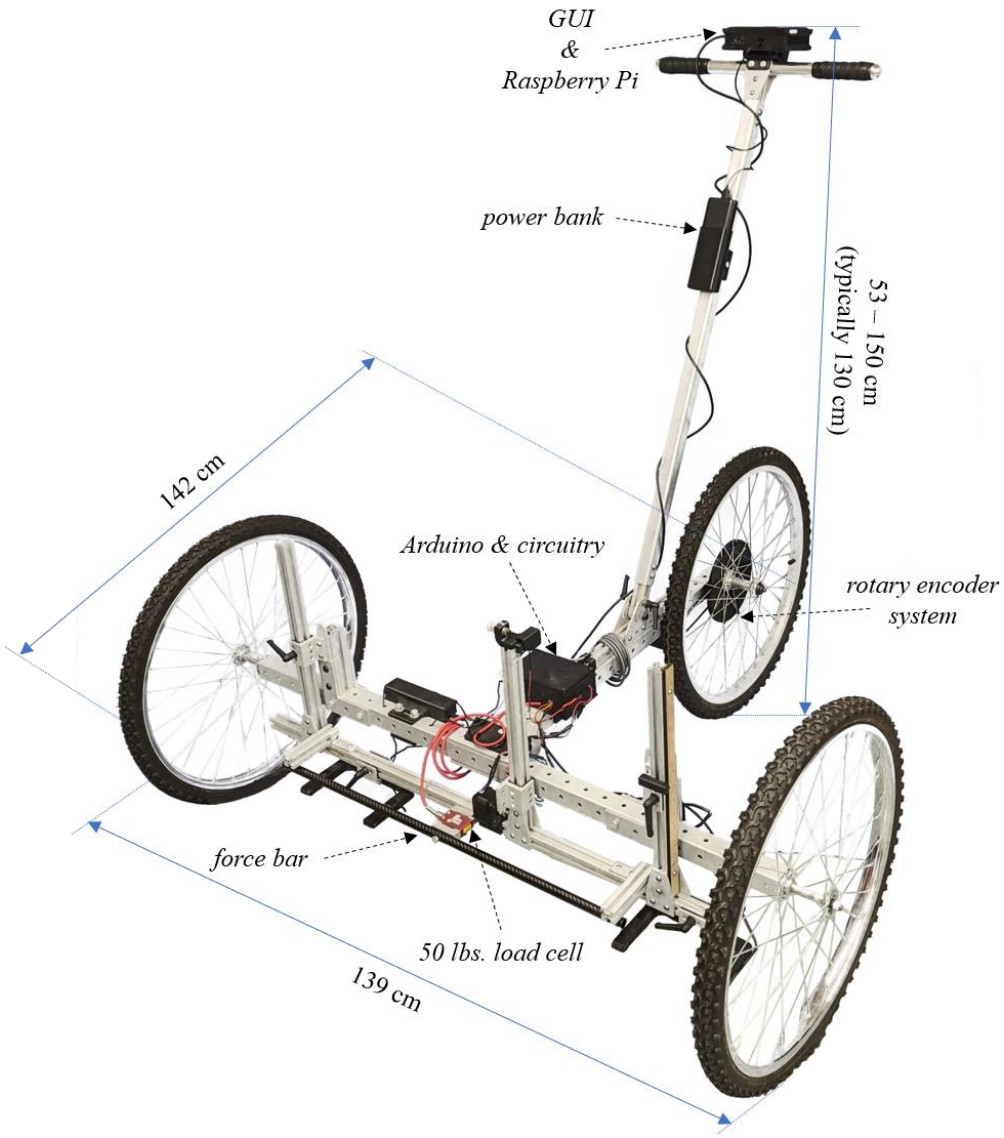


**Figure 3.3** The SOCEM with major components and maximum volumetric dimensions labeled. Note that additional, secondary subsystems and sensors are attached and unlabeled.

### 3.3.2 Graphical User Interface (GUI)

An LCD touchscreen (Juvtmall) graphical user interface (GUI) is used to control the data acquisition process. Users interact with the GUI via a finger or an attached stylist to press on-screen buttons or input text using an on-screen keyboard. The user interface was developed using the Python programming language. The home screen and testing screen are shown in Figure 3.4a and 3.4b respectively. On the home screen, pressing the “Collect Data” button navigates to the testing screen, where the user inputs the name of the data file to be saved to. A “Tare” button is available to zero the force sensor at any point. During testing, a live feed of the elapsed time, displacement, and force

measurement are displayed to ensure sensors are working properly, as shown in Figure 3.4b. After ending a test, an additional window is then created with a force-displacement graph, allowing an immediate check and feedback on the collected data. If the window is not closed before starting the next test, the force-displacement will be plotted on the same graph. This allows users to compare multiple plots' force responses, as shown in Figure 3.4c. If the window is closed, a new force-displacement graph will be created. The GUI utilizes a white background with dark text to help combat glare in the field.

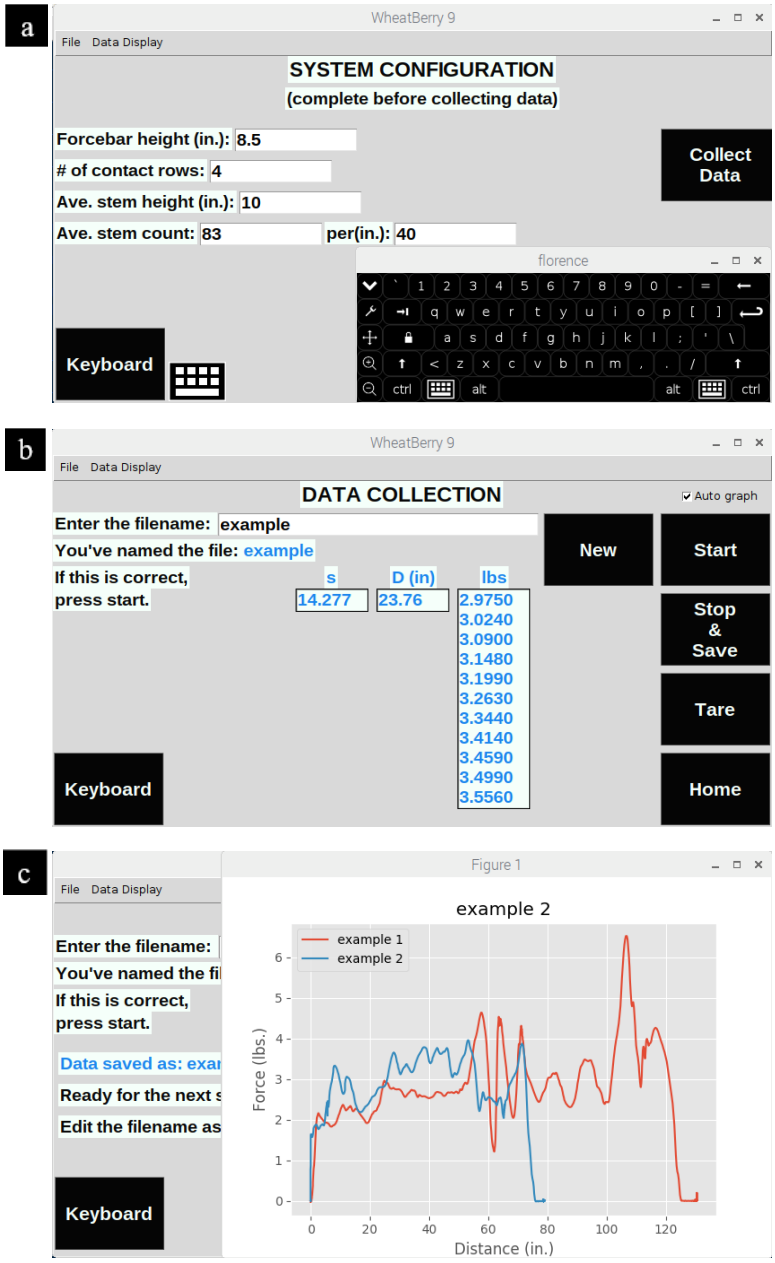


**Figure 3.4 (a)** GUI home screen. **(b)** Screen during testing. **(c)** Force displacement graph shown after testing.

3.3.3 Electronics

A Raspberry Pi computer (Raspberry Pi 3 Model B+) is the central component of the electronics system. It runs the GUI, sends commands to a microcontroller, and saves and processes data. Figure 3.5 provides a simplified diagram of the electronic system. The microcontroller (Arduino Uno Rev3, Arduino.cc) is connected to all sensors to digitize their signals. After initiation by the Raspberry Pi computer command, the microcontroller reads the sensor data and forwards it to the Raspberry Pi. The electronics system is powered by a lithium-Ion battery (PowerCore 20100, Anker). The battery enables the electronics to be powered for approximately 16 hours before requiring a recharge. To recharge the battery, a micro USB cable and power supply are required. The battery can easily be removed for remote charging.

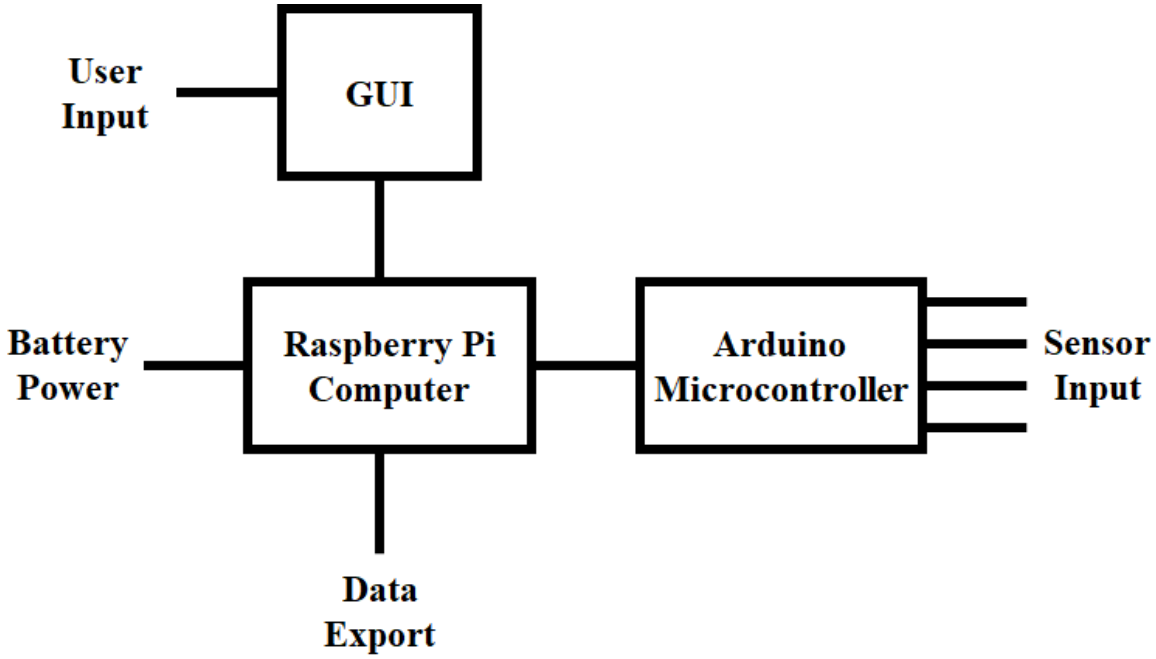


**Figure 3.5** Simplified diagram of major electronic components.

3.3.4 Sensors

Two sensors are used to measure a plot's resistance force and the SOCEM's displacement. The force sensor is a 50-lb S-beam load cell with overload protection (model FSH01020, Futek Advanced Sensor Technologies, Inc., Irvine, CA). The load cell is connected to the force bar by a bolt so that the force acting on the force bar is measured. A YUMO rotary encoder with a 1024 pulse per rotation (SparkFun Electronics, Niwot, CO) is linked with the rear wheel via a gear and timing belt

system to record the SOCEM displacement. Additional sensors, such as LiDAR, Ultrasonic, and ambient temperature and humidity sensors, can be incorporated into the SOCEM.

### 3.3.5 Data Files

Two data files are typically generated after testing. Immediately after a user presses the "Stop & Save," raw data is saved to a Microsoft Excel file. This includes force bar height, average stem height, average spacing estimation, elapsed time, force, and displacement. This file is saved under the user's inputted name after the label "RAW_". A second file, under the user's inputted name, saves the same raw data, automatic post-test data analysis, and a force-displacement graph to a Microsoft Excel file. The automatic post-test data analysis includes calculations of sampling rate, maximum force, mean force, median force, average test speed, and multiple flexural stiffness estimations. With just the force and displacement sensors, data is recorded at approximately 80 Hz.

### 3.3.6 Post-Test Data Analysis

The focal measurement obtained from the SOCEM test data is an estimation of the average stem flexural rigidity or $EI$, where $E$ is Young's modulus and $I$ is the cross-sectional moment of inertia. Flexural rigidity is measured for two principal reasons. Primarily, stem flexural rigidity is known to be highly correlated to stem strength [8, 11, 16] and $EI$ is directly related to buckling [18]. Thus, its measurement is a reliable assessment of lodging resistance. Secondly, compared to bending strength measurements, flexural rigidity measurements are non-destructive and the testing method for multiple plants is easier on the user (e.g., less input force).

Since an entire plot is tested, the number of stems and interactions among neighboring stems must be accounted for. To do so, the following simplifying assumption must be made: all stems are represented as identical cantilever beams with equivalent height and flexural stiffness that are fixed to the ground with a constant spacing between each stem. This allows the Multiple Inline Interacting Cantilever Beam Model (see Chapter 2), referred to here as the Interacting Model, to be utilized. Using this model calls for just four input parameters: peak force, stem length, force bar height, and spacing distance. The stem length, force bar height, and spacing are acquired from the averages of the measurements (details described in the 3.4 Testing Method). To obtain the peak force from the force-displacement data, a few steps are required. The model assesses a single row so the force response of a single row must be examined to obtain the average peak force. Dividing the SOCEM force measurements by the number of contact rows provides the needed force response. Before determining the peak force, it is important to only examine the data from the center of the plot to prevent distortion due to the "edge effect". The edge effect enables crops on the edges of the plots to have greater growth [19], often resulting in different phenotypes than the majority of the plot's crops.

Stronger resistance and taller crops were consistently observed at the start and end of plots in preliminary SOCEM data. Therefore, the data from the first and last 50 cm of a plot is removed. The most distinguishable force peaks from the force per row displacement plots are then identified and averaged. This can be done manually or automatically through software (e.g., PeakUtils Python library). An example plot is shown in Figure 3.6. Inputting the force bar height and averages from the peak force, stem length, and spacing distance into a Python script that follows the model calculates an estimated average stem *EI* for a given plot.

Since stems are randomly configured and the amount of interaction varies, the above process is repeated using a Multiple Inline *Non-Interacting* Cantilever Beam Model (see Chapter 2) or the Non-Interacting Model, which requires the same four inputs. An additional estimated average stem *EI* is generated from this model. The two *EI* estimations from the Interacting Model and Non-Interacting Model can then be averaged together.

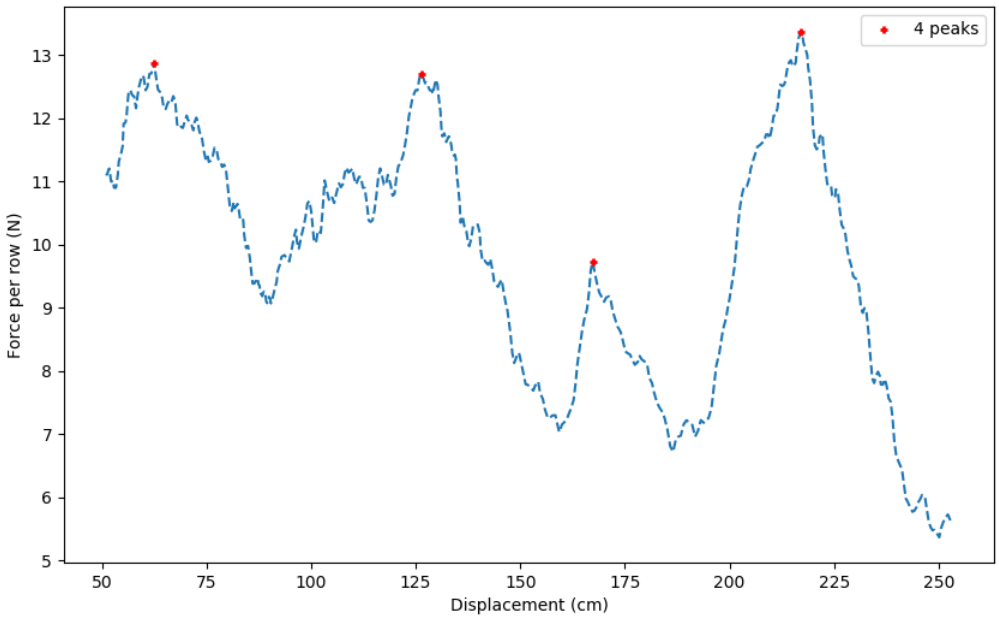


**Figure 3.6** Example force per row displacement plot with peak forces identified in red.

### 3.4 Testing Method

To ensure accurate data, the methods described in the upcoming paragraphs were utilized and currently recommended for future use. The process to properly set up a plot for testing is described first, followed by methods to determine a plot's average height and stem spacing distance.

### 3.4.1 Pre-Test

Prior to testing a plot, the following methods should be performed. To eliminate the edge effect [19], rows along the sides of a plot should not be tested. If needed, the side rows should be adjusted so no contact with the force bar is possible. Any debris in the test plot should be removed prior to testing to prevent interference with the plot's force resistance. This should be done carefully to prevent damage to the stems. At the start of each test, the force sensor should be tared after confirming nothing is in contact with the force bar. To load stems more naturally and improve accuracy, the force bar should be adjusted so that it is at 70-90% of the height of most stems (see Chapter 2 for further details). Remaining within these limits reduces potential error in the flexural rigidity calculations.

### 3.4.2 Stem Height and Spacing

Recall that the *EI* estimation calculations require inputs of the average height/length of the stems and the average spacing between stems. Since the plot has already been harvested by a combine, the height of neighboring clusters of stems should be similar. So, a sample row from each plot was selected in which the height of a cluster of stems was measured every 50 cm approximately. The mean plot height was then computed to be used as the input for calculations. To obtain an estimation of the average spacing, half the number of contact rows were examined for sampling counts. In approximately the center of a plot, the number of stems in a 100 cm stretch was counted for each sampling row. The 100 cm was then divided by the average number of stems to provide an estimation for the average spacing. This value was used for calculation inputs.

Autonomizing the process of determining the average height/length of the stems and the average spacing between stems is currently in the prototyping stages. This will rapidly decrease the total testing time, allowing for even higher throughput.

### 3.4.3 User Operation

To operate the SOCEM, the user initially positions the device at the front of a plot, as shown in Figure 3.7. After adjusting the height of the force bar if needed, the user then inputs the force bar height, the number of rows of stems that will contact the force bar, the average stem height, and the average stem count into the GUI home screen. On the testing screen, the user then inputs the name of the data file to be saved to. After taring the force sensor and pressing "Start," the user then pushes the SOCEM across the plot at a slow, steady rate. Once through the plot, the user presses the "Stop & Save" button to end the test. This process may then be repeated for more tests.

Note that it is currently recommended that a plot only be tested once with the SOCEM as testing can alter the system's geometry (e.g., angled stems) and force response. Preliminary data from

a simple experiment consistently showed reduced force responses when a plot was tested sequentially with the SOCEM. However, in the experiment, there was minimal delay between consecutive tests. Over a longer period between tests, stems may return to their original positions.

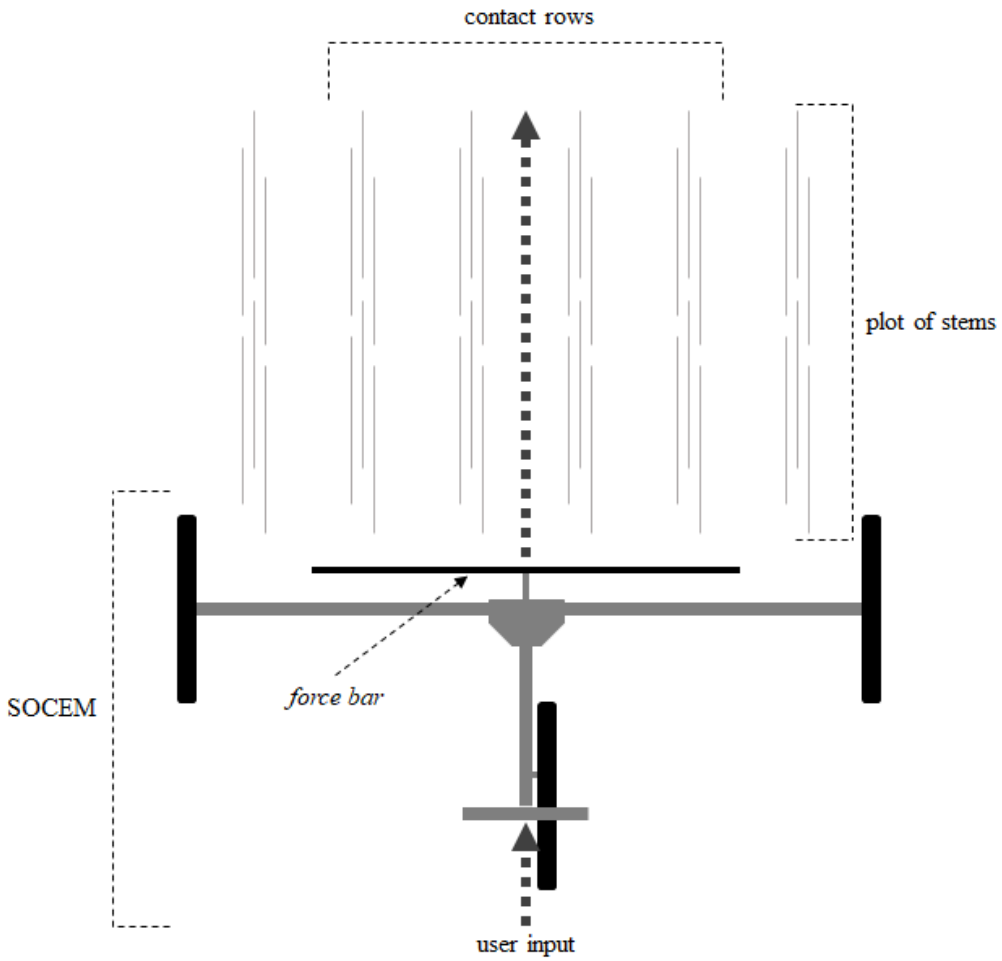


**Figure 3.7** Method of use diagram. The user first positions the SOCEM in front of the testing plot without making any contact as shown. The user inputs the number of contact rows (that will contact the force bar), force bar height, average stem height, and average stem density into the GUI. After zeroing the force sensor, the user then pushes the SOCEM through the plot.

### 3.5 Validation

Before examining stems with varying geometry and material properties, a simplified lab test was conducted to validate the SOCEM *EI* estimations. In particular, SOCEM *EI* estimations were compared to corresponding *EI* measurements of sheet metal sets obtained from three-point bending

tests and calipers. Details and results from the validation experiment are provided below. Note that the following information was presented previously in Chapter 2.

### 3.5.1 Experimental Setup

As illustrated in Figure 3.8, six rectangular sheet metal strips were securely placed directly inline, and equally spaced by width *s*. The SOCEM was then utilized to slowly drive the force bar across the beams to obtain the force-displacement plot. The force-displacement response was then analyzed and the Interacting Model was used to estimate the *EI* of the beams. The estimated *EI* values were then compared to actual *EI* values for each set of beams. Actual *EI* values were determined from three-point bending tests and calipers measurements (see Table 2.1).

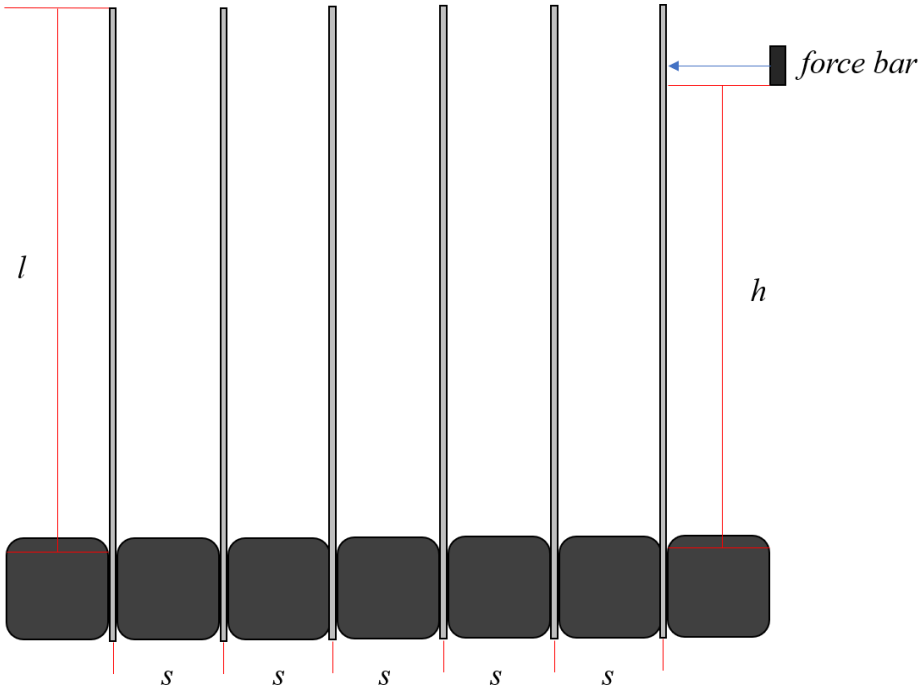


**Figure 3.8** Diagram of experimental setup. *l* - effective length of beams, *h* - minimum effective height of the force bar, *s* - width of spacing bars.

### 3.5.2 Test Specifics

Five sets of beams (A-E) with nearly equal *EI* values were created. Each set of beams were subjected to three SOCEM tests. The first test had a beam to beam spacing of 19.1 mm, the second a spacing of 24.9 mm, and the third a spacing of 49.9 mm. The height of the force bar was adjusted so that the beams would not yield but they would come into contact with at least one other beam during

the test. The beam length between sets of beams was also varied. Thus, all input parameters for the model are varied. Table 3.1 below, summarizes the testing conditions for all 15 experimental tests.

**Table 3.1** Conditions for each SOCEM validation test. Note that the effective *l* and *h* (with respect to the spacing bars) are listed. The expected peaks refer to the number of maximum force peaks that occur for a test with six beams.

| Set | *EI* (N mm$^2$) | *s* (mm) | *l* (mm) | *h* (mm) | Expected peaks |
|---|---|---|---|---|---|
| $A_1$ | 41900 | 24.9 | 180 | 167 | 4 |
| $B_1$ | 63000 | 24.9 | 180 | 165 | 4 |
| $C_1$ | 111000 | 24.9 | 231 | 219 | 4 |
| $D_1$ | 154000 | 24.9 | 205 | 191 | 4 |
| $E_1$ | 335000 | 24.9 | 231 | 219 | 4 |
| $A_2$ | 41900 | 49.9 | 180 | 167 | 5 |
| $B_2$ | 63000 | 49.9 | 180 | 165 | 5 |
| $C_2$ | 111000 | 49.9 | 231 | 219 | 5 |
| $D_2$ | 154000 | 49.9 | 205 | 191 | 5 |
| $E_2$ | 335000 | 49.9 | 231 | 224 | 5 |
| $A_3$ | 41900 | 19.1 | 186 | 175 | 3 |
| $B_3$ | 63000 | 19.1 | 186 | 175 | 3 |
| $C_3$ | 111000 | 19.1 | 237 | 225 | 3 |
| $D_3$ | 154000 | 19.1 | 211 | 198 | 3 |
| $E_3$ | 335000 | 19.1 | 237 | 225 | 3 |

### 3.5.3 Validation Results

Each set of beams' mean, measured *EI* was plotted against the SOCEM's estimated *EI*, as shown in Figure 3.9. Fitting a linear regression (blue line) to the plot yields $R^2 = 0.99$ and a slope of 0.945, indicating the SOCEM's measurements are highly correlated but underpredicted *EI*. The "ideal" line describing the theoretical case in which all SOCEM *EI* estimations were equivalent to all measured *EI*, has been shown in red. Assuming the mean, measured *EI* to be the true value, the SOCEM *EI* estimations yielded a mean absolute percent error of 10.92% with a standard deviation of 6.98%.

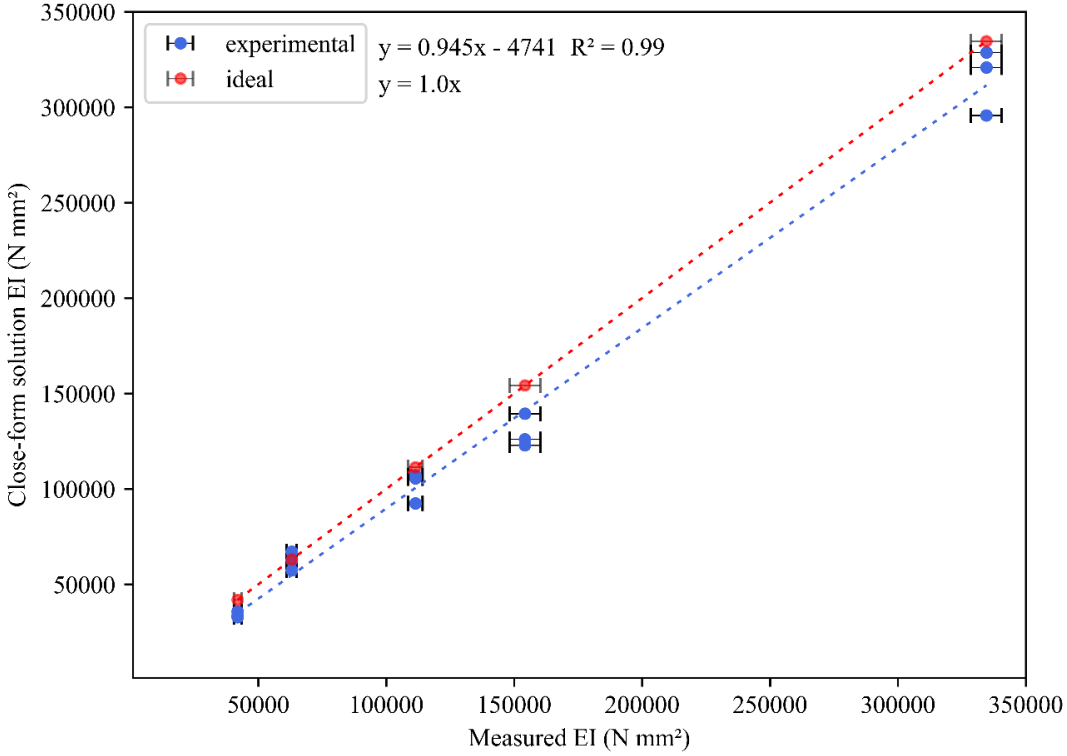


**Figure 3.9** *EI* linear regression of the SOCEM's prediction. The closed-form solution or the SOCEM's predicted *EI* (N mm$^2$) plotted against the measured *EI* (N mm$^2$). Linear regression blue line shows $R^2 = 0.99$ and slope of 0.945. Error bars represent the standard deviation of the measured *EI*. The red line shows the theoretical, ideal case of $y = x$ to indicate accuracy.

### 3.6 Preliminary Results

The preliminary data obtained from the SOCEM is promising. During the Summer of 2019, the SOCEM was used to test over 70 wheat plots at the University of Idaho Arboretum. Data from the SOCEM was then used to compute estimations of *EI* from each plot. The estimated *EI* values were then compared to historical lodging percentages. Details and the results are provided below.

Historical wheat lodging percentages from 2016-2019 from six Idaho locations (Bonners Ferry, Nezperce, Genesee, Moscow, Tammany, Tensed) were obtained from variety trials provided in Northern Idaho Small Grain and Grain Legume Research and Extension Program reports [20]. While 70 plots were tested with the SOCEM, many of the varieties had limited lodging data available from the variety trials so a data selection filtering process was first conducted before comparing results. Many varieties were not planted over more than one year and/or location. As mentioned in 1.4.1 Lodging Counts, without enough data points over multiple years and environments, it is difficult to

understand a variety's resistance to lodging due to the numerous confounding environmental factors. For each variety tested by the SOCEM, there was a potential maximum of 24 lodging percentage data points from four years and six locations, but most varieties had fewer data points. To compare then, only varieties with at least 10 data points were evaluated. This provided 31 tested plots (with some repeated varieties) in which *EI* estimations were made. For each variety, the mean percent lodging from all its available data points was computed.

A linear regression analysis between the SOCEM measurements and historical lodging percentage would typically be conducted; however, this would provide limited insight as the plots tested were elite, commercial hybrids. Among such varieties, there are rare lodging occurrences, despite varying stem phenotypes. As an alternative analysis, the varieties were classified into either a lodging prone or lodging resistant group, in which the division was made at 7% lodging. Only three plots from the variety named "UI Silver" were placed in the lodging prone group, with a mean percent lodging of 25%. The lodging resistant group possessed a lodging percentage mean of 1.23% and a median of 0.15%.

The estimated mean *EI* values (averaged from the Interacting and Non-Interacting Models) were compared between the two groups, as presented in Figure 3.10. Error bars represent the standard deviation. The lodging resistant plots had a mean, estimated *EI* of about 310 N $cm^2$ (SD. = 62 N $cm^2$), whereas the lodging prone plots possessed a mean, estimated *EI* of about 200 N $cm^2$ (SD. = 12 N $cm^2$). Both estimations are reasonable values as 270 N $cm^2$ is typically reported in the literature [21]. An independent t-test was conducted with $\alpha = 0.01$ and the assumption of unequal variance. The t-test indicated the mean estimated *EI* values between the lodging resistant and lodging prone groups are significantly different with a $p$ value $< 0.001$.

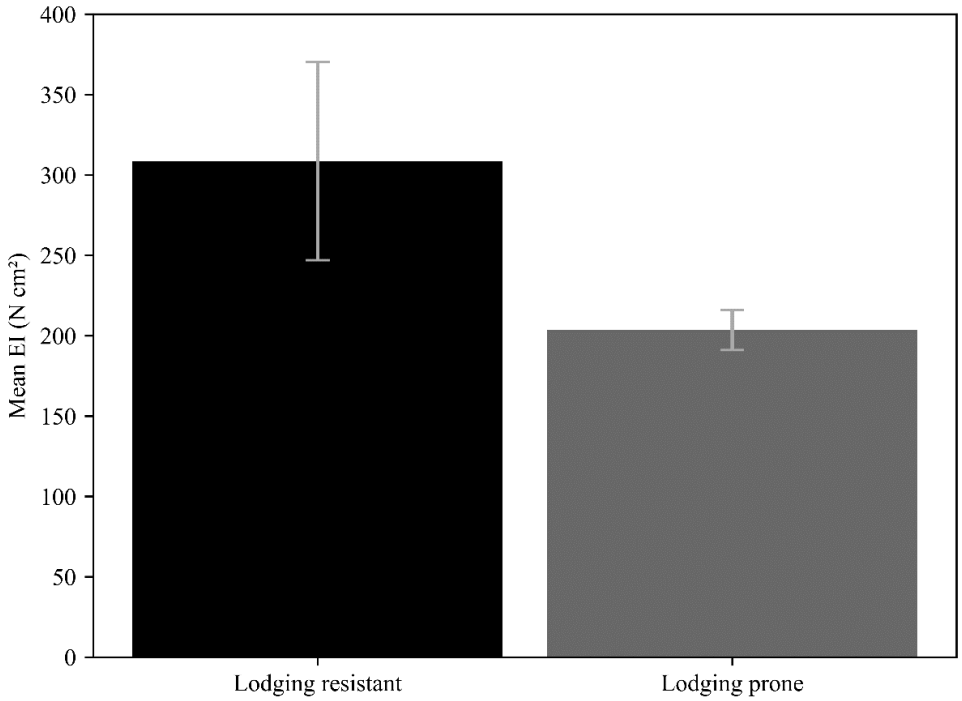


**Figure 3.10** Mean estimated *EI* of lodging resistant varieties (<7% mean lodging) compared to a lodging prone variety (25% mean lodging).

## 3.7 Discussion

The SOCEM possesses many benefits, but it is subjected to limitations due to human factors and technical factors. Its benefits are discussed, followed by its limitations and lastly the future work involved.

### 3.7.1 Benefits

The SOCEM is a user-friendly, field tool for farmers and plant breeders to rapidly and accurately assess stem lodging via a non-destructive and natural-like loading method. It is important to highlight the fact that applying natural bending enables more accurate phenotyping of stalks. Due to the complex, hierarchical, biological structure of stems, unnatural loading can result in erroneous assessments of lodging resistance [22, 23]. More notably, the SOCEM has the highest throughput compared to any current method. By testing entire plots at a time, it is able to obtain stiffness data from hundreds or even thousands of stems in the span of a few minutes. With such high throughput and large sample sizes, comprehensive phenotyping of hybrids becomes more economically feasible.

This could lead to a significantly increased understanding of how genetics affect stalk strength and thus, more lodging resistant crops.

### 3.7.2 Limitations

In its current state, the SOCEM contains limitations due to both human factors and technical factors. User-to-user variability may affect testing results. There is likely to be some variation in manual measurements of height and crop counts (for spacing estimations) between users. Additionally, the manner in which a user pushes the SOCEM through plots during testing should be controlled. For clean data, the SOCEM should be pushed through plots at a slow, steady walking pace to reduce error and inertial effects. Users can easily be trained to implement such testing protocols. Labor costs are also involved in the SOCEM's operation.

Technical factors of the SOCEM arise due to its current design and some assumptions involved in calculations. With the current force sensor and device size, only small grain crops may be tested. Large grain crops may exceed the 50-lb limit of the force sensor when testing multiple crops. The height of the device and force bar are too low to properly test large grain crops as well, since unnatural loading would be implemented, stems may fracture, and the user is unlikely to be able to smoothly push through a plot.

The SOCEM and its method are primarily designed to test stubble, but it is also possible to test plots at any time. Although, if testing occurs pre-harvest, reduced accuracy in measurements may occur as the weight and influence of the crop's head is not accounted for in the methods. Additionally, some plants may be damaged, depending on the setup.

As mentioned in 3.4 Testing Method, there may be a limitation on the number of SOCEM tests performed on a plot. After a test, the SOCEM often alters the plot's geometry by leaving stems at a slight angle. If tested again, at least with little delay between tests, the force response will be reduced, leading to inaccurate results and invalidating comparisons to other plots. Over extended time between tests, the stems may return to their original positions to allow for additional tests, but this has not been confirmed yet.

The equations involved in the Interacting Model and its alternative Non-Interacting Model utilized a number of simplifying assumptions. The models use the perspective of straight, identical, uniform, cantilever beams that are equally spaced apart. In reality, this is not the case. The orientation of the stems varies, but often are approximately straight. The stems are not identical nor uniform and the spacing between each stem also varies. Additionally, the force bar height is assumed to be constant; yet, with a rough, uneven soil surface in the field, the force bar height will experience small changes with respect to the ground. If set within the recommended force bar range (70-90% plot

height), the effect of these changes is minimal. Without these simplifying assumptions, such a quick analysis of the stem stiffness is currently not possible. The relatively small variation within a plot's geometry allows averages to efficiently describe most of the plot.

The equations also assume that each stem is securely fixed in the ground. The validity of such an assumption depends on the soil conditions and root system. If the soil is dry with high clay content (as was the case in 3.6 Preliminary Results), the stalk and root crown rotation is limited [16], giving more accurate results than if testing occurs with wet, sandy, or loose soil. When the fixed ground assumption is not met, tests are likely to underpredict flexural stiffness, as observed with other devices [16].

### 3.7.3 Future work

The validation testing shows the SOCEM can accurately predict flexural stiffness in a controlled environment and the preliminary data suggests it can assess stalk lodging resistance. To fully confirm that its flexural stiffness measurements can predict stalk strength, a full experiment is planned for Summer 2020. The SOCEM will be used to collect data on several wheat hybrids, which will then be compared to three-point bending strength tests conducted in the lab.

While the SOCEM already is a high throughput device, the manual height and crop count measurements reduce the testing rate. Additional SOCEM sensors are currently being prototyped to automate the height and spacing estimation process. This was previously attempted, but the measurements obtained by the sensors were not precise enough for accurate stiffness estimations. The authors are likely to upgrade to advanced LiDAR (Light Detection and Ranging) and camera sensors to obtain accurate data on crop height and spacing estimation [24, 25]. Further in the future, testing is likely to become autonomous, almost entirely removing human operation. To do so, the SOCEM would be attached to the back of a harvest combine. With such a method, data would be instantly obtained during harvesting at no extra labor cost.

In its current design, the SOCEM is configured to test small grains, but its concept can easily be applied to large grains. In fact, increased accuracy is likely to occur with larger grains, especially as the height and spacing will be easier to estimate for users or automatic sensors. To test larger grains, the scale of the device would have to increase, along with the force sensor's capacity. The same assumptions and testing protocol would still apply.

## 3.8 Conclusion

The SOCEM provides a simple, field method for assessing stalk strength at higher throughputs than any previously existing device. Testing typically occurs after harvest so it is considered non-destructive while replicating natural stem loading. It measures stalk stiffness, which is

highly correlated to stalk strength and therefore lodging resistance. Thus, its phenotyping can be applied to connect genetics to stalk strength, allowing breeders to reduce the risk of lodging in small grains. The device will be modified to also assess large grains in the near future.

### 3.9 References


[1] Rajkumara, S. 2008. "Lodging in Cereals - A Review." *Agricultural Reviews* 29: 55–60.

[2] Berry, P.M., and J. Spink. 2012. "Predicting Yield Losses Caused by Lodging in Wheat." *Field Crops Research* 137 (October): 19–26. https://doi.org/10.1016/j.fcr.2012.07.019.

[3] Berry, P. M., R. Sylvester-Bradley, and S. Berry. 2007. "Ideotype Design for Lodging-Resistant Wheat." *Euphytica* 154 (1–2): 165–79. https://doi.org/10.1007/s10681-006-9284-3.

[4] Duvick, Donald N. 2005. "The Contribution of Breeding to Yield Advances in Maize (Zea Mays L.)." *Advances in Agronomy* 86: 83–145.

[5] Mulder, E. G. 1954. "Effect of Mineral Nutrition on Lodging of Cereals." *Plant and Soil* 5 (3): 246–306. https://doi.org/10.1007/BF01395900.

[6] Laude, H. H., and Arland W. Pauli. 1956. "Influence of Lodging on Yield and Other Characters in Winter Wheat [1]." *Agronomy Journal* 48 (10): 452–55. https://doi.org/10.2134/agronj1956.00021962004800100005x.

[7] Neenan, M., and J. L. Spencer-Smith. 1975. "An Analysis of the Problem of Lodging with Particular Reference to Wheat and Barley." *The Journal of Agricultural Science* 85 (3): 495–507. https://doi.org/10.1017/S0021859600062377.

[8] Berry, P. M., M. Sterling, J. H. Spink, C. J. Baker, R. Sylvester-Bradley, S. J. Mooney, A. R. Tams, and A. R. Ennos. n.d. "Understanding and Reducing Lodging in Cereals." *Advances in Agronomy*, 217–71.

[9] Erndwein, Lindsay, Douglas D. Cook, Daniel J. Robertson, and Erin E. Sparks. 2020. "Field-Based Mechanical Phenotyping of Cereal Crops to Assess Lodging Resistance," February. https://arxiv.org/abs/1909.08555v3.

[10] Berry, P. M., J. Spink, M. Sterling, and A. A. Pickett. 2003. "Methods for Rapidly Measuring the Lodging Resistance of Wheat Cultivars." *Journal of Agronomy and Crop Science* 189 (6): 390–401. https://doi.org/10.1046/j.0931-2250.2003.00062.x.

[11] Robertson, Daniel J., Shien Yang Lee, Margaret Julias, and Douglas D. Cook. 2016. "Maize Stalk Lodging: Flexural Stiffness Predicts Strength." *Crop Science* 56 (4): 1711. https://doi.org/10.2135/cropsci2015.11.0665.

[12] Stubbs, Christopher J., Yusuf Oduntan, Tyrone Keep, Scott D. Noble, and Daniel J. Robertson. 2020. "The Effect of Self-Loading on the Mechano-Stability and Stalk Lodging

Resistance of Plant Stems." *BioRxiv*, March, 2020.03.21.001727. https://doi.org/10.1101/2020.03.21.001727.

[13] Shah, D. U., T. P. S. Reynolds, and M. H. Ramage. "The Strength of Plants: Theory and Experimental Methods to Measure the Mechanical Properties of Stems." *Journal of Experimental Botany* 68 (July 20, 2017): 4497–4516. https://doi.org/10.1093/jxb/erx245.

[14] Guo, Qingqian, Ruipeng Chen, Xiaoquan Sun, Min Jiang, Haifeng Sun, Shun Wang, Liuzheng Ma, Yatao Yang, and Jiandong Hu. 2018. "A Non-Destructive and Direction-Insensitive Method Using a Strain Sensor and Two Single Axis Angle Sensors for Evaluating Corn Stalk Lodging Resistance." *Sensors* 18 (6): 1852.

[15] Heuschele, D. Jo, Jochum Wiersma, Leonard Reynolds, Amy Mangin, Yvonne Lawley, and Peter Marchetto. 2019. "The Stalker: An Open Source Force Meter for Rapid Stalk Strength Phenotyping." *HardwareX*, e00067.

[16] Cook, Douglas D., Witold de la Chapelle, Ting-Che Lin, Shien Yang Lee, Wenhuan Sun, and Daniel J. Robertson. 2019. "DARLING: A Device for Assessing Resistance to Lodging in Grain Crops." *Plant Methods* 15 (1): 102.

[17] Feng, Suwei, Dechuan Kong, Weihua Ding, Zhengang Ru, Gan Li, and Liyuan Niu. 2019. "A Novel Wheat Lodging Resistance Evaluation Method and Device Based on the Thrust Force of the Stalks." *PLOS ONE* 14 (11): e0224732. https://doi.org/10.1371/journal.pone.0224732.

[18] Gere, James M., and Stephen P. Timoshenko. 1961. *Theory of Elastic Stability*.

[19] Watson, D. J., and S. A. W. French. 1971. "Interference between Rows and between Plants within Rows of a Wheat Crop, and Its Effects on Growth and Yield of Differently-Spaced Rows." *Journal of Applied Ecology* 8 (2): 421–45. https://doi.org/10.2307/2402881.

[20] "Variety Trials." n.d. Accessed December 7, 2020. https://www.uidaho.edu/extension/cereals/north/variety-trials.

[21] Hirai, Yasumaru, Eiji Inoue, Masami Matsui, Ken Mori, and Koichi Hashiguchi. 2003. "Reaction Force of a Wheat Stalk Undergoing Forced Displacement." *Journal of the Japanese Society of Agricultural Machinery* 65 (2): 47–55.

[22] Robertson, Daniel, Simeon Smith, Brian Gardunia, and Douglas Cook. 2014. "An Improved Method for Accurate Phenotyping of Corn Stalk Strength." *Crop Science* 54 (5): 2038. https://doi.org/10.2135/cropsci2013.11.0794.

[23] Robertson, Daniel J., Margaret Julias, Brian W. Gardunia, Ty Barten, and Douglas D. Cook. 2015. "Corn Stalk Lodging: A Forensic Engineering Approach Provides Insights into Failure Patterns and Mechanisms." *Crop Science* 55 (6): 2833–41. https://doi.org/10.2135/cropsci2015.01.0010.

[24] Yuan, Wenan, Jiating Li, Madhav Bhatta, Yeyin Shi, P. Stephen Baenziger, and Yufeng Ge. 2018. “Wheat Height Estimation Using LiDAR in Comparison to Ultrasonic Sensor and UAS.” *Sensors (Basel, Switzerland)* 18 (11). https://doi.org/10.3390/s18113731.

[25] Liu, Shouyang, Fred Baret, Denis Allard, Xiuliang Jin, Bruno Andrieu, Philippe Burger, Matthieu Hemmerlé, and Alexis Comar. 2017. “A Method to Estimate Plant Density and Plant Spacing Heterogeneity: Application to Wheat Crops.” *Plant Methods* 13 (1): 38. https://doi.org/10.1186/s13007-017-0187-1.

# Chapter 4: Future Work and Conclusion

## 4.1 Introduction

The featured work in this thesis was two-fold. First, a general, pioneering model that accounts for large deflections of multiple, interacting cantilever beams was derived. Secondly, a new, electromechanical device that utilizes the presented model was described, highlighting its ability to rapidly evaluate the stalk strength of grains. Both aspects of this thesis are significant advances in their fields, but this is just the beginning of their development. Suggestions for future work on the Multiple Inline Interacting Cantilever Beam Model and the SOCEM are provided here respectively. An overarching conclusion then follows.

## 4.2 Multiple Inline Interacting Cantilever Beam Model Improvements

Using multiple, pseudo-rigid body models (PRBM) [1,2] the Multiple Inline Interacting Cantilever Beam Model presented in Chapter 2 was shown to possess predictive capabilities. However, the assumptions and simplified perspective that the model applies, limits its effective range and accuracy. With the foundation provided by this thesis, additional research can be conducted to expand the model. The following provides suggestions for exploring alternative beam geometry, developing a multi-beam end angle correction factor, and incorporating beam coordinates.

### 4.2.1 Beam Geometry

All experiments utilized beams with prismatic, rectangular geometry, so a next step includes examining alternative geometry. With prismatic geometry, inline beams only deflect forward, guaranteeing steady contact between multiple beams. There is no sliding out of contact. Beams with non-rectangular faces are likely to exhibit different mechanics, potentially affecting the accuracy and range of the model. Beams with solid and hollow circular cross-sections are of particular interest, as this geometry better describes existing systems such as crops. Bending circular-cross sectional beams with an applied force bar can also cause torsional deflection and sliding. As a result, the effect of interactions may be reduced. Therefore, the model may not accurately describe the mechanics of such systems. When examining the model's accuracy for alternative geometry, it is best to first investigate the simpler case of a single beam deflecting due to an applied force bar before investigating the more complex case of an inline row of beams. For an in-depth analysis, all system geometry ($l$, $h$, and $s$) should be fully varied. A similar method using physical and FEM experiment as described in 2.4 Data Triangulation to Assess Accuracy of the Closed-Form Solution is applicable.

### 4.2.2 Multi-Beam End Angle Correction Factor

While the PRBM beam end angle is accurate for single cantilever beams, the correction factor involved in such is inadequate for multiple interacting beams. The additional forces due to interacting beams alters the end angle. As seen in Chapter 2, with greater interactions (smaller spacing and larger deflections) error in the closed-form solution increases. Furthermore, analyzing the horizontal force component response yielded significantly more error due to the inaccurate beam end angle utilized to estimate the total force peak. In applications, it is often easier to measure the horizontal force component acting on a force bar, as seen in the SOCEM's current design. Therefore, developing a multi-beam end angle correction factor would be highly advantageous. Most likely through an FEM parametric study, a correction factor should be developed to improve model accuracy. The correction factor is likely to primarily be a function of deflection (or the ratio of force bar height to beam height) and beam-to-beam spacing. However, the beam geometry may influence the multi-beam end angle so it should also be explored.

### 4.2.3 Coordinates of Beams

In natural systems, the beams have various placement, allowing some to be considered inline, and others not. Perhaps taking the mean between the Non-Interacting and Interacting Model is a sufficient estimate, but the degree of interaction is ultimately unknown. However, if the x and z coordinates (viewed aerially, see Figure 2.1) were obtained, much of the uncertainty involving the spacing and degree of interaction between beams would be eliminated. In fact, a relatively simple computational program could run a multi-PRBM simulation featuring beams placed at their specific coordinates. From this, the number of beams interacting with one another would be known, assuming the height of the force bar and beams remains known. Such a program would be similar to the Interacting Model but with increased accuracy. This would particularly be useful with systems consisting of multiple rows.

## 4.3 SOCEM Improvements

The SOCEM design documented in this thesis presents a first, functional prototype with a beneficial design, yet several redesigns and additions are recommended. A discussion outlaying possible directions for the SOCEM is hereby presented. First, GUI improvements and additional sensors are suggested, followed by a force bar system redesign recommendation. Lastly, and most importantly, sensors to measure crop height and spacing are discussed.

### 4.3.1 GUI Improvements

The GUI described in 3.3.2 is an established prototype, but user experience could be even further improved with additional design work and feedback. For example, it may be advantageous to

give users the option to examine past data easier. Currently, a folder must be opened outside the GUI. Also, the visualization to monitor proper data collection during SOCEM testing could be improved. The current design displays a live feed list of force and displacement numbers as the SOCEM is pushed across a plot. However, a live feed force-displacement graph would be more appealing and effective. This was previously attempted, but lag was experienced. A faster and more powerful processing unit (under development) is likely to allow for a live feed graph.

The hardware could also be upgraded without much cost increase. A larger touchscreen would allow users to more accurately use their fingers as inputs. With the current five-inch touchscreen, the attached stylist is much more effective than fingers, but many users may prefer finger input.

### 4.3.2 Supplementary Sensors

A few additional sensors could be attached to the SOCEM for greater data collection. For instance, pairing the load-cell with an accelerometer or gyroscope to record its angle can improve force measurement accuracy, especially in a field. The terrain in the field is uneven so the load-cell will experience small changes in its orientation, which can transgress the assumption that it is measuring $F_x$. The weight of the force bar can also influence load-cell measurements during angle changes, although its effect is small due to its lightweight design. It would be possible to correct for this if the angle of the load-cell was known.

A temperature and humidity sensor would also be beneficial, particularly since the environment can influence the mechanical properties of crops. Consider turgor pressure, the hydrostatic pressure exerted on a plant's cell wall, which influences plant biomechanics on several biomechanical levels [3]. The humidity is known to influence turgor pressure [3, 4], so it should be recorded during testing. These sensors could easily be integrated into the SOCEM design.

### 4.3.3 Force Bar System Redesign

To reduce failure risk and potential erroneous measurements, the force bar system should be redesigned slightly. From a design failure mode and effects analysis, the FUTEK S-beam load-cell of the force bar system possess the highest risk priority number (combined weighting of severity, likelihood, and detectability), supporting its redesign. The load-cell is the most expensive and critical component of the SOCEM's primary function (obtaining resistance force measurements). During transportation, it is at risk of breaking if its maximum load capacity is exceeded (e.g., dropping the SOCEM, insecure transportation). In its current design, nothing is protecting the load cell from overload. Thus, a simple mechanism to absorb any load during non-testing times is recommended. A

protective bar on a locking hinge to rotate in front of the force bar during transportation could easily be added.

As described in 2.6.3, the closed-form solution is sensitive to the ratio of the force bar height to beam/stem height, meaning that errors in either measurement can contribute to error in *EI* predictions. To reduce the chance of error then, the force bar height measurement should be as accurate as possible. Currently, users adjust the force bar height with two, 80/20 linear bearing sliders, allowing for any height to be set within its continuous range. Users then read the indicated $1/16^{th}$ inch ruler and input the reading into the SOCEM GUI. Users must also confirm the force bar is level using a separate level tool. While a level could easily be attached to the SOCEM, a different direction is suggested to further reduce measurement error and user effort. Instead, the design could be modified so push-button spring pins are used to adjust the force bar height to known, discrete level heights. Users could then simply enter a force bar label number into the GUI, or the process could even be automated with sensors (e.g. potentiometer, photogates). This design would provide an easier experience for users and reduce user input error of the force bar height, reducing error in *EI* measurements.

Depending if a multi-beam end angle correction factor is developed for the closed-form solution, a bi-axial load cell may be used to greatly reduce erroneous *EI*. As seen in Chapter 2, as deflections increase, error in *EI* predictions significantly increase due to inaccurate estimations of *F* from its $F_x$ estimation. This is a considerable issue for the current SOCEM design as $F_x$ is only measured with the single-axis load cell. Replacing the current load-cell with one capable of measuring both $F_x$ and $F_y$ would allow for an accurate determination of *F* and increase the effective range of the closed-form solution and SOCEM force bar. However, a bi-axial replacement is likely to cost four times as much as the current load-cell and implementing one with a force bar may be difficult due to bi-axial load cell designs. Thus, it may be best to continue with the current load-cell and remain within the force bar height limitation of 70-90% beam height.

### 4.3.4 Crop Height Sensors

While measuring stem height manually (as described in 3.4.2 Stem Height and Spacing) is relatively easy and quick, it would be beneficial to automate measurements. Several inexpensive prototypes were developed but were deemed inadequate. Their designs and issues are briefly described. Two simple systems used ultrasonic and LiDAR sensors positioned at a known height above stems, sending signals down to be rebounded by the tops of stems. Using time of flight, the distance could be measured to extrapolate crop height measurements. However, due to the thin

structure of the stems, both sensors cannot detect the stems, at least with the inexpensive sensors used.

A more advanced height estimation system was also experimented with an ultrasonic, LiDAR, and photogate sensor, as depicted in Figure 4.1. In the system, a stepper motor would first drive a horizontally orientated sensor upward via a timing belt until a limit switch, at a known height above all stems, was hit. The stepper motor would then lower the sensor until it detected stems in front of it. As the SOCEM went through a plot, the sensor would be lowered or raised to remain at the top of the row of stems. Unfortunately, this method was limited by the sensor. Again, the ultrasonic and LiDAR could not adequately detect the top of the stems due to the thin structures. The sensors detected the stems eventually, but the location ultimately depended upon how much obstruction the stems caused (i.e., how dense the stems were). Orientating the sensor at an angle to view both the front and side of a row improved results, but measurements were still under and inconsistent. Using a photogate as the sensor in this system was briefly examined. This was able to detect stems, but, unlike the ultrasonic and LiDAR, this sensor does not project along a row. Thus, since the SOCEM moves forward through a plot, the stems move through the photogate's thin IR beam, which does not provide enough time to readjust its position to the top of stems using the previous control algorithm. Instead, the photogate tends to lower itself as it goes through the plot. Using a series of several IR beams may allow the sensor to properly update its position. The control algorithm should only lower the sensor if all IR beams are unblocked, otherwise the sensor should be raised. While this system has potential for being viable, there are associated negatives. For example, an additional battery pack to operate the stepper motor is required. There are also several moving parts, increasing the chance of SOCEM failure.

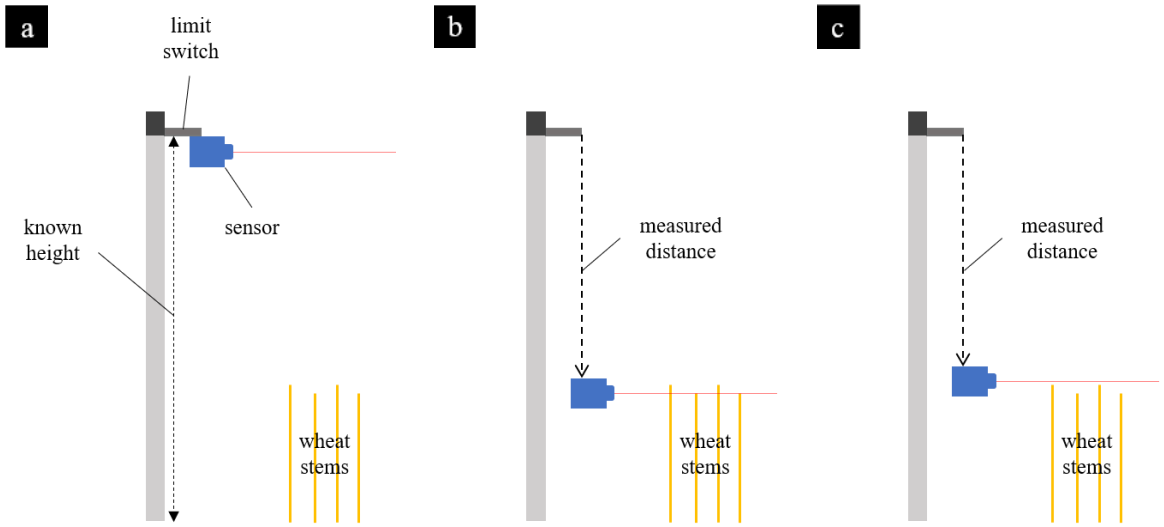


**Figure 4.1** Diagram of a height estimation system prototype. The initial step **(a)** involves a stepper motor raising a stepper motor to a limit switch at a known height. The sensor will then lower itself until the wheat stems are detected as shown in **(b)**, with the distance the sensor moved measured by the stepper motor. The sensor will then update its position until its above stems within a short distance, as shown in **(c).** The sensor will alternate between **(b)** and **(c)**, taking samples of height measurements.

An alternative method, without any moving sensors, includes using an advanced LiDAR sensor to obtain point cloud data from a top view. This has successfully been performed for several wheat varieties with 200 height values obtained from each experimental plot [5]. However, the varieties examined in [5] appear to be dense, pre-harvested plots. A reduction in accuracy may occur if testing post-harvested plots with just stems. Additionally, such a sensor is expensive and the data collected may be difficult to analyze due to its sheer size [6]. It may be possible to limit the sampling rate and only assess the greatest heights obtained in the point cloud. Despite the cost and increase in computation, it may be worth it to utilize advanced LiDAR since the closed-form solution is sensitive to the ratio of the force bar height to the stem length. The force bar height can be well controlled, so error primarily resides in measurements of stem height. The quantity of error is demonstrated in the following example.

Figure 4.2 provides the numerical derivative of the closed-form solutions *EI* with respect to stem length across realistic stem heights (or lengths) and a realistic stem spacing range observed within experimental wheat plots. The force bar height was constant at 15 cm and the inputted force peak was always 10 N. From the tests of the 70 wheat plots described in 3.6 Preliminary Results, a typical spacing estimation was about 1 cm. Consider, at a spacing of 1 cm and an estimated stem height of 20 cm ($h/l$ = 0.75), each centimeter off of the true stem length, can affect *EI* estimations by about 20 N cm$^2$, assuming the force bar height, spacing, and peak force measurements were exact. At

greater *h/l* ratios, spacings, and forces, errors in stem height measurements can have even greater influence on *EI* estimations. For wheat stems, when the difference between lodging prone and resistance varieties is only about 110 N cm$^2$ as shown in 3.6 Preliminary Results, erroneous *h/l* estimations could be significant.

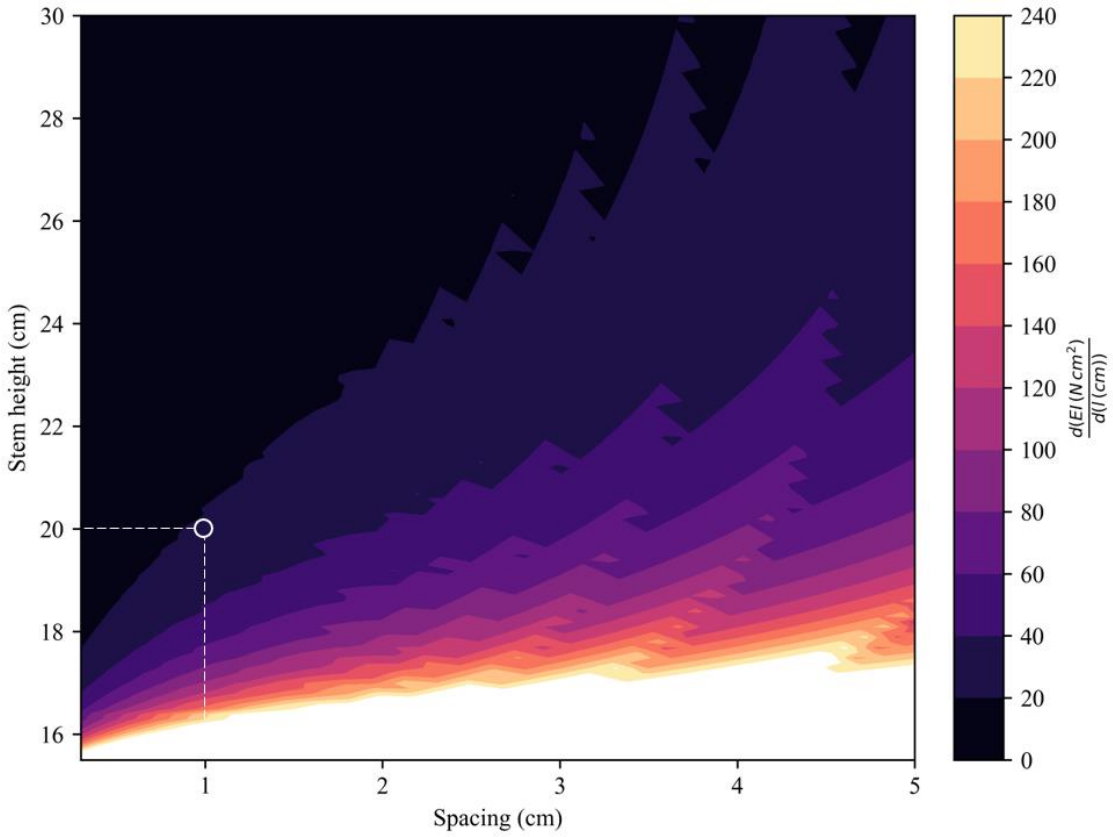


**Figure 4.2** Contour plot of the closed-form solution's *EI* numerical derivative with respect to stem height (N cm$^2$) across a realistic range of stem heights and a realistic stem spacing range observed within experimental wheat plots. The force bar height was constant at 15 cm. Force peak was constant at 10 N. A typical wheat spacing of 1 cm and stem height of 20 cm is highlighted, showing an *EI* derivative of about 20 N cm$^2$.

### 4.3.5 Spacing Sensors

Implementing sensors to estimate the spacing between beams is an improvement that would provide the most benefit to the SOCEM. The current, manual method of counting stems within a 100 cm stretch (described in 3.4.2) is slow and tedious. That process is the bottleneck of testing. Sensors to automate measurements to estimate spacing would increase the rate of testing significantly, increasing throughput even more. Furthermore, sensors are likely to increase the accuracy of the spacing estimations, which could significantly increase *EI* estimation accuracy. The following

example supports the need for accurate estimations of spacing. Figure 4.3 illustrates the numerical derivative of the closed-form solutions *EI* with respect to spacing across ratios of force bar height to stem length (*h/l*) and a realistic stem spacing range observed within experimental wheat plots. The stem length and force peak were held constant at 20 cm and 10 N, respectively. At a typical spacing of 1 cm, with a *h/l* of 0.7 (least error prone configuration within the closed-form solution limitations), each centimeter off of the true spacing, can affect *EI* estimations by about 40 N cm$^2$, assuming the unlikely situation of an exact *h/l* and peak force measurements. At greater spacings, *h/l*, or forces, errors in spacing estimations will have greater consequences on *EI* estimations. Again, with seemingly little difference between the flexural stiffness of lodging prone and resistant wheat varieties, spacing measurement errors should be reduced as much as possible.

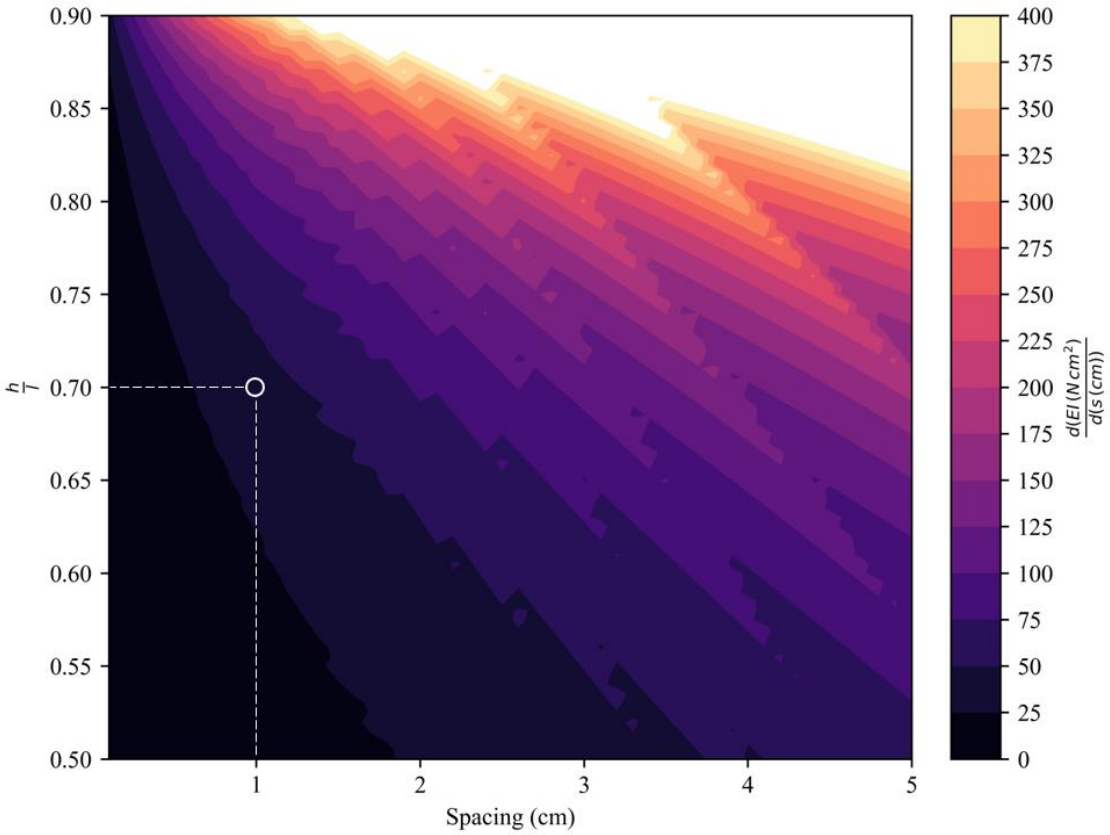


**Figure 4.3** Contour plot of the closed-form solution's *EI* numerical derivative with respect to spacing (N cm$^2$) across ratios of force bar height to stem length (*h/l*) and a realistic stem spacing range observed within experimental wheat plots. The force peak was constant at 10 N. A typical wheat spacing of 1 cm and *h/l* = 0.7 is highlighted, showing an *EI* derivative of about 40 N cm$^2$.

To increase accuracy and the data collection rate, spacing estimations should be automated. A few prototypes were developed but produced insufficient results. First, infrared (IR) photogates were

attached to the SOCEM in an attempt to count stems along a row as the SOCEM moved through a plot. Figure 4.4 illustrates the photogate set up from an aerial view. The photogates' signals were analyzed to count the number of times the IR beam was broken by stems passing through. However, significant under counts were consistently observed for this photogate method. The wheat stems are too clustered to properly count with this method, particularly at the low photogate heights used (beneath the force bar). Perhaps moving the photogates higher would improve counting estimations, but this method is still unlikely to be accurate enough. An alternative method featuring the IR photogates was also developed. As a photogate moved through a row of stems, the time the photogate was open and blocked was recorded. To eliminate the effect of differences in SOCEM pushing speeds, the ratio of the time blocked to open was then calculated. Using linear regression, a relationship between the ratio and the beam spacing estimations from manual counts was developed. Unfortunately, only a $R^2$ value of about 0.23 was found, suggesting this method was also inadequate, assuming the manual spacing estimations were sufficient. The clustered orientation of the stems still seemed to limit a photogate method. Again, placing the photogates higher up may provide more reliable methods, but the amount of improvement is unknown. With the ease of implementation and low cost, an additional attempt with this method is well within reason.

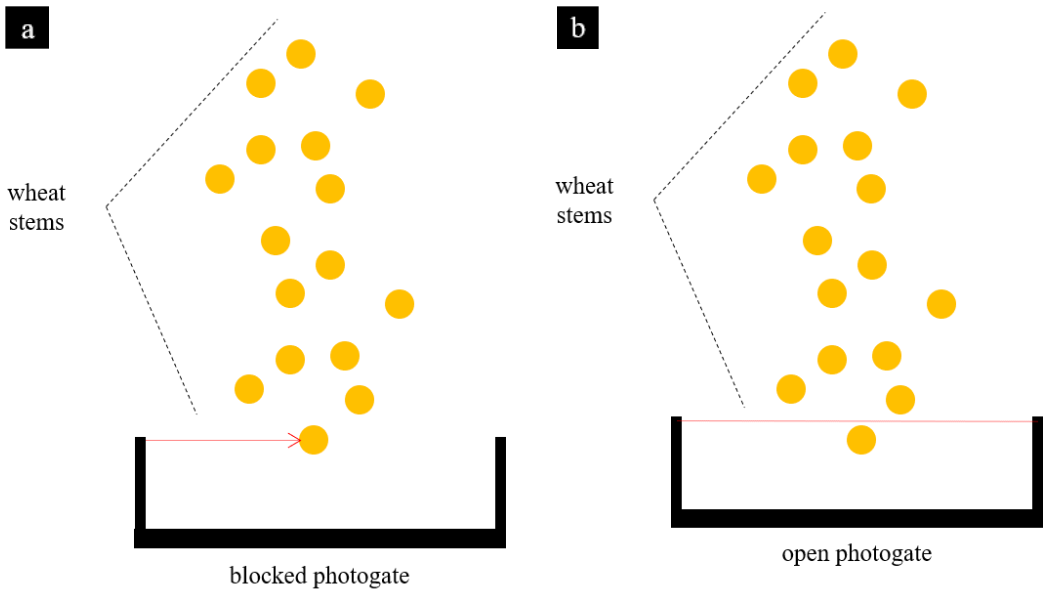


**Figure 4.4** Aerial view of an IR photogate prototype to estimate beam spacing. As the photogates move forward through a row of stems, the IR beam will either be blocked **(a)** or open **(b)**.

Alternatively to photogates, the implementation of an aerial camera system for image analysis presents strong advantages. Attaching a camera to the SOCEM to obtain top view images of the stems

not only would provide accurate spacing measurements; it would also provide the coordinates of the stems. As discussed in 4.2.3, the coordinates of the stems would determine the degree of interactions, improving model accuracy. Obtaining coordinates has already successfully been implemented for early-developed, green plants using high resolution RGB images [3]; however, for post-harvested wheat stems, this may be more difficult due to the limited color difference between stems and the ground. While a camera system would greatly improve accuracy, the implementation is complex. Sufficient processing power and storage would be required to collect data from a camera system. Additionally, analyzing the images would slow down the *EI* estimation process. However, code could automate this process.

### 4.4 Conclusion

Both the SOCEM and the Multiple Inline Interacting Cantilever Model are applicable, scientific tools. The unique, but simple, design of the SOCEM enables rapid, high throughput evaluations of stalk strength in grains. Such evaluations can lead to stronger crops, allowing for a stable crop supply. The SOCEM's capabilities arise from the Multiple Inline Interacting Cantilever Model, which can accurately describe the force response of interacting cantilever beams undergoing unequal, simultaneous deflections. From a simplified perspective, many natural and artificial systems (crops, forests, hairs, brushes, etc.) can be represented with this model. Despite a widespread system, a general model of simple, interacting cantilever beams has not been seen in the scientific literature until this model. The pioneering model has been shown to be accurate across various parameter ranges while remaining simplistic, allowing it to be ideal for applications, not just theory. Some areas may use it for design purposes of artificial structures, but it currently appears more applicable for evaluating existing structures, as done with the SOCEM. Further improvements to both the SOCEM and the model, such as the several examples described here, will magnify their understanding, capabilities, and effectiveness. Both may become highly impactful tools.

### 4.5 References

[1] Howell, Larry L. 2001. *Compliant Mechanisms*. New York: John Wiley & Sons.

[2] Howell, L. L., A. Midha, and T. W. Norton. 1996. "Evaluation of Equivalent Spring Stiffness for Use in a Pseudo-Rigid-Body Model of Large-Deflection Compliant Mechanisms." Journal of Mechanical Design 118 (1): 126–31. https://doi.org/10.1115/1.2826843.

[3] Niklas, Karl J., and Hanns-Christof Spatz. 2012. *Plant Physics*. University of Chicago Press.

[4] Rygol, Joachim, Karl-Heinz Büchner, Klaus Winter, and Ulrich Zimmermann. 1986. "Day/Night Variations in Turgor Pressure in Individual Cells of Mesembryanthemum Crystallinum L." *Oecologia* 69 (2): 171–75. https://doi.org/10.1007/BF00377617.

[5] Yuan, Wenan, Jiating Li, Madhav Bhatta, Yeyin Shi, P. Stephen Baenziger, and Yufeng Ge. 2018. “Wheat Height Estimation Using LiDAR in Comparison to Ultrasonic Sensor and UAS.” *Sensors (Basel, Switzerland)* 18 (11). https://doi.org/10.3390/s18113731.

[6] Singh, Kunwar K., Gang Chen, John B. Vogler, and Ross K. Meentemeyer. 2016. “When Big Data Are Too Much: Effects of LiDAR Returns and Point Density on Estimation of Forest Biomass.” *IEEE Journal of Selected Topics in Applied Earth Observations and Remote Sensing* 9 (7): 3210–18. https://doi.org/10.1109/JSTARS.2016.2522960.

Liu, Shouyang, Fred Baret, Denis Allard, Xiuliang Jin, Bruno Andrieu, Philippe Burger, Matthieu Hemmerlé, and Alexis Comar. 2017. “A Method to Estimate Plant Density and Plant Spacing Heterogeneity: Application to Wheat Crops.” *Plant Methods* 13 (1): 38. https://doi.org/10.1186/s13007-017-0187-1